

# Synchrotron X-Ray Radiation and Deformation Studies

**Fæster Nielsen, Søren**

*Publication date:*
2001

*Document Version*
Publisher's PDF, also known as Version of record

Risø-R-1289(EN)

# Synchrotron X-Ray Radiation and Deformation Studies

**Søren Fæster Nielsen**

**Risø National Laboratory, Roskilde**
**November 2000**

# Abstract

In the present thesis two different synchrotron X-ray diffraction techniques capable of producing non-destructive information from the bulk of samples, have been investigated. Traditionally depth resolution in diffraction experiments is obtained by inserting pinholes in both the incoming and diffracted beam. For materials science investigations of local strain and texture properties this leads to very slow data acquisition rates, especially when characterisation is performed on the level of the individual grains.
To circumvent this problem a conical slit was manufactured by wire electrodischarge machining. The conical slit has six 25µm thick conically shaped openings matching six of the Debye-Scherrer cones from a fcc powder. By combining the conical slit with a micro-focused incoming beam of hard X-rays an embedded gauge volume is defined. Using a 2D detector, fast and complete information can be obtained regarding the texture and strain properties of the material within this particular gauge volume. The capacity of the conical slit for depth profiling is demonstrated by scanning the gauge volume within the bulk of a polycrystalline copper sample, obtaining a two-dimensional map of the grain boundary morphology.
Another X-ray diffraction technique was applied on the three-dimensional X-ray diffraction (3DXRD) microscope at the ESRF synchrotron. The microscope uses a new technique based on ray tracing of diffracted high energy X-rays, providing a fast and non-destructive scheme for mapping the embedded grains within thick samples in three dimensions. All essential features like the position, volume, orientation, stress-state of individual grains can be determined, including the morphology of the grain boundaries.
The first results obtained by using the novel tracking technique are presented in this thesis. For validation, the tracking technique has been applied just below a sample surface and the tracking results are compared to electron microscopy investigations of the same sample surface. The positions of the grain boundaries were reconstructed from the tracking data with an average uncertainty of 26µm and the grain orientations were calculated with a precision of 0.1°.
The tracking technique was applied in a preliminary experiment with the intention of following the rotation history of the crystal lattices in individual grains during deformation. The tracking technique was furthermore applied in combination with synchrotron X-ray tomography in order to gain new information on the wetting kinetics of liquid gallium in aluminium grain boundaries.
Finally, an electron microscopy investigation was carried out in order to describe the lattice rotations and texture evolution in uniaxially compressed aluminium single crystals and polycrystals.

The images on the front page are EBSP images, where the colours indicate the crystal orientation. The image in the centre is an EBSP image of a polycrystalline aluminium sample where the white lines are the grain boundaries determined by the X-ray tracking technique described in this thesis. Surrounding the centre image, are EBSP images of aluminium single crystals deformed to different strain levels.

This Ph.D. thesis is available in an electronic version on http://www.risoe.dk/afm/synch/ and http://www.risoe.dk/rispubl/AFM/ris-r-1289.htm.

ISBN 87-550-2931-0; 87-550-2932-9 (Internet)
ISSN 0106-2840

Print: Pitney Bowes Management Services Denmark A/S, 2001

# Abstract in Danish

I denne ph.d. afhandling undersøges to forskellige diffraktionsteknikker af synkrotronstråling, som begge giver information om en prøves indre på en ikke destruktiv måde.
Traditionelt opnås dybdeopløsning i diffraktionseksperimenter ved at indsætte en blænde i den indkommende og den diffrakterede stråle. En konsekvens af denne metode er, at dataopsamlingen bliver meget tidskrævende, specielt ved bestemmelse af tøjningen og teksturen i individuelle krystalkorn.
For at opnå en hurtigere dataopsamling blev en konisk blænde fremstillet med seks koniske åbninger. Åbningerne er 25μm og designet til at lade seks bestemte Debye-Sherrer diffraktionskegler fra et fcc pulver passere igennem. Ved at kombinere den koniske blænde med en fokuseret indkommende røntgenstråle kan et volumen i prøven defineres.
Fuldstændig information om de lokale teksture og tøjningsegenskaber i det definerede volumen, kan opnås ved at benytte en to-dimensional detektor. Den koniske blændes kapacitet indenfor dybdeprofilering er demonstreret ved at scanne det definerede volumen igennem en polykrystallinsk kobberprøve, hvor ved korngrænsemorfologien i et plan blev kortlagt.
En anden røntgendiffraktionsteknik blev anvendt på det tre-dimensionelle røntgendiffraktionsmikroskop (3DXRD), som er installeret på ESRF synkrotronen. Dette mikroskop benytter en ny teknik baseret på ray-tracing af diffrakterede røntgenstråler med høj energi. Resultatet er en hurtig og ikke-destruktiv metode til at kortlægge indlejrede krystalkorn i tykke prøver i tre dimensioner. Alle essentielle parametre som position, volumen, krystallografisk orientering og spændingstilstanden i individuelle korn kan bestemmes, inklusiv korngrænsemorfologien. De første resultater opnået ved at anvende ray-tracing teknikken er præsenteret i denne afhandling. For validering blev teknikken anvendt lige under overfladen på en prøve af aluminium. Resultatet blev sammenlignet med en elektronmikroskopisk undersøgelse af den samme prøveoverflade. Positionen af korngrænserne blev rekonstrueret fra røntgendatasættet med en gennemsnitlig usikkerhed på 26μm, i sammenligning med den elektronmikroskopiske undersøgelse. Den krystallografiske orientering af kornene blev bestemt med en præcision på 0.1°.
Røntgendiffraktionsteknikken på 3DXRD mikroskopet blev dernæst anvendt i et deformationsforsøg med det formål at følge rotationshistorien af krystalgitteret i de individuelle krystalkorn under deformationen. Teknikken blev yderligere anvendt i kombination med synkrotron røntgentomografi for at undersøge, hvordan flydende gallium gennemtrænger korngrænserne i en aluminium polykrystal.
En elektronmikroskopisk undersøgelse blev til sidst udført, for at beskrive gitterrotationerne og teksturudviklingen i aluminium enkrystaller og polykrystaller deformeret ved kompression.

# Preface

*This thesis is submitted in partial fulfilment of the requirement for obtaining the Ph.D. degree at Copenhagen University. The research described was carried out within the Engineering Science Center at the Materials Research Department at Risø, under the supervision of Erik Johnson at Copenhagen University and Torben Leffers, Materials Research Department at Risø National Laboratory.*

*During the spring 2000 I spent four months as a visiting Ph.D. student at Ecole National Superieure des Mines de St. Etienne, France in the Microstructures and Processing Department. I am grateful to Jean-Christoph Glez, Antoine Baldacci for making my stay in Saint Etienne so pleasant, and Giles Blanc for good advisees on sample preparation.*

*I am thankful to my supervisors for their helpful comments and suggestions during my project and I am grateful for the involvement of Dorte Juul Jensen in the project and especially for her catching enthusiasm. A special thanks goes to Henning Friis Poulsen, who has showed me many of the mysteries in synchrotron radiation, and Erik Mejdal Lauridsen and Søren Schmidt for an endless number of scientific discussions.*

*Grethe Winther and Niels Chr. Krieger Lassen have been a great help in all aspects of calculations regarding EBSP data and Jørgen Bilde-Sørensen always took the time to answer my questions and has been a tremendous inspiration through the whole project both scientifically and privately.*

*Finally I want to thank Marianne Glerup, Anita Voss, Preben Olesen and Cliver Klitholm for their cheerful spirits, that have made my daily life at Risø very pleasant.*

# Contents

# Introduction

Recently significant progress has been made in quantitative characterisation of plastic deformation of polycrystalline metals (Hansen, 1990 and Proc. of 20th Risø Int. Conf, 1999). It has been shown that dislocation boundaries are created during deformation and that these boundaries subdivide each grain into small volume elements that have different crystallographic orientations. The dislocation boundaries constitute a deformation microstructure and the morphology of this microstructure has been shown to be important for the work hardening behaviour of the individual grains and the sample as a whole (Hansen & Huang, 1998).

Aluminium and copper deformed in tension have been found to develop three different types of deformation microstructures, but the actual type of microstructure in a given grain does not seem to depend on the applied strain (Huang & Hansen, 1997). A clear correlation between the type of microstructure and the final grain orientation after the deformation has been observed in thin foils by transmission electron microscopy (Huang & Hansen, 1997 and Huang, 1998). The thin foils were taken from the bulk of a deformed sample. Each foil represents a snap shot of the state of the sample after the deformation has been applied. By transmission electron microscopy it is therefore impossible to study the lattice rotation in individual grains, because only the final state of the sample after the deformation can be observed. The same argument holds for all other surface techniques. Neutron diffraction could on the other hand be used to probe the bulk properties both before and after the deformation. However, this technique cannot resolve the individual grains that typically are in the micron size range. Due to the lack of *in-situ* microscopic probes, models of processing and grain evolution are generally formulated in terms of statistical properties.

The present thesis work has mainly been concerned with the development of a non-destructive method to investigate the bulk of crystalline samples. Such a technique could for example be used to investigate the grain rotations induced by deformation. In deformation studies it has not been possible with standard surface techniques to investigate the importance of the rotation history of the crystal lattice in individual grains for the final microstructure and grain orientation after the deformation. It is not known whether the deformation microstructure within a grain with a given crystallographic orientation depends on the previous lattice rotation and/or the crystallographic orientations of the neighbouring grains. These questions can only be answered by applying a non-destructive high-resolution technique with a high penetration power, in order to observe the orientations of individual grains before, during and after the deformation.

Two different techniques that are useful for this type of investigations are presented in the present thesis. The work has resulted in five papers that are reprinted in appendix C. These papers are referred to in the thesis as Paper A to Paper E.

A minor part of the thesis work is an electron microscopy investigation of aluminium single crystals and polycrystals deformed in compression that only proves that a new non-destructive technique would be a useful tool in deformation studies.

# 1 Synchrotron

Synchrotron X-ray radiation has a very high flux and a very high penetration power. In order to find a non-destructive technique, which is capable of mapping grain boundaries and grain orientations in the bulk of a polycrystalline sample, several different synchrotron techniques were tested.
During the time that this project was carried out a new X-ray microscope was installed at the European Synchrotron Radiation Facility (ESRF) in Grenoble, France and some of the first results from this instrument are presented in the present thesis. Due to the novelty of the X-ray microscope the main part of this project was spent on optimising the microscope and developing software and methods for analysing the recorded data.
In this chapter a short introduction to the basic of synchrotron radiation and the basics of X-ray diffraction will be given. The X-ray microscope is introduced, and a detailed description of the three different synchrotron techniques that have been applied is given in the next three sections.

## 1.1 Synchrotron radiation

X-ray tubes have been used to produce X-rays since Röntgen observed this type of radiation in 1895. The X-ray tube was improved in 1913 by William Coolidge when he used a tungsten filament and in 1934 when R.E. Clark introduced the rotating anode. The next big leap regarding X-ray sources happened in 1947 when Elder, Gurewitsch, Lanmuir and Pollock for the first time observed synchrotron radiation in the shape of visible light from a 70 MeV electron-synchrotron. Since then synchrotron radiation has been used with great success within solid state physics, surface science, material science, crystallography, molecular biology, etc. (Altarelli *et al.*, 1998). The features that make synchrotron radiation useful to different fields of science is the high energy and high flux of the radiation, the corresponding high penetration power, the low angular divergence, and the high coherency.
The first synchrotron radiation sources were particle accelerators that were used mainly for high-energy physics, where the particles were accelerated to velocities close to the velocity of light and then brought to collide. When charged particles are accelerated they emit X-ray radiation. This is a by-product for the high-energy physics but later storage-rings were built to produce only synchrotron radiation. In a synchrotron electrons (or positrons) are accelerated in a booster and then injected into a storage-ring where they travel with constant velocity. By using very precise magnets the electrons can be forced to move in a circular path. The centripetal acceleration of the electrons will produce a wide spectrum of electromagnetic radiation; from visible light to hard X-ray radiation. This is called a white X-ray beam because it is a mixture of many different frequencies. When the magnets bend the relativistic electrons to follow the circular path, the synchrotron radiation will be emitted in an intense beam tangentially to the particle path with a very small angular divergence. The reason for the small angular divergence is the *Doppler*-effect, which becomes extreme because the electrons are moving almost as fast as the electro-magnetic radiation they emit. It can be shown that the opening angle $\psi$ of the synchrotron beam will be:

$$\psi = \frac{1}{\gamma} \tag{1.1.1}$$

where $\gamma$ is the relativistic factor given by $\gamma=m/m_0 \approx E/m_0c^2$. Here m is the relativistic mass of the electron and $m_0$ is the rest mass, E is the energy of the electron and c is the speed of light. For an electron $m_0c^2=0.511$MeV and the angular divergence will according to equation (1.1.1) be less than 0.5mrad when the energy of the electron is greater than 1GeV, which is a typical energy in modern synchrotrons.
The quality of the X-ray beam is measured as the number of photons per second and per relative bandwidth. When normalised with the angular divergence and the area of the radiation source we get the quality measure called *brillance* defined by:

$$Brillance = \frac{number\ of\ \ photons}{\sec \cdot mrad^2 \cdot mm^2 \cdot 0.1\% bandwith} \qquad (1.1.2)$$

If not normalised with the area of the source the value is called the *brightness,* and if not normalised with the area of the source and the angular divergence, the value is called the *photon flux*. Depending on the type of experiment, one of these three quality measures can be used to compare the results from different experiments using different X-ray sources.
Bending magnets are the classical tool for producing synchrotron radiation. Modern synchrotrons, however, are designed as storage rings with some straight sections where undulators or wigglers can be inserted in the particle path. These insertion devices consist of magnets with alternating polarity that force the electrons to follow oscillating paths rather than moving in a straight line. The periodical variations of the magnetic field make the electrons move up and down when they are passing through the undulator. This transverse acceleration of the electrons creates an intense X-ray beam. The electrons are so to speak running slalom in small arcs and this makes constructive interference possible between radiation emitted from different arcs when the electrons are travelling through the undulator. The maximum brillance from undulators is about 10 orders of magnitudes higher than what can be achieved from a rotating anode at the K$\alpha$ line. Undulators are in fact the X-ray sources with the highest brillance known today.

## 1.2 Diffraction theory

In this section the basic theory of X-ray diffraction is presented. The intention is to cover only those aspects of the theory that are used directly in this thesis. For further background the reader is referred to Warren (1969).

### 1.2.1 The reciprocal lattice

X-rays are electromagnetic radiation with a short wavelength that interacts with matter through dipole interactions with the electrons. Typical wavelengths range from 0.1-10Å, which are typical interatomic distances, making X-rays ideal for the study of structures on an atomic scale.
When an electron is placed in the electromagnetic field of an X-ray beam it is forced to oscillate around its equilibrium position with the same frequency as the field. The accelerations of the electron will cause it to emit radiation at the same frequency as the incident radiation, like a small dipole antenna. This is the classical Thomson scattering, where the X-rays are scattered elastically without any loss of energy. If some energy of the incident beam is lost to the crystal we have Compton scattering. Another possibility is photoelectric absorption where

an atom becomes excited and removes the energy by emitting photons (fluorescence) or electrons (the Auger effect) when it decays. For a detailed description of the scattering processes see Woolfson (1996).
In most diffraction experiments a crystal is placed in the X-ray beam. A crystal is a periodic three-dimensional arrangement of atoms. The crystal structure can be described by a Bravais lattice and a unit cell. The crystal can be generated by placing a unit-cell in all the lattice points of the Bravais lattice. If one lattice point is chosen as the origin, the position vector to all other lattice points can be expressed as a linear combination $\boldsymbol{r}=h\boldsymbol{a}_1+k\boldsymbol{a}_2+l\boldsymbol{a}_3$ where *h, k* and *l* are integers and $\boldsymbol{a}_1$, $\boldsymbol{a}_2$ and $\boldsymbol{a}_3$ are the basis vectors in the lattice that spans the unit-cell. In crystallography and diffraction, the reciprocal lattice is more useful than the direct lattice. The basis vectors of the reciprocal lattice $\boldsymbol{b}_1$, $\boldsymbol{b}_2$ and $\boldsymbol{b}_3$ are defined from those of the direct lattice $\boldsymbol{a}_1$, $\boldsymbol{a}_2$ and $\boldsymbol{a}_3$ by

$$\begin{aligned} \boldsymbol{b}_1 &= \frac{\boldsymbol{a}_2 \times \boldsymbol{a}_3}{\boldsymbol{a}_1 \times \boldsymbol{a}_2 \times \boldsymbol{a}_3} \\ \boldsymbol{b}_2 &= \frac{\boldsymbol{a}_3 \times \boldsymbol{a}_1}{\boldsymbol{a}_2 \times \boldsymbol{a}_3 \times \boldsymbol{a}_1} \\ \boldsymbol{b}_3 &= \frac{\boldsymbol{a}_1 \times \boldsymbol{a}_2}{\boldsymbol{a}_3 \times \boldsymbol{a}_1 \times \boldsymbol{a}_2} \end{aligned} \quad , \tag{1.2.1}$$

which have the following properties

$$\boldsymbol{a}_i \cdot \boldsymbol{b}_j = \begin{cases} 1 & for \quad i = j \\ 0 & for \quad i \neq j \end{cases} \tag{1.2.2}$$

Every point in the reciprocal lattice has the position vector $\boldsymbol{g}_{hkl}= h\boldsymbol{b}_1+k\boldsymbol{b}_2+l\boldsymbol{b}_3$ where *h, k* and *l* are integers. The integers *h, k* and *l* are called Miller indices when they are used to describe reciprocal lattice vectors, however, they can be used to describe both directions and planes. The following notation is traditionally applied: (*hkl*) is a specific lattice plane, [*hkl*] is a specific direction, {*hkl*} is a set of equivalent lattice planes and <*hkl*> is a set of equivalent directions.
There are two features that make the reciprocal lattice useful, the distance $d_{hkl}$ between the (*hkl*) planes in the direct lattice is $d_{hkl} = 1/|\mathbf{g}_{hkl}|$ and for cubic lattices the reciprocal lattice vector $\boldsymbol{g}_{\mathrm{hkl}}$ is normal to the (*hkl*) lattice plane in the direct lattice.

### 1.2.2 The diffraction condition

A monochromatic X-ray beam is diffracted on all the atoms in a crystal, and the diffracted X-rays will interfere constructively in such a way that diffraction only will be observed in certain directions. This phenomenon was explained by Bragg (1913), who regarded the atomic planes as semi-transparent mirrors for the incoming beam. He described the condition for occurrence of constructive interference as

$$2d\sin\theta = n\lambda \tag{1.2.3}$$

This condition is the Bragg law, where *d* is the distance between the atomic planes, $\lambda$ is the wavelength of the X-ray beam, and *n* is an integer. Constructive interference will only be observed when the X-ray beam is incident on the lattice planes at the angle $\theta_B$ (the Bragg angle) that satisfies this equation.

Von Laue used another approach to find a condition for constructive interference (Friedrich *et al.*, 1912). He considered the phase difference between electromagnetic waves that are scattered on different atoms. Constructive interference will be achieved when the phase difference is an integral number of $2\pi$. If a plane wave with the direction vector $\boldsymbol{k}_0$ is scattered on two atoms $P_1$ and $P_2$, displaced relative to each other by the vector $\boldsymbol{d}$ (see Fig.1.2.1), then the phase difference can be expressed by

$$\phi = \frac{2\pi}{\lambda}\Delta x = \frac{2\pi}{\lambda}(P_2A - P_1B) = \frac{2\pi}{\lambda}\boldsymbol{d}\cdot(\mathbf{k}_0 - \mathbf{k}) = \frac{2\pi}{\lambda}\mathbf{d}\cdot\mathbf{q} = 2\pi n \qquad (1.2.4)$$

where $\boldsymbol{q}=\boldsymbol{k}_0-\boldsymbol{k}$ is called the scattering vector and is a measure of the momentum transferred in the scattering process. The scattering vector contains information about the crystal structure because it is perpendicular to the scattering planes and the length of the vector gives the spacing between the crystal planes. If the crystal lattice can be described by the lattice vectors $\boldsymbol{a}_1$, $\boldsymbol{a}_2$ and $\boldsymbol{a}_3$ then constructive interference will only occur in the direction $\boldsymbol{k}$, if the following three conditions are fulfilled at the same time:

$$\begin{aligned}
\phi_{a_1} &= \frac{2\pi}{\lambda}\mathbf{a}_1\cdot\mathbf{q} = 2\pi h \\
\phi_{a_2} &= \frac{2\pi}{\lambda}\mathbf{a}_2\cdot\mathbf{q} = 2\pi k \qquad \Rightarrow \qquad \begin{aligned}\mathbf{a}_1\cdot\mathbf{q} &= h\lambda \\ \mathbf{a}_2\cdot\mathbf{q} &= k\lambda \\ \mathbf{a}_3\cdot\mathbf{q} &= l\lambda\end{aligned} \qquad (1.2.5) \\
\phi_{a_3} &= \frac{2\pi}{\lambda}\mathbf{a}_3\cdot\mathbf{q} = 2\pi l
\end{aligned}$$

These equations are called the Laue-conditions and they are only satisfied for certain orientations of the considered crystal lattice. It can be shown that the Laue conditions are satisfied only when $\boldsymbol{q}/\lambda$ is a vector in the reciprocal lattice. Thus constructive interference will only occur when this is the case (Warren, 1969).

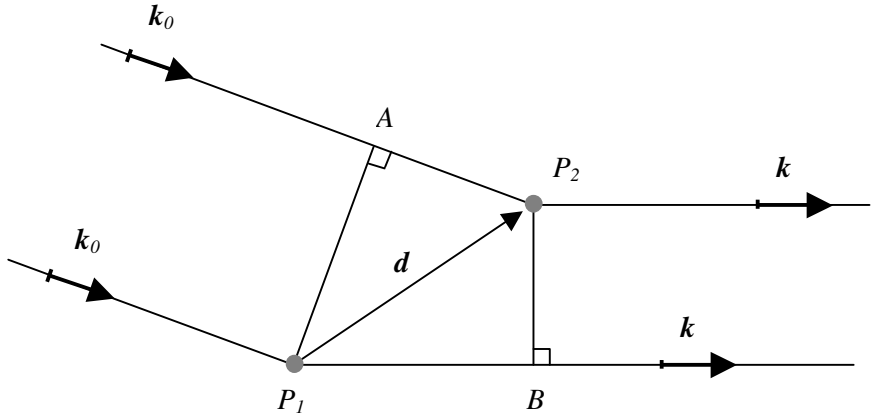


*Fig. 1.2.1. Elastic scattering (i.e. $|\mathbf{k}_0| = |\mathbf{k}| = 1/\lambda$) of a monochromatic beam with the wave vector $\boldsymbol{k}_0$ on two atoms $P_1$ and $P_2$.*

The difference between the Bragg and the Laue description of the diffraction conditions is that the Laue conditions is a vector description that is valid in the three dimensional case. The Laue condition can be illustrated graphically by drawing a sphere with the radius $1/\lambda$ in the reciprocal lattice. The sphere is

called an Ewald-sphere after P.P. Ewald. In two dimensions the Ewald sphere corresponds to a circle that can be drawn together with a two-dimensional cut through the reciprocal lattice. The idea with this sphere or circle is that lattice planes corresponding to a particular reciprocal lattice point will diffract only when the sphere cuts it.
The scattering from one electron in a point, at a distance large compared to the atomic diameter, can be calculated as a space integral of the scattering amplitude times the charge density of the electron. The total scattering from one atom, which is called the atomic scattering factor *f*, can be determined by adding the contributions from all the electrons in the atom. The value of the atomic scattering factor increases with the number of electrons in the atom (Henry & Lonsdale, 1965). The total scattering amplitude from the crystal can be determined by adding the contributions from individual atoms and taking into account their relative displacements. The position of the $i^{th}$ atom in the direct lattice can be written as the sum of the position vector $\boldsymbol{r}_i$ from the origin of the unit cell to the atom, and a lattice vector $\boldsymbol{R}_j$ from the origin of the co-ordinate system to the $j^{th}$ unit cell. The scattering amplitude can then be written as

$$A(\mathbf{q}) = \sum_i^m f_i e^{-i\mathbf{q}\cdot\mathbf{r}_i} \sum_j e^{-i\mathbf{q}\cdot\mathbf{R}_j} \tag{1.2.6}$$

where m is the number of atoms in the unit cell and $f_i$ is the atomic scattering factor of the $i^{th}$ atom. The first sum is called the structure factor *F* because it contains all the information about the positions of the atoms in the unit cell. Calculating the structure factor for a given crystal structure gives information about the relative strengths of the Bragg reflections (the intensity in the diffracted beam can be calculated as $I(\mathbf{q}) = |A(\mathbf{q})|^2$). The second sum is unity when $\boldsymbol{q}$ is a vector in the reciprocal lattice and zero otherwise.
In this thesis only aluminium samples have been studied. Aluminium has a fcc structure where the co-ordinates for the four Al atoms in the unit cell are (0,0,0), (½,½,0), (½,0,½) and (0,½,½). Hence

$$\begin{aligned} F_{hkl} &= \sum_i^m f_i e^{-i\mathbf{q}\cdot\mathbf{r}_i} \\ &= f_{Al}[1 + e^{-i(h+k)} + e^{-i(h+l)} + e^{-i(k+l)}] \end{aligned} \tag{1.2.7}$$

This equation equals $4f_{Al}$ when *h*, *k* and *l* are all even or all odd, but it equals zero when *h*, *k* and *l* are mixed. In other words the reciprocal lattice for an fcc crystal with the lattice parameter *a* will be a simple cubic lattice with the lattice parameter *1/a* minus those lattice points where *h*, *k* and *l* are all even or all odd. The resulting reciprocal lattice for a fcc crystal is therefore a bcc lattice with the lattice parameter *2/a*.

### 1.2.3 Powder diffraction

A powder sample can be considered as an ensemble of small perfect crystals with random orientations. The variation of the orientations will cause the diffraction to occur in a ring pattern when captured on a two-dimensional detector. The rings are called powder rings or Debye-Scherrer rings. The formation of these rings may be explained with the aid of Fig.1.2.2. The incoming beam will only be diffracted in a crystal if the normal ON of plane (hkl) intersects the reference sphere with an angle of 90°-θ to the incoming beam. The diffracted beam will then intersect the two dimensional detector at the point P. In a powder sample with no texture there will be many powder crystals with an (hkl) plane whose normal will intersect the reference sphere at an angle of 90°-θ. If

the normals are spanning a full circle, so will the diffracted beam on the detector. The diffraction spots will only be lying on a continuous ring if a sufficient number of small crystals with random orientation are present in the powder sample. If only a part of the Debye-Scherrer ring is observed on the detector it indicates that the powder crystals have a preferred orientation and the sample is said to have a texture.
Another set of planes with a different *d*-spacing will satisfy the Bragg law with another angle. The diffraction from these planes will obey the same geometrical relationship as illustrated in Fig.1.2.2. The resulting diffraction from all the planes will be a set of concentric rings with different radius on the detector. The radius of the rings depends on the distance from the sample to the detector. The ring pattern on the detector corresponds to a two-dimensional section through the three-dimensional diffraction cones.

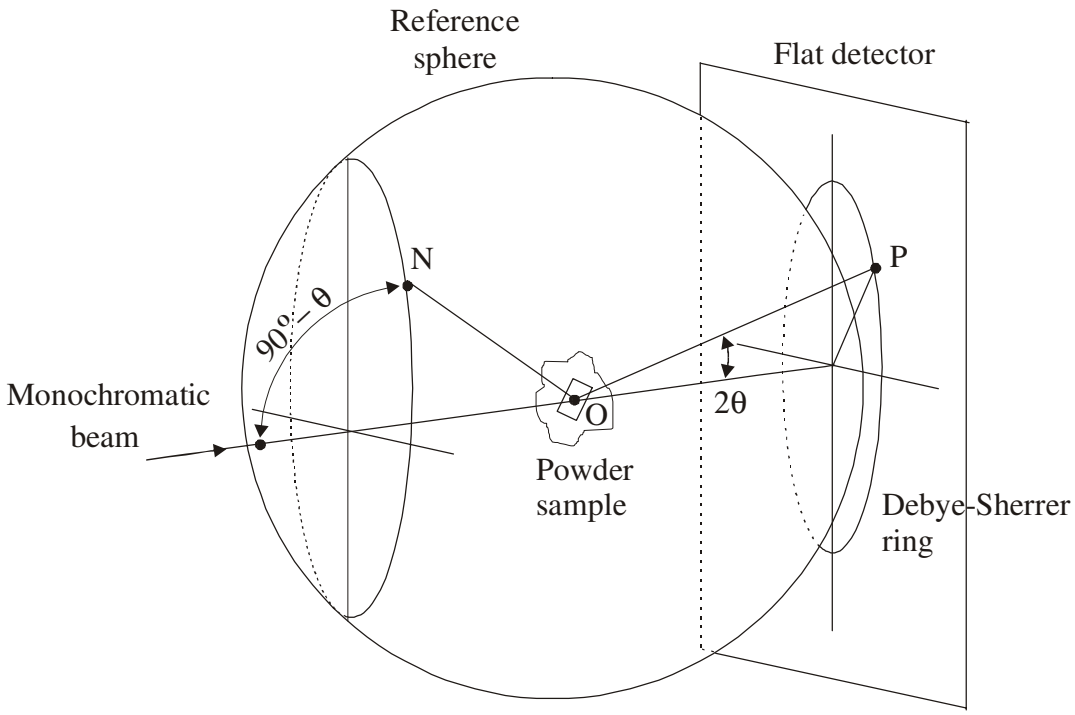


*Fig. 1.2.2. The formation of a powder ring on a two-dimensional detector. The vector from O to N is normal to the (hkl) planes which leads to one diffraction spot at P on the detector.*

# 1.3 The 3D X-ray diffraction microscope

A three dimensional X-ray diffraction microscope (3DXRD) has recently been installed at the Materials Science beamline (ID11) at the European Synchrotron radiation Facility (ESRF) in France. The microscope was developed jointly by the Materials Research Department at Risø and ESRF and it was commissioned during the summer of 1999. The microscope allows two-dimensional focusing of hard X-rays (45-90keV), by using a bent Laue crystal and a bent multilayer as focusing elements (see Fig.1.3.1). For technical details see Lienert *et al.* (1999a) and Poulsen *et al.* (1997). Focal spot sizes are achieved down to $5x5\mu m^2$, and the divergence of the monochromatic beam is approximately 0.1-1mrad. The ESRF synchrotron provides a large photon flux of about $10^{11}$ counts per second and the high energy ensures a high penetration power. When the en-

ergy of the X-ray beam is 80keV the penetration depth is 5mm in steel and 4cm in aluminium. The penetration depth is normally defined as the depth where the intensity of the transmitted beam is reduced to 10%. The combination of these features makes the X-ray diffraction microscope ideal for non-destructive characterisation of the microstructure, in the μm-scale range, within the bulk of crystalline materials. At the Advanced Photon Source (APS) in Argonne there exists another so-called 3D crystal microscope (Ice, 2000) but this instrument operates at lower energies, resulting in lower penetration depths than the 3DXRD microscope (Lienert *et al.*, 1999b) at ESRF.

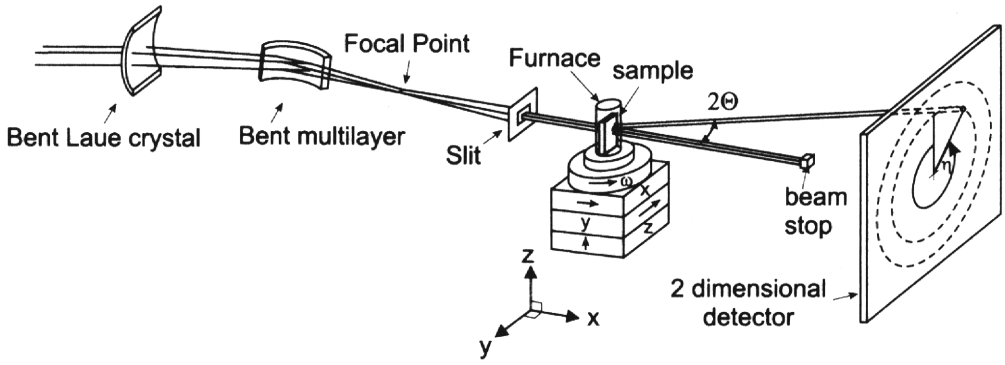


*Fig. 1.3.1. An illustration of the 3DXRD microscope. The diffracted beam exits the sample in an angle of $2\theta$ and is defined on the two dimensional detector by the azimuthal angle $\eta$ on the Debye-Scherrer ring. $\omega$ is the rotation of the sample. (Form Juul Jensen & Poulsen, 2000).*

The microscope is a two-axis diffractometer and consists basically of a detector arm and a sample tower. The sample tower can be translated along three axes in an orthogonal co-ordinate system (x,y,z). Above the tower is mounted a rotation unit and a sample stage with an extra set of x and y translations to be used for alignment of the sample. The sample tower is designed to carry loads up to 200kg making it possible to mount a stress rig or a furnace at the sample position for *in-situ* measurements. Even with a heavy load the sample tower can be rotated and translated with an absolute accuracy of a few microns. All translations and rotations are motorised and controlled through the SPEC program.
Fig.1.3.2 is an image of the 3DXRD microscope. The white synchrotron beam enters the beamline through a hole in the wall, and a monochromatic beam is singled out in the optics box. If a sample is placed in the monochromatic beam the resulting diffracted beam can be studied by positioning a two dimensional detector in its path by scanning the detector arm. At present two different CCD's are available at the beamline; one wide-range with a pixel size of 67μm (Metoptics), and one semi-transparent narrow-range detector with a pixel size of 5μm (Quantics).
Even though the 3DXRD microscope has a very simple set-up it can be used for depth-resolution studies. The main problem in achieving 3D information in all X-ray diffraction experiments is to determine the origin of the diffraction in the direction of the incoming beam. Three different methods to obtain this longitudinal resolution have been developed; conical slits (Paper **A**), X-ray tracking with line focus (Paper **B**) or point focus and focusing analyzer optics (Lienert *et al.*, 1999a). The former two have been developed and tested during the present Ph.D. project and are described in the following in greater detail.

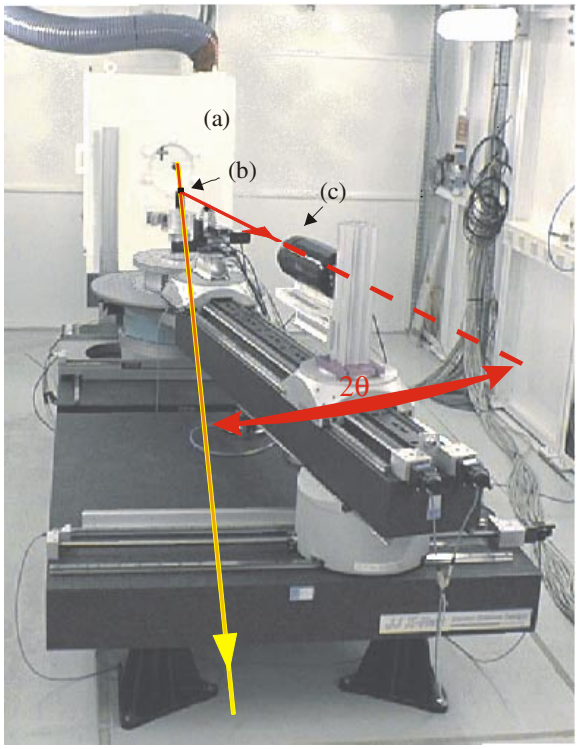


*Fig. 1.3.2. Image of the 3D X-ray diffraction microscope at beamline ID11. (a) is the optics box with the monochromator, (b) is the sample and (c) is a two dimensional detector. The yellow line illustrates the monochromatic beam and the red line indicates the diffracted beam in an angle of 2θ.*

## 1.4 The conical slit

The Materials Research Department at Risø has designed a conical slit to investigate fcc crystals. This device makes it possible to achieve longitudinal resolution in an X-ray experiment. Discussed below are the problems associated with achieving longitudinal resolution. The design of the manufactured conical slit and the non-trivial aligning process of the conical slit are described, and finally the experimental results are discussed.

### 1.4.1 Slits and longitudinal resolution

In most X-ray diffraction experiments a sample is placed in the X-ray beam and the resulting diffraction is studied. It is not obvious, however, from exactly where inside the sample the diffraction originates. The longitudinal resolution is missing. A gauge volume within the sample can be defined by using conventional slits to confine both the incoming and the diffracted beam, see Fig.1.4.1. By back-tracing the edges of the slits, a volume element in the sample is found for both the incoming and the diffracted beam. The crossing of the two volume elements is the gauge volume within the sample where the diffraction must have originated. Alternatively, focusing instead of slits could be used to confine the incoming beam.
A disadvantage of this technique is that only one gauge volume, one reflection and one orientation is measured at a time. This problem can be overcome, however, by using a conical slit (CS) with openings along the Debye-Scherrer cones. When a CS is positioned in the diffracted beam it will define a three-

dimensional gauge volume in the sample. If a two-dimensional detector is used it will be possible to record a full Debye-Scherrer ring and thereby to get complete information on the texture from one particular gauge volume in only one image. By using a detector far away from the origin of the diffraction, to ensure a high angular resolution, information of the strain-field could in principle be obtained simultaneously.

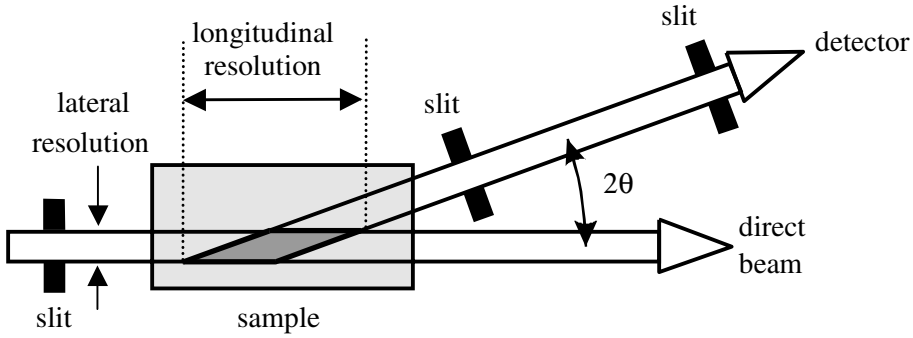


*Fig. 1.4.1. Two-dimensional illustration of the cross-beam technique where slits are used to confine both the incoming and diffracted beam. The resulting gauge volume is shaped as a needle.*

Another advantage is that one diffraction ring consists of several diffraction spots yielding information from many different reflecting grains in one image. A conical slit provides a considerable faster way to obtain longitudinal resolution than traditional slits.
Fig.1.4.2 illustrate the experimental set-up when using a CS. A sample is positioned in a monochromatic beam that is defined in two dimensions either by a slit or by focusing. The CS is mounted after the sample in the diffracted beam. Further downstream a two-dimensional detector can record the diffraction that has been allowed through the conical slit.
By varying the material thickness of the conical device it can be designed to function as a slit or as a collimator. As a slit, the strain profile of the sample can be directly monitored in the images, provided the 2D detector has sufficient resolution. Moreover, for coarse-grained samples the integrated intensity of a single grain can be deduced from a single exposure by summing over the strain profile. For fine-grained samples, the option of summing over the strain profile implies that texture components are directly observable. As a collimator, only a part of the strain profile is allowed to pass. Hence, neither strains, nor integrated intensities are directly observable. Instead it is necessary either to scan the incoming energy or to deconvolute the spatial degrees of freedom (Lienert *et al.*, 2000a). Intensities will also be substantially smaller in this case. On the other hand, a collimator defines the gauge volume better than a slit. In this thesis work I will only be concerned with the slit alternative. In the limit of an infinitesimally thin slit the conical openings will be rings. From here on the conical slit openings will be referred to as rings.

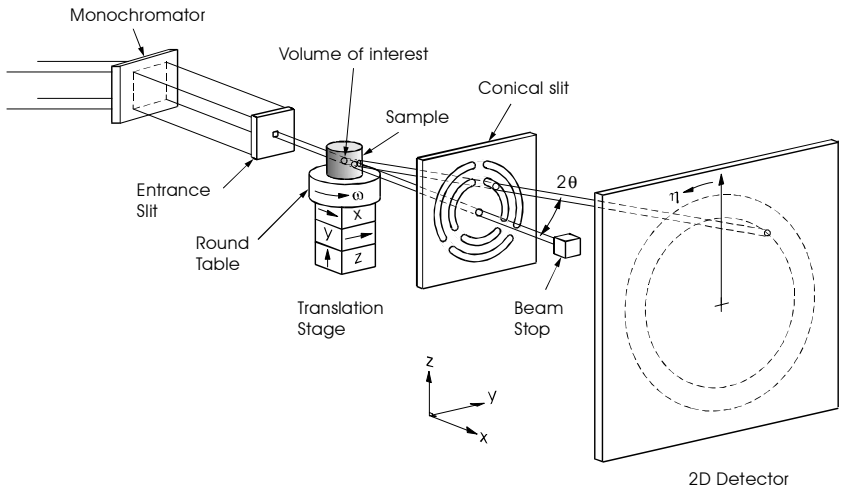


*Fig. 1.4.2. An illustration of the experimental set-up. The CS selects the diffraction from a specific gauge volume in the sample.*

### 1.4.2 Design and manufacturing of the CS

The manufactured conical slit (CS) has six slit openings, each with a gap of 25µm. The size of the gaps was chosen as a compromise between achieving a high resolution and still having a reasonably intensity in the Debye-Scherrer rings on the detector. The CS is 4mm thick, made of tungsten carbide and designed to be used at X-ray energies just above the tungsten *K*-edge for the investigation of fcc materials. The six fcc powder rings that are allowed through the CS are the {111}, {200}, {220}, {222}, {331} and {422} reflections. The CS also has a central hole to allow the direct beam to pass through the slit. The heat-load from the direct beam can then be shifted to an appropriate beam-stop after the CS.

In order for diffraction to occur from a crystalline sample, the Bragg equation has to be fulfilled. The conical slit openings in the CS had to be manufactured with an angle $2\theta$ so the Bragg diffraction at one particular energy from a given fcc material with a certain set of d-spacings would be allowed through the slit. The slit openings in the CS is designed to fit the calculated Debye-Scherrer cones from an Ag powder with a lattice constant $a_{Ag}$= 0.40862nm, a distance of 10mm between the powder and the CS, and an X-ray energy of 69.263keV. Other fcc materials can be investigated by changing the energy. The X-ray energy that is necessary to make the diffraction from a particular fcc material fit the slit openings in the CS can be calculated by the relation $2d\sin\Theta=12.398/E$, where d is the lattice distance for the fcc material, and $2\Theta$ is the fixed opening angle in the CS.

The CS was constructed at Institute für Mikrotechnik Mainz, Germany by wire electrodischarge machining (wire-EDM). This is a thermal method where material in the working zone is melted and removed through a surrounding dielectric liquid. Various EDM techniques have been established, for example in the tool making industry, for the generation of moulds or dies for punching purposes. The EDM technique offers a high degree of freedom in precisely manufacturing small components. Unfortunately this method can only be used with wires down to 30µm in diameters. The gaps in the CS were designed to be 25µm and it was

therefore impossible to produce the whole CS from one single piece of tungsten. Instead seven conical parts where manufactured individually. When assembled the seven pieces form the CS (Fig.1.4.3a,b). The conical parts were manufactured with small uniform taps to ensure a constant slit gap (Fig.1.4.3c). The taps also have the advantage that they make the conical parts self-aligning when they are assembled. Machining by wire-EDM heats the surroundings of the cutting zone. Unfortunatly heating can introduce microcracks in the material. By lowering the discharged energy the heat effected layers can be removed furnishing a very smooth surface finish (Fig.1.4.3d). The main problem in the fabrication process was the formation of elliptically shaped conical parts instead of the intended circular cross section. The inner and outer diameters on both sides of each individual part were measured in a scanning electron microscope and the absolute error on the diameters was found to be at worst 13µm and in average 4.6µm.

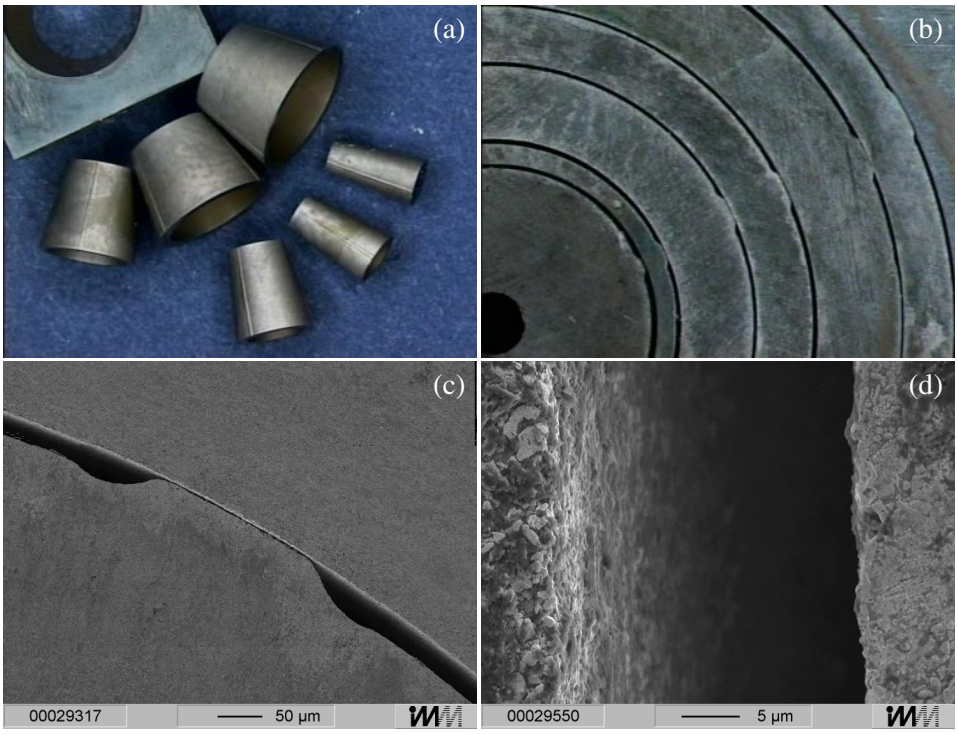


*Fig. 1.4.3. (a) The disassembled CS consist of seven parts, (b) top view of the assembled CS, (c) one tab that provide a constant silt opening of 25µm, and (d) detailed view of gap between two parts.*

### 1.4.3 Alignment of the CS

If the conical slit (CS) is perfectly aligned, a fine grained well annealed fcc powder with no texture will give homogeneously illuminated rings on a two dimensional detector behind the CS. An alignment error may lead, however, to an inhomogeneous illumination of these rings. This inhomogeneity can be utilised for the alignment. The aligning process is nontrivial because there are six degrees of freedom: the wavelength of the incoming radiation, the three translations and two rotations of the CS. To simplify the discussion it is an advantage to concentrate on only one ring in the CS. Later an alignment strategy can be generalised to apply to all the six rings in the CS. In the following it is also assumed that the machining and assemblage errors of the CS are negligible when

compared with alignment errors. Thus only the influence of the alignment errors will be considered here.
Fig.1.4.4 illustrates the geometry of one Debye-Scherrer cone and the corresponding ring of the CS. The co-ordinates of the centre of the ring are ($x_c$, $y_c$, $z_c$), and the tilts around the y- and z-axes are denoted $\omega_c$ and $\chi_c$, respectively. $2\Theta$ is the opening angle of the slit and $\eta$ defines the azimuthal angle in the image, with $\eta$=0 at the 12 o'clock position. $\Delta 2\theta$ is an angular offset caused by a small difference from the correct energy. A misalignment of the ring is related to an angular offset $\delta 2\Theta$ between the ring and the Debye-Scherrer cone (se Fig.1.4.4). When the ring is completely aligned, $\delta 2\Theta$ must be zero for all angles $\eta$. When the complete alignment is achieved then $x_c=y_c=z_c=\chi_c=\omega_c=\Delta 2\theta=0$, and the diffracting volume will be situated at (-L, 0, 0).

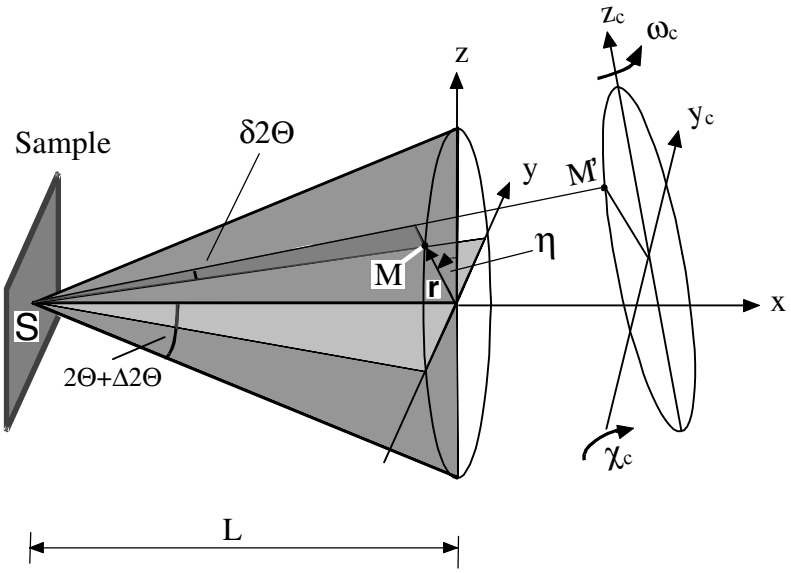


*Fig. 1.4.4. Geometry related to conical slit movements. Illustration of one Debye-Scherrer cone and a misaligned slit. The Debye-Scherrer cone is diffracted by a thin powder sample illuminated with a narrow beam. The direct beam is along the x-axis. For a given angle $\eta$ the misaligned ring in the conical slit selects the direction SM' instead of the beam direction SM leading to an angular offset $\delta 2\Theta$ with respect to the Debye-Scherrer cone.*

With these definitions the position of the ring can be described with the position vector **r**=Ltan2Θ(0, -sinη, cosη). When the ring is rotated by $\chi_c$ around the y-axis and by $\omega_c$ around the z-axis, followed by a displacement ($x_c$, $y_c$, $z_c$), its new position vector is given by:

$$\begin{pmatrix} r_x \\ r_y \\ r_z \end{pmatrix} = \begin{pmatrix} \cos\omega_c & -\sin\omega_c & 0 \\ \sin\omega_c & \cos\omega_c & 0 \\ 0 & 0 & 1 \end{pmatrix} \begin{pmatrix} \cos\chi_c & 0 & \sin\chi_c \\ 0 & 1 & 0 \\ -\sin\chi_c & 0 & \cos\chi_c \end{pmatrix} \begin{pmatrix} 0 \\ -\sin\eta \\ \cos\eta \end{pmatrix} L\tan 2\Theta + \begin{pmatrix} x_c \\ y_c \\ z_c \end{pmatrix} \tag{1.4.1}$$

Notice that it is only for small rotations and small translations that the individual operations commute and the final result does not depend on the order in which the corrections are applied. The angle $\delta 2\Theta$ between the Debye-Scherrer cone and the ring is then found from:

$$\tan(2\Theta + \Delta 2\Theta + \delta 2\Theta) = \frac{\sqrt{r_y^2 + r_z^2}}{L + r_x} \tag{1.4.2}$$

By aligning the edges of the central hole in the CS (made for the direct beam), good pre-aligning can be achieved. This means that it is only necessary to search for an expression for small rotations $\chi_c$ and $\omega_c$ and small translations $x_c$, $y_c$ and $z_c$ because only small alignment errors need to be considered. Therefore, the expression (1.4.2) can be evaluated in a first order approximation in $\Delta 2\Theta$, $\chi_c$, $\omega_c$, $x_c$, $y_c$ and $z_c$ and leads to:

$$\delta 2\Theta = -\left(\Delta 2\Theta + \frac{x_c}{2L}\sin 4\Theta\right) - \cos^2 2\Theta\left\{\sin\eta\left(\frac{y_c}{L} + \omega_c \tan^2 2\Theta\right) + \cos\eta\left(-\frac{z_c}{L} + \chi_c \tan^2 2\Theta\right)\right\} \quad (1.4.3)$$

Each bracket of this equation contains pairs of parameters which are "coupled" as they can compensate each other. A small mismatch between the opening angle $2\Theta+\Delta 2\Theta$ of a given (hkl) Debye-Scherrer cone and the corresponding ring in the CS can be compensated with a translation of $x_c$. In the same way, a misorientation of $\omega_c$ or $\chi_c$ can be corrected with a translation of $y_c$ or $z_c$, respectively. Moreover, an alignment error of $x_c$ or a non-vanishing $\Delta 2\Theta$, affects the offset $\delta 2\Theta$ for all positions $\eta$ in the same way. However, a variation in $\omega_c$ or $y_c$ hardly alters $\delta 2\Theta$ at the positions $\eta$=0° and $\eta$=180° whereas an error in $\chi_c$ or $z_c$ has a negligible influence on the intensity at $\eta$=±90°.
A complete alignment of the CS can be achieved by analysing the geometry of the intensity patterns transmitted through one ring in the CS and applying Eq. (1.4.3). Fig.1.4.5 illustrates typical intensity patterns as they look like on the detector.

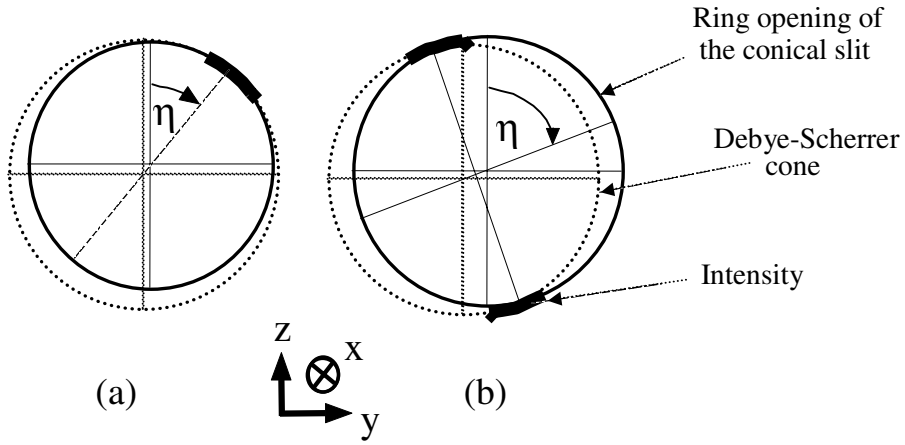


*Fig. 1.4.5. Typical intensity distributions on a 2D X-ray detector when the conical slit is misaligned with respect to the Debye-Scherrer cone. (a) The conical slit is not aligned along x. Projected on the X-ray detector, the ring of the conical slit is smaller than the Debye-Scherrer cone. The Debye-Scherrer cone is only seen on the detector in a small range around the angle $\eta$. (b) The conical slit is aligned along x. Parts of the Debye-Scherrer cone are seen at the angles $\eta$ and $\eta$+180° due to a misalignment of the orientation and the transversal position ($y_c$ and $z_c$) of the CS.*

When substituting $\eta$ with $\eta$+180° in Eq. (1.4.3) the second term will change sign. This means that if the CS is scanned along the x-axis then the intensity in the diffraction rings on the detector will peak simultaneously at opposite positions if, and only if, the first term in Eq. (1.4.3) is zero. By acquiring images while scanning the CS along the x-axis it is possible to find the positions of maximum intensity for $\eta$ with $\eta$+180° in all the rings, and Eq. (1.4.3) can then be solved for $\Delta 2\Theta$ and $x_c$. To bring the two last terms in Eq. (1.4.3) to zero it is necessary to focus on one ring at a time. Fig.1.4.5 (b) illustrates a typical situa-

tion with two peaks centred at $\eta$ and $\eta$+180°. To align the CS, a combined $y_c$ and $z_c$ scan along the line perpendicular to the line connecting the two spots has to be performed. In this way the ($y_c$, $z_c$) positions, that give an isotropic illuminated ring on the detector, can be found. The CS is now aligned with exception of the redundancy between $y_c$ and $\omega_c$ and between $z_c$ and $\chi_c$. This procedure can now be repeated for all the rings and global least-square optimisation of $y_c$, $z_c$, $\omega_c$ and $\chi_c$ can be found from the set of optimal ($y_c$,$z_c$) position for all the rings.

### 1.4.4 Experimental and calculated depth resolution

A test of the conical slit (CS) was performed at the synchrotron beamline ID15, ESRF. The aim was to measure the experimental depth resolution. The CS only allows diffraction from a specific gauge volume to pass through the slit, or seen from the other direction the CS so to speak focuses on the gauge volume. By scanning the CS along the x-axis the CS will focus on different gauge volumes within the thickness of the sample (see Fig.1.4.6). When focusing outside the sample no intensity, should in principle, be measured. If the thickness of the sample is known a scan along the x-axis will provide a direct measure of the longitudinal resolution of the CS.

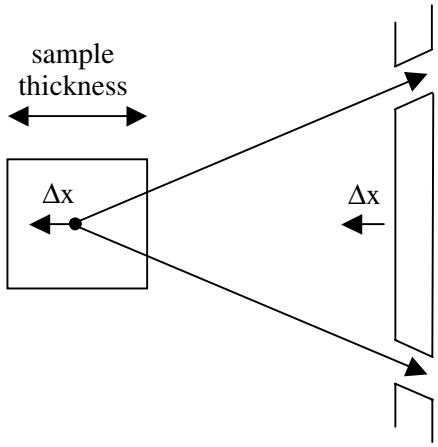


*Fig. 1.4.6. The figure illustrates that a movement Δx of the CS will cause the gauge volume to move the same amount. The depth resolution of the CS can then be directly measured if the thickness of the sample is known by scanning the gauge volume through the sample.*

The sample used for this test was a 100µm thick layer of nickel (Ni) powder, packed between two glass plates. The Ni powder was provided by P. Suortti and he has earlier described the powder as well annealed and with virtually no strain (Suortti, 1977). The incoming beam was defined by a square aperture to 22×24µm$^2$, and the beam profile was found to be almost Gaussian in both directions. To acquire the images a two-dimensional image intensifier was placed 30cm from the Ni sample.
The aligning of the CS was performed as described in the previous section. However, assemblage errors of the CS made it impossible to optimise the intensity in all the rings at the same time. The CS was scanned in a three-dimensional mesh by translating in the x, y and z directions. An exposure was acquired at each position. The global assemblage errors can be found by evaluating the azimuthal variation of the intensity in the six rings in all the images and comparing the x, y and z settings where the individual rings are aligned. During the experiment no attempt was made to find the optimal settings for the aligning of all the rings that take the assemblage errors into account. Instead we

chose to align the CS with respect to the {200} ring. Fig.1.4.7 shows a typical image of the powder diffraction that is transmitted through the CS. The figure clearly shows that for example the {422} ring is not completely aligned (some intensity is missing in the lower left part of the diffraction ring).

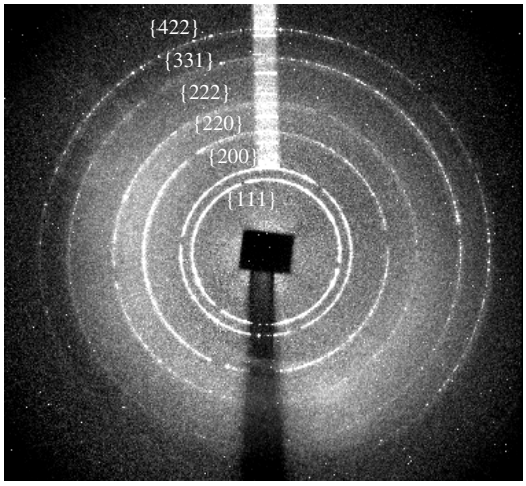


*Fig. 1.4.7. A typical recorded image of powder diffraction when using the CS. The {hkl} indexes of the individual rings are written on top of the image.*

To find the depth resolution the CS was scanned in the x-direction through the {200} alignment centre. Thirteen images were recorded with equidistant steps of 100µm along the x-axis. For each ring the intensity was integrated radially as well as azimuthally, by using the image-processing program *FIT2D* (Hammersley *et al.*, 1996). The normalised integrated intensity distributions as function of the x-position of the CS are plotted in Fig.1.4.8 for the four innermost rings. Due to a lack of recorded intensity the two outermost rings are not included. The variation of the integrated intensity with x was fitted to a Gaussian. The resulting fitted centre positions and widths are listed in Table 1.4.1. The table also contains calculated values for the widths of a perfect CS, assuming a Gaussian profile of the incoming beam.

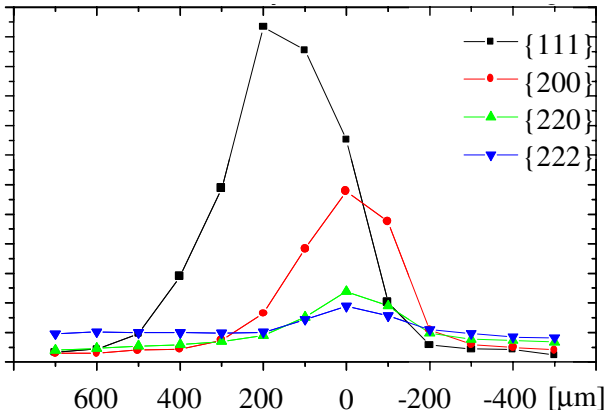


*Fig. 1.4.8. Normalised plot of the integrated intensity as function of the x-position of the CS. x=0 corresponds to the position where the CS is focusing on the middle of the 100µm thick Ni powder sample.*

As seen from Table 1.4.1 the measured and calculated depth resolutions are in reasonable agreement with better resolution for higher-order reflections as expected. In general the measured resolutions are smaller than the calculated.

This is caused by the combined effect of the assembly and aligning errors that make the slits appear more narrow when seen from the diffracted beam. The centre positions are constant within the errors on the measurements, with exception of the {111} reflection, which is offset by 153μm. The magnitude, seen in relation to the measured width, implies that assembly errors have caused the focal point of the {111} reflection to be shifted. The {111} slit in the CS is so to speak cross-eyed compared to the other slit openings. In general we estimate the average machining and assemblage errors on the diameter of the CS rings to be both of the order of 5μm.

| Reflection | Calculated FWHM [μm] | Measured FWHM [μm] | Measured center position [μm] |
|---|---|---|---|
| {111} | 366 | 275 ± 12 | 153 ± 5 |
| {200} | 315 | 222 ± 12 | 0 ± 6 |
| {220} | 239 | 217 ± 16 | 10 ± 7 |
| {222} | 181 | 192 ± 15 | 4 ± 7 |

*Table 1.4.1. The calculated and measured FWHM of the four reflections. The measured FWHM are decreasing for higher reflections. The centre positions of the measured peaks are in good agreement, with exception of the {111} peak. This indicates that the {111} slit opening is cross-eyed compared to the other slit openings.*

### 1.4.5 Grain boundary mapping

The main use of the conical slit (CS) is expected to be local strain and stress measurements (Lienert *et al.*, 2000b). The CS can also be applied for mapping grain boundaries and grain orientations in polycrystalline samples. H.F. Poulsen and S. Garbe have tested a CS in a grain mapping experiment at beamline ID11, ESRF. The aim of this experiment was to map the grain boundaries and grain orientations within an embedded layer of a coarse-grained $4.5\times4.5\times4.5mm^3$-sized Cu polycrystal. Afterwards the sample was sectioned and the same layer that was mapped in the synchrotron experiment was investigated by electron microscopy (EBSD). The result from the two different techniques was then compared.

The set-up was identical to that presented in Fig.1.4.2, with the incoming beam being defined by a $50x50\mu m^2$ aperture. Results shown here refer to one specific layer and the (200) data only. To find the orientation of a specific grain the sample was first rotated from $-90^o$ to $90^o$ in steps of $10^o$ while oscillating by ±5° at each step. By identifying at least 3 major spots relating to lattice planes that are perpendicular to each other, a first fit was obtained. The exact orientation was determined by acquiring exposures at constant ω and 'scanning' ω with an accuracy of $\Delta\omega=0.1^o$. To map a specific grain the variation in total intensity of a selected reflection was monitored while scanning the gauge volume in x and y. The boundary, defined at the half-intensity point, was determined by interpolation.

Resulting synchrotron and EBSP data are shown in Fig.1.4.9. The map provided by synchrotron diffraction is not complete, due to an inadequate amount of

beamtime (about 12 hours). Grain positions measured by the two methods correspond within 150μm and orientations within 2°. There is a large potential for substantial improvements of these numbers, especially the spatial accuracy. Firstly, the impinging beam size can be reduced to $5\times5\mu m^2$ by focusing the monochromatic beam. Secondly, measuring several reflections from the same grain, corresponding to approximately 90° sample rotations, can diminish the effect of the poor resolution in the direction along the beam. Thirdly, slight misalignments during synchrotron measurement implied that the measured layer is not identical to the surface measured by EBSP.

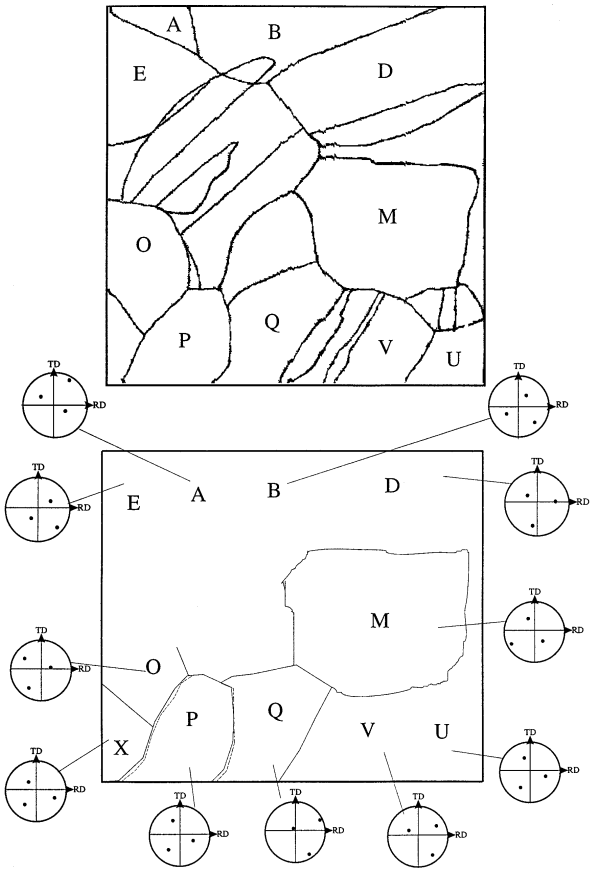


*Fig. 1.4.9. Grain mapping of the top layer in a Cu poly-crystal by electron microscopy (EBSP) above, and using the hard X-ray conical slit set-up illustrated in Fig.1.4.1, below. Also shown are the determined <200> pole figures (see App. **B**) for the individual grains. The boundary of grain P was measured using a (200) reflection from grain P (solid line) as well as (200) reflections from neighbouring grains X, O and Q (dashed lines).*

### 1.4.6 Discussion

The work with the conical slit has been published (Paper **A**) and it is probably the first attempt to use a conical slit for depth profiling, three-dimensional mapping of grain boundaries and grain orientations, in an X-ray diffraction experiment. Earlier a conical device has been used in the diffracted beam (Häuserman & Itié, 1992), but only for 'beam cleaning' and energy determination in high-pressure research. The conical device was in their case a conical collimator with only one ring.

The basic principle can naturally be applied to X-rays with lower energies or to neutrons, but in these cases flat conical devices and flat 2D detectors cannot be applied due to the larger scattering angles. The main drawback by using a CS is that it will only work for samples that belong to one specific symmetry group and only at one specific energy. The CS described in this thesis was designed for fcc materials, which of course limits the applicability of the CS. The conical parts all suffer from some degree of eccentricity, even though the most modern wire-EDM machining was used to produce the conical parts. When assembled the achieved slit width is approximately 25±5μm. This uncertainty influences the resolutions of the CS and makes it difficult to compare intensities through different rings.

The assembly errors could have been avoided if it had been possible to manufacture the six slits in one piece of tungsten. When the slit is assembled from seven conical pieces the combined machining and assembly errors could be determined by performing a calibration of the CS. This could be performed by comparing the $x_c$, $y_c$ and $z_c$ settings for the optimal alignment of the individual rings in the CS, as described earlier. However, this would complicate the data analysis substantially.

The tab system that ensures self-alignment of the cones needs to be modified. Structuring the inside of the cones and at the same time increasing the height of tabs on the outside would definitely lead to an improvement. Alignment and tilting errors between the cones due to the geometrical errors of tabs over the entire height could be minimised. The cones would be secured against each other. Therefore, distortion could be excluded as well. A better self aligning system for the cones in the CS would ensure that all slit openings focus on the same gauge volume, and cross-eyed slits like the (111) ring would be avoided.

A straightforward way to reduce the errors is to make the conical device thinner. This is feasible, as the penetration depth at 70keV is 62μm in tungsten. Hence even at 1mm thickness, the transmitted fraction is $10^{-7}$. A thinner device would also constitute a more ideal slit.

The aligning of the present conical slit is a complicated task because an error in the position of the CS and the related angular settings has the same effect. The misalignment of each of these "pairs of parameters" can be recognised from the appearance of the intensity transmitted through the CS. With an appropriate beam and an appropriate reference sample, the position and the orientation of the CS can be adjusted.

As illustrated in section 1.4.5 the CS can be used to map grain boundaries and grain orientations and compared to conventional slits the acquisition time is short. However, if a large ensemble of grain were to be mapped, it would not be possible with the CS within a reasonable time. The CS has a large potential within stress and strain measurements from a particular gauge volume, but when speed is required in order to map grain boundaries and grain orientations in a large volume element it would be better to use the tracking technique, described in the following section.

## 1.5 X-ray tracking

The microstructure in polycrystalline materials has mostly been studied in planar sections by microscopy techniques like SEM on sample surfaces, or TEM on thin foils. The 3DXRD microscope at ESRF provides a new and fast non-destructive technique for studying planar sections in the bulk of samples by using a so-called tracking technique. All essential features like the position, volume, orientation, stress-state of the grains can be determined, including the morphology of the grain boundaries.
This section starts with an introduction to the basic principles of the tracking technique and the following sections describe individual aspects of the tracking technique in more details. The experimental results have been published (Paper **B, C** and **D**).

### 1.5.1 The tracking principle

The tracking algorithm is inspired by the use of three-dimensional detectors in high-energy physics and is based on a monochromatic high energy X-ray beam focused into a line and a two-dimensional detector. The principle is sketched in Fig.1.5.1. When the incoming beam is focused into a line it defines a layer within the sample. All grains that happen to fulfil the Bragg condition in this layer give rise to diffraction spots on the detector. The diffraction spots are the projected images of the corresponding diffracting grains in the observed layer and the projection angle is a combination of the scattering angle $2\theta$ and the azimuthal angle $\eta$ on the detector.

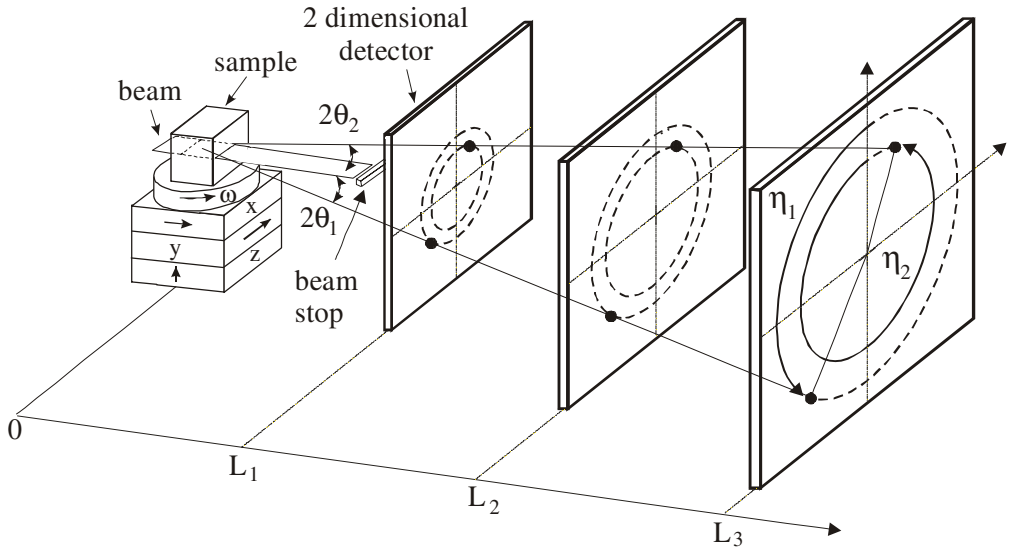


*Fig. 1.5.1. Illustration of the tracking technique. When the detector is translated away from the sample the diffraction spots will move outwards on the detector. The positions of the diffracting grains in the sample are determined by linear fits. The fits also provide the $2\theta$ and $\eta$ values.*

The position of each diffraction spot on the detector is measured and the intensity-weighted centre-of-mass (CM) of each diffraction spot is computed. This procedure is repeated at several detector distances corresponding to different L values in Fig.1.5.1. Linear fits through corresponding CM points extrapolate to the CM of the diffracting grains and provide the angles $2\theta$ and $\eta$. To obtain the cross-sectional grain shape, the periphery of the diffraction spot in the image

acquired at the closest distance is projected into the illuminated sample plane along the direction determined by the fit.
By rotating the sample around an axis ω, perpendicular to the illuminated plane, all grains will come to fulfil the Bragg condition and a complete map of all grain boundaries and grain orientations in the plane is thus produced. A three-dimensional map can be obtained simply by translating the sample in *z* and repeating the procedure for several layers.
Examples of actual images acquired with different detector-to-sample distances are given in Fig.1.5.2. The diffraction spots are clearly seen to move outwards on the detector when the detector is translated away from the sample. The detector is in this case a CCD-plate, which is built into a detector system that consists of two fluorescence screens 200μm apart. This allows the detector to be aligned in such a way that the direct beam goes between the two fluorescence screens. Only the diffracted beam hits the fluorescence screens and is transferred by optics to the CCD. The direct beam has a two-dimensional Gaussian shape and some of the tails will be detected by the part of the fluorescence screens that is closest to the gap between them. This effect is seen in Fig.1.5.2 as two bright rectangles in the centre of the images. All other spots are diffraction spots from one layer in an aluminium sample.

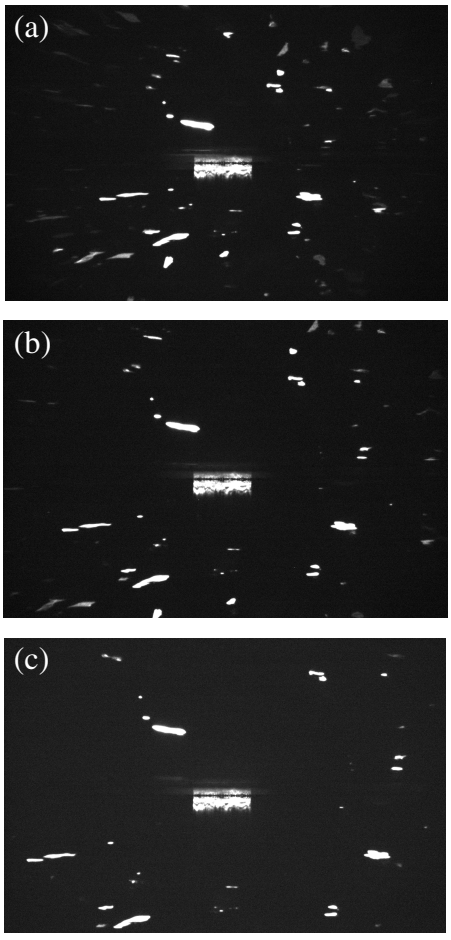


*Fig. 1.5.2. Three images of the diffraction pattern form an Al sample. The distance from the sample to the detector in (a), (b) and (c) are 7.6mm, 10.3mm and 12.9mm, respectively. The two rectangles in the middle of the images correspond to the tails of the direct beam, which are detected by the edges of the two fluorescence screens in the detector.*

### 1.5.2 Diffraction spots and mosaicity

In tracking, the incoming beam is focused into a line (typically $800\times5\mu m^2$) that intersects the sample in one full layer. The diffraction pattern from this layer is a projection of the grains that satisfy the Bragg law. The shape of a diffraction spot depends on both the projection angle, which is a combination of the scattering angle $2\theta$, and the azimuthal angle $\eta$ of the spot on the detector. This is illustrated in Fig.1.5.3. The figure shows a quadratic grain and the resulting diffraction spots for two different $\eta$ values. The small scattering angle will result in a rectangular diffraction spot for $\eta = 0°$. The size of the spot in the y-direction will be the same as the size of the diffracting grain, but the spot size in the z-direction will be a compressed version of the thickness of the grain. The situation is different for $\eta = 90°$. The height of the line-focused beam is only a few microns and the layer defined by the beam in the sample can therefore be considered as two-dimensional. If the diffracted beam has an angle of $\eta = 90°$, then the two-dimensional cross-section will be projected into a one-dimensional line on the detector. The projection of a diffraction spot with the dimensions $y_{det}$ and $z_{det}$ results in a grain with the dimensions $\Delta x$ and $\Delta y$. The projection can be expressed as

$$\begin{aligned} y_{\text{det}} &= \Delta y \\ z_{\text{det}} &= \Delta x \tan(2\theta)\cos(\eta) \end{aligned} \qquad (1.5.1)$$

where $(y_{det}, z_{det})$ and $(\Delta x, \Delta y)$ are two local co-ordinate systems around the CMS of the diffraction spot and the grain section respectively.

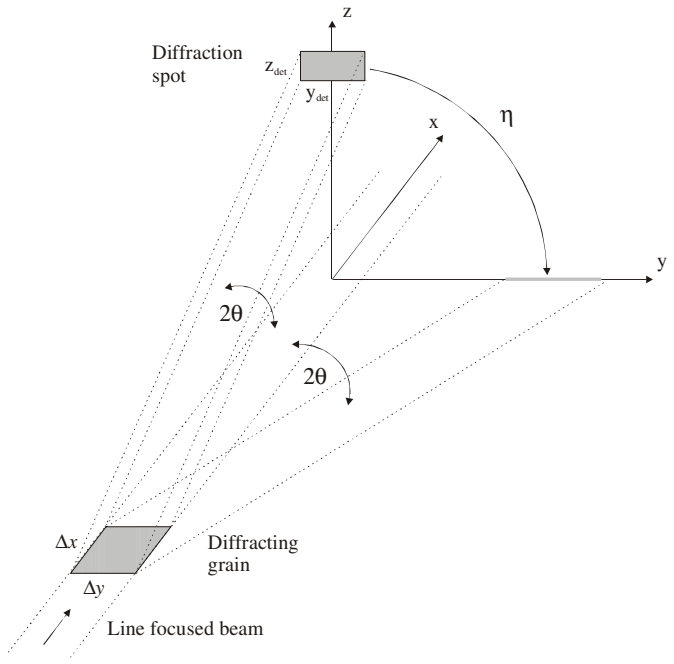


*Fig. 1.5.3. The shape of a diffraction spot corresponds to the shape of the grain in the sample plane. The projection depend on the two angle $2\theta$ and $\eta$.*

If we consider a diffracting grain as an ensemble of points then the diffraction from each of these points will lie on a Debye-Scherrer ring in the diffraction pattern, but the centre position and the radius of the rings will not be identical. The different positions where the diffraction originates in the x-direction determine the radius of the rings, while the positions in the y-direction determine the centre positions in the y-direction of the Debye-Scherrer rings on the detector. If the grain is not a perfect crystal, but has small variations in the crystallo-

graphic orientation, then the intensity in the diffraction spot will spread out along the Debye-Scherrer rings, as in the case of powder diffraction (see section 1.2.3). This spread of the orientation distribution within a grain is called the mosaicity or the mosaic spread. Fig.1.5.4. shows the diffraction from an aluminium sample that suffers from a mosaicity of approximately 6°, where the intensity in the diffraction spots are clearly spread out along the Debye-Scherrer rings. For certain spots, the intensity tails along the Debye-Scherrer rings have different lengths for different parts of the diffraction spots. Long and short tails correspond to regions of a grain where the variations of the orientations are large and small, respectively. A subdivision of a grain in more or less perfect crystal parts can easily be observed in the diffraction spot.
The mosaicity causes, as described, a one-dimensional spread along the Debye-Scherrer rings. A two-dimensional spread will only be observed if the incoming beam diffracted in the sample has a large divergence. At the 3DXRD microscope the divergence is $\alpha \leq 0.5 \cdot 10^{-3}$ rad, and the resulting radial intensity spread on the detector will be $\Delta z = L \tan \alpha \approx 5\mu m$, for a sample to detector distance of L=10mm. The detector has a pixel size of 4.3µm in both directions and the beam divergence will therefore only cause a negligible spread of one pixel on the detector.

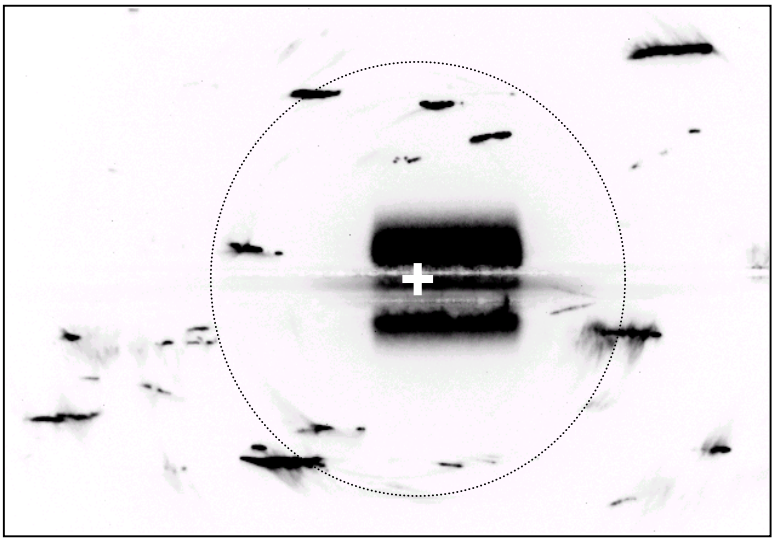

*Fig. 1.5.4. The mosaic spread in the grains result in diffraction spots that are spread out along the Debye-Scherrer rings. The white cross marks the centre of the direct beam and the dotted circle is an illustration of a Debye-Scherrer ring. The diffraction pattern is from a 99.4% commercially pure aluminium sample (the 2S material).*

The mosaic spread can be determined by focusing on one diffraction spot and measuring how much the sample has to be rotated in ω before the diffraction spot disappear. To compare the mosaicity between different spots, it has to be taken into account that the amount of ω rotation a diffraction spot experiences depends on the scattering angle 2θ and the azimuthal angle η of the particular spot. This can be explained with the aid of Fig.1.5.5. The monochromatic beam is diffracted in the sample and the diffracted beam produces a diffraction spot on the detector. The position of the spot is determined by the angles 2θ and η.

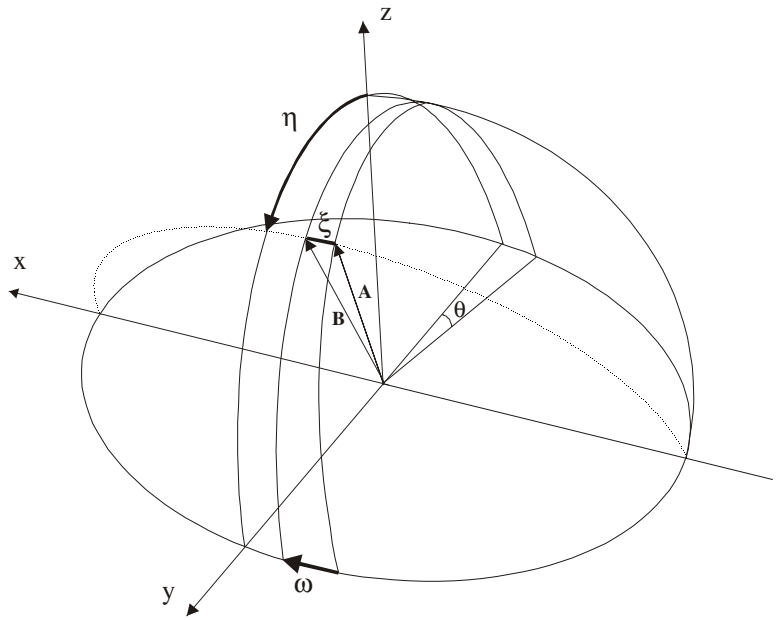


*Fig. 1.5.5. Illustration of a scattering vector A, that by a rotation $\omega$ of the sample, only experience a rotation of $\xi$. The final position of the scattering vector after the rotation is B.*

By inspecting Fig.1.5.5 the normalised scattering vector A can be found to be

$$\mathbf{A} = \frac{1}{N}\begin{pmatrix} 1 \\ \tan\theta \\ \dfrac{1}{\tan\eta} \end{pmatrix} \quad , \quad \textit{where} \quad N = \sqrt{1+\tan^2\theta+\tan^{-2}\eta} \tag{1.5.2}$$

If the sample is rotated by ω then the scattering vector will also be rotated. The rotation of the sample can be expressed as

$$\Omega = \begin{pmatrix} \cos\omega & \sin\omega & 0 \\ -\sin\omega & \cos\omega & 0 \\ 0 & 0 & 1 \end{pmatrix} \tag{1.5.3}$$

After the rotation the new scattering vector B will be given by

$$\mathbf{B} = \Omega\mathbf{A} \tag{1.5.4}$$

The angle ξ between the two vectors, before and after the rotation can now be calculated as

$$\cos\xi = \frac{\mathbf{A}\cdot\mathbf{B}}{|\mathbf{A}|\cdot|\mathbf{B}|} = \mathbf{A}\cdot\mathbf{B} = \cos\omega + \frac{1-\cos\omega}{N\tan^2\eta} \tag{1.5.5}$$

A spot with an $\eta$ value near the equator will experience a rotation that is equal to the actual rotation ω of the sample, while a diffraction spot near the poles (η=0 and π) will experience a smaller effective rotation $\xi$. Exactly at the poles the effective rotation will be zero. In other words the sample has to be rotated more in ω to record the total integrated intensity for a diffraction spot near the poles compared to a diffraction spot near the equator.

In the tracking process a series of images are acquired with a constant step size in ω. If the crystal grains in the sample have a mosaic spread then the total integrated intensity in the diffraction spots will be spread out over several images. It is vital for the tracking technique that the recorded images of the diffraction spots contain the total integrated intensity. Otherwise it will not be possible to determine either the correct intensity weighed centre of mass or the periphery of the diffraction spot, resulting in a projected grain boundary with an incorrect shape at the wrong position in the sample plane.

Oscillating the sample over a range $\Delta\omega$ while recording each image is an effective way to obtain a complete integration of the Bragg intensity. The necessary $\Delta\omega$ value should match the mosaic spread of the grains. The ω value that is oscillated around will not always be at the centre position of the distribution that corresponds to the mosaic spread. This means that even if $\Delta\omega$ is greater than the mosaic spread, it will not prevent the intensity in some diffraction spots from being split between two images. When $\Delta\omega$ is smaller than the mosaic spread, the intensity in one diffraction spot will be distributed between more than two images. The total intensity in a diffraction spot has to be summarised before it is possible to determine the correct grain position and the correct grain boundary shape.

The summation could be carried out by projecting the full two-dimensional intensity distribution into the sample plane. When this is performed for all the images recorded with different ω, that contain intensity from the diffraction spot under investigation, the intensity distributions could be added in the sample plane. This method is very time consuming because the intensity in each pixel in the images has to be projected into the sample plane. It was therefore decided to treat one image at a time and add the projected boundaries in the sample plane. When the intensity in a diffraction spot is split between several images due to mosaicity, this method results in artificial grain boundaries that have to be removed. The diffraction spots that correspond to different parts of the same diffracting grain are easily identified by inspection of the diffraction patterns. The artificial grain boundaries can afterwards be removed by inspection of the data files that contain the (x,y) points of the different projected boundaries. When the sample is larger than the line focused beam, which typically is 800μm, then the sample has to be translated in the y-direction. The tracking has to be performed on several parallel stripes in order to cover a full layer in the sample. This results in grains that only partly exist in two tracking series. Again the result is artificial grain boundaries, but they can be removed by comparing the orientation of the two parts of the diffracting grain. If the misorientation across a reconstructed boundary is less than 0.5°, the boundary has been removed.

Fig.1.5.6 is an example of how different parts of a grain boundary were determined from a diffraction spot where the total intensity was distributed between three images. The images were recorded at $\omega = -2°, 0°, 2°$ with an oscillation of $\Delta\omega = 2°$. The sample was a 99.996% pure aluminium polycrystal. The tracking was performed 10μm below the sample surface, and before the tracking experiment an EBSP image was acquired at the surface. The grain boundaries determined by the X-ray tracking are superimposed as white lines on the EBSP images in Fig.1.5.6

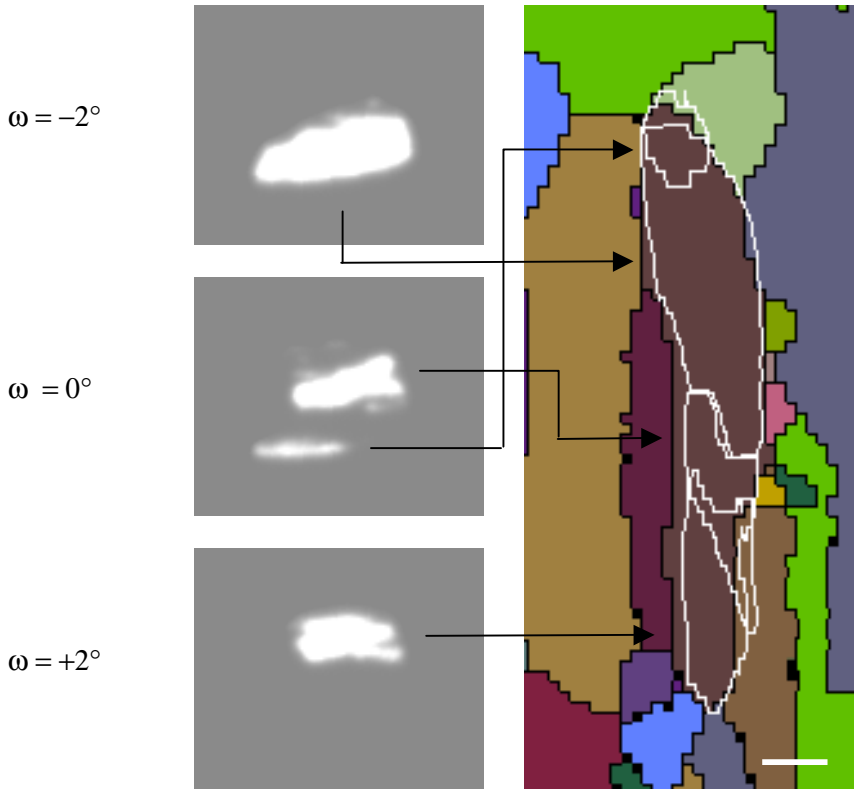


*Fig. 1.5.6. The total Bragg intensity in a diffraction spot is distributed between three images. Left: the same diffraction spot recorded at $\omega = -2°, 0°, 2°$ with an oscillation of $\Delta\omega = 2°$. Right: the different parts of the diffraction spot correspond to different parts of the grain boundary in the sample plane. This is illustrated by the arrows. The white lines are the boundaries determined by the X-ray tracking, superimposed on an EBSP images of the same sample. The white scale bar at the bottom is 100μm.*

### 1.5.3 The periphery of a diffraction spot

The incoming monochromatic beam can be considered as a series of parallel single X-rays in the x-y plane (see Fig.1.5.3). Each ray will be either diffracted or not diffracted in a particular grain. The resulting intensity distributions across a diffraction spot should therefore in theory be a step-function, but this will only be the case for a perfect crystal and a perfect detector. Fig.1.5.7 is an example of the intensity distribution across two diffraction spots. In Fig.1.5.7(a) the intensity distribution is nearly flat at the centre, with some tails reflecting the instrumental resolution and the mosaic spread of the grain. If the grain has a large mosaicity then certain parts of the grain will diffract at a slightly different ω rotation of the sample. Some parts of the intensity will be missing, and the intensity distribution will have local minima instead of a flat plateau at the centre (Fig.1.5.7b).

The variation in the shape of the intensity distributions across the diffraction spots makes it difficult to determine the periphery of the spots. As a first approximation the periphery of the spots can be determined by setting a fixed intensity threshold. The diffraction is stronger from some (hkl) reflections than from others. This can be taken into account by letting the fixed intensity threshold be a function of the maximum intensity of the spot under investigation.

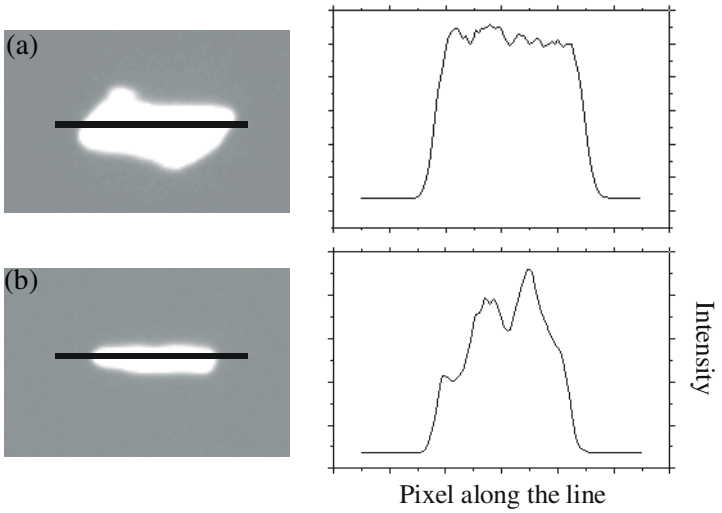


*Fig. 1.5.7. Two diffraction spots (a) and (b) with low and high mosaicity, respectively. The intensity along the black lines was measured and the intensity distributions are plotted next to the diffraction spots.*

In Fig.1.5.8 the periphery of the diffraction spots have been determined by setting a fixed intensity threshold as a percentage of the maximum to background intensity. Afterwards the peripheries have been projected into the sample plane and are in Fig.1.5.8 superimposed as white lines upon an EBSP image of the sample surface. The sample material was commercially pure aluminium (99.4%), the main impurities being Fe (0.33wt%) and Si (0.09wt%). This material is also called aluminium 2S.

The tracking was performed 10μm below the sample surface with a line focused beam ($800\times5\mu m^2$). The sample dimensions of $2.5\times2.5mm^2$ made it necessary to perform the tracking on three parallel stripes to cover the surface. This is the reason why the tracking boundaries for the two grains in the middle of the images have been split into two, compared to the EBSP image. These boundaries are artificial and are only created because the beam size is limited.
The projected grain boundaries are decreasing in size for increasing intensity thresholds for all the grains, as it obviously should. A threshold fixed at 35% of the maximum intensity in the diffraction spots seems to make the misfit between the determined grain boundaries and the EBSP image smallest when averaging all the grains. When looking at individual grains then the tracking boundaries make the best fit with the EBSP image for different thresholds between 30%-60% of the maximum intensities.

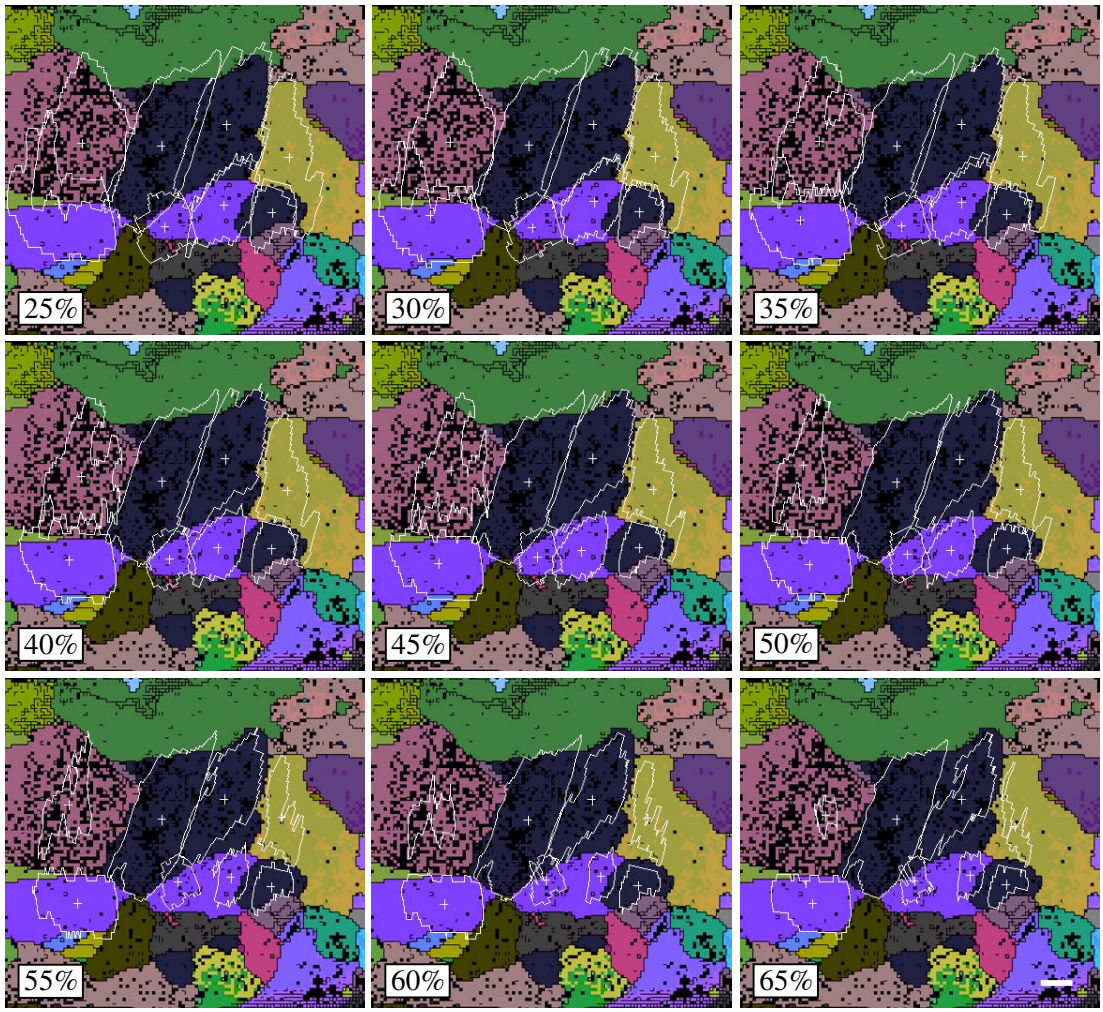


*Fig. 1.5.8. The peripheries of several diffraction spots have been determined by setting a fixed intensity threshold as a percentage of the maximum intensity in the diffraction spots. The projected boundaries are superimposed as white lines on an EBSP image of the sample. The white crosses in the centre of the spots are the intensity-weighted centres of mass in the diffraction spots projected into the sample plane. The white scale bar in the right corner is 200μm.*

Another and more consistent way to define the periphery of a diffraction spot is to approach the spot from all directions on separate lines. The edges of a diffraction spot can then be defined in these intensity profiles as the points where the profiles have the steepest slopes. By combining all the edge points we get the periphery of the spot. When using a fixed threshold on a diffraction spot where some intensity is missing due to mosaicity, a local minimum close to the edges of the spot would cause the spot to appear smaller than it actually is. This would be the case for the diffraction spot in Fig.1.5.7(b) if the threshold were fixed at 40%. When the steepest slope approach is used on Fig.1.5.7(b) it is much more likely to determine the correct periphery of the diffraction spot, but it should be underlined that edge finding always will be a matter of definitions. In this thesis the steepest slope approach have been chosen, because it gives boundaries with the smallest misfit compared to the boundaries in the EBSP images and because the image processing program *Image Pro* has an automatic routine to find the edge of any object by this technique. With the exception of Fig.1.5.8 all images that show reconstructed grain boundaries from the tracking

data have been determined by using the *Image Pro* routine to find the edges of the corresponding diffraction spots.

### 1.5.4 The grain boundary position

The tracking algorithm is based on acquiring a series of images of the same diffraction pattern while the detector is translated away from the sample (see Fig.1.5.1). If individual points on the peripheries of the same diffraction spot in this series could be identified, then corresponding points could be fitted and extrapolated into the sample plane. The identification of individual points is unfortunately not possible. Instead it was decided to determine the peripheries of corresponding diffraction spots in the series and calculate the intensity-weighted centre of mass (CM) of all the pixels within these peripheries. The CM values were then fitted by a straight line and the determined angles $2\theta$ and $\eta$ were used to project all points on the periphery of the diffraction spot recorded at the closest distance to the sample into the sample plane. The shortest possible distance between the sample and the detector ensures the lowest effect of any divergence in the diffracted beam on the diffraction spot.
When the sample is rotated, several different reflections will be observed from the same grain as different diffraction spots. When the periphery of these spots have been determined they can be projected into the sample plane by their respective directions and they should correspond to exactly the same grain boundary in the sample plane. This will only be the case if the sample is perfectly aligned in the centre of the $\omega$ rotation. If it is not perfectly aligned then the vertical axis of the sample will not be identical with the rotation axis and the rotation will make the sample swing around in the shape of a cone (see Fig.1.5.9).

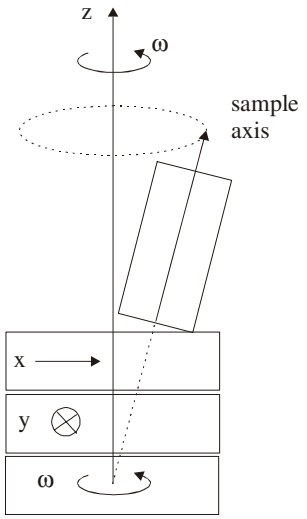


*Fig. 1.5.9. If the sample is not perfectly aligned then the vertical sample axis will turn around like a cone when the sample is rotated in $\omega$. In the projection of the periphery of the diffraction spots it is assumed that the sample axis is aligned with the rotation axis. The periphery of the diffraction spot will therefore be projected back to a wrong position in the sample plane that is not identical with the boundary of the actual diffracting grain.*

Even if the sample is very carefully aligned there will always be some sphere of confusion due to the precision of the translation and rotation stages. This error can be minimised by using several reflections from the same grain and minimising the misfit between their respective projected peripheries in the sample plane. The parameters that have to be fitted are the $\omega$ rotation, the sample translations

x and y, the sample-to-detector distances and the position of the direct beam on the detector. This fit was optimised by visual inspection of the misfit between the projected peripheries of different reflections from the same grain. The most important parameter was found to be the position of the sample relative to the ω rotation axis, e.g. the sample translations in x and y. Visual inspection is not the best way to determined a global minimum, but a large improvement was achieved by this fit even though it was not possible to get all the projected peripheries of different reflections from the same grain to be identical in the sample plane. In Fig.1.5.10 the determined grain boundaries from three different reflections from the same grain have been superimposed as white lines on an EBSP images of the same Al sample. The tracking was performed 10μm below the sample surface.

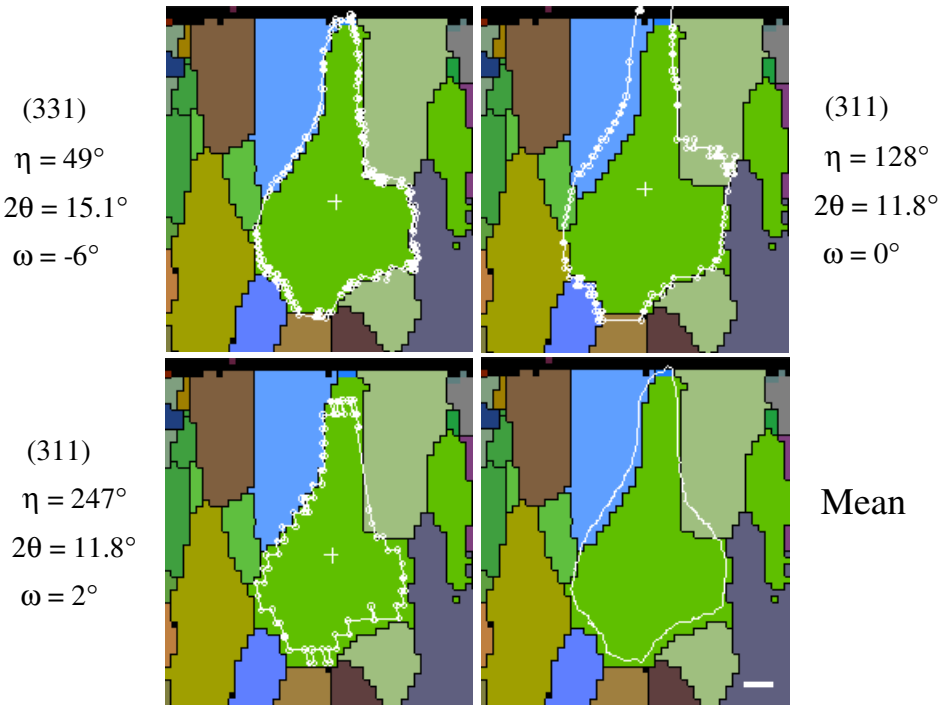


*Fig. 1.5.10. The boundary of one grain determined from three different reflections. The image in the lower right corner is the calculated mean of the three boundaries. The white scale bar in the right corner is 100μm.*

The variations of the shape of the determined boundaries in the sample plane are partly caused by the fit. Only a local minimum has been determined. Another reason for the variation is that different peripheries are projected in different directions. Depending on the η angle, each projected periphery will have a large uncertainty in one direction and a small uncertainty in the perpendicular direction. For η=0 the uncertainty of the determined boundary will be large in the x-direction and small in the y- direction (see Fig.1.5.3).
It was attempted to take the dependence of the projection direction into account when comparing the boundaries with the EBSP image by averaging the determined boundaries from different reflections from the same grain. This was done by selecting a centre point of the grain and rotating a straight line around the centre point. The mean grain boundary was then determined by averaging the points where the straight line intersects the boundaries from different reflections. The proper way of weighting the uncertainties in this averaging was unfortunately not determined. Fig.1.5.10 shows the calculated mean of three dif-

ferent boundaries of the same grain where the uncertainties have not been taken into account. By comparing the misfit between the determined boundaries and the EBSP image we see that the boundary from the (331) reflection has the smallest misfit. It was therefore decided to use single reflections in all plots of determined boundaries instead of averaging between boundaries from different reflections that in principle should improve the result.

### 1.5.5 Experimental results

The tracking technique is a non-destructive technique for bulk studies, but due to the novelty of the technique it was necessary to carry out the experiments in such a way that it is possible to compare the results with standard techniques. As a validation test of the technique a coarse-grained 99.996% pure aluminium sample was investigated. The sample was first annealed for 12 hours at 500°C and slowly cooled to minimise the mosaic spread in the grains. One sample surface was polished and the grains at this surface were mapped by electron microscopy. The EBSP image was acquired with a step size of 20µm. The range of orientation variations within the grains was found to be less than 1°. Next, the sample was aligned with the same surface parallel to the beam at the 3DXRD microscope and the tracking procedure was performed with a line focused X-ray beam (800×5µm$^2$) incident 10µm below the surface. The sample dimensions were 2.5×2.5mm$^2$, making it necessary to acquire information from three stripes across the sample. With 1 second exposure time, 22 ω-settings with $\Delta\omega = 2°$ and $L = 7.5, 10.3$ and $13$mm, the total data acquisition time was less than 2 minutes. The speed of this technique should be compared with conventional diffraction set-ups for depth resolved studies using slits formed as pinholes, grids (Wroblewski *et al.*, 1999) or cones (Paper **A**) before and/or after the sample, which lead to very slow data acquisitions.

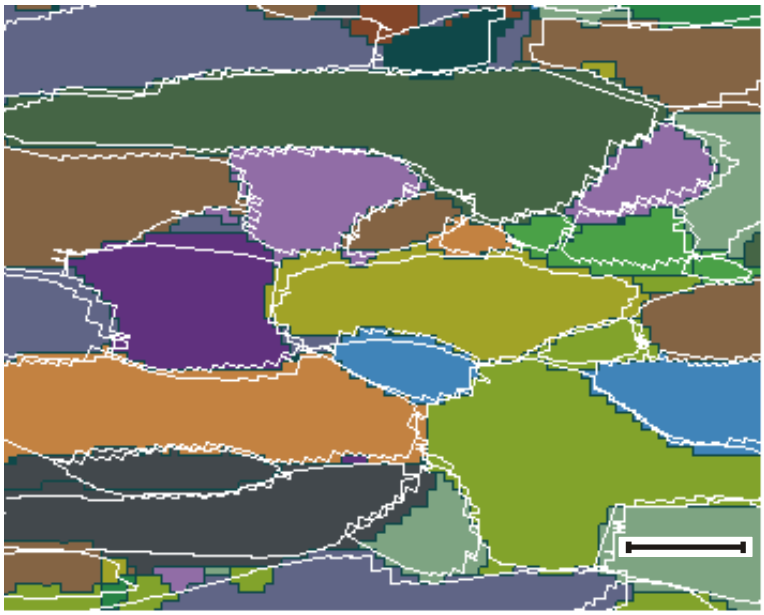

*Fig. 1.5.11. The determined grain boundaries from the tracking experiment are superimposed on an EBSP image of the sample surface. The colours of the grains in the EBSP image indicate the macroscopic orientation of the grains. The scalebar in the image is 400µm.*

The resulting grain boundaries determined by the two different techniques are superposed in Fig.1.5.11. The black lines in the figure indicate the grain boundaries as determined by electron microscopy (EBSP), and the white lines indicate the grain boundaries resulting from the synchrotron experiment. The tracking boundaries are raw data from single reflections with no interpolation or averaging between reflections from the same or neighbouring grains. The misfit between the tracking and the EBSP boundaries have been found by linear intercept to be 26μm in average with a maximum of 40μm. Maps of the grain boundary structure determined by the tracking technique will thus be of sufficient quality for many applications. For example, in recrystallisation studies the evolution of separate nuclei can be followed during annealing (Lauridsen *et al.*, 2000a), and in estimates of grain-to-grain interactions where centroid descriptions often are sufficient. To increase the quality of the maps, software is presently being developed that makes use of the inherent crystallographic features. This includes automatic procedures for interpolation between reflections from the same and neighbouring grains. All tracking results in this thesis have been calculated by hand with the exception of the orientations of the grains.
The colours of the grains in Fig.1.5.11 indicate different grain orientations from the EBSP measurement. The EBSP was acquired on a standard JEOL840 SEM microscope where it is not possible to align the sample relative to the microscope axis with a sufficient precision. The tilts of the sample are normally corrected by eye. It is therefore not possible to compare the determined macroscopic orientation from the EBSP measurement and the tracking experiment. Relative changes in the orientation like the misorientation across a grain boundary can on the other hand easily be compared.
The misorientations across the grain boundaries in Fig.1.5.11 have been calculated from the tracking data as described in app. A1 and found to be equal to the EBSP measurement with an uncertainty of less than 1.2°. This misfit between the calculated misorientations from the two techniques is partly due to the combined uncertainties of the measurements in the set-ups and partly due to the way the misorientations were calculated. The misorientations were found from the EBSP data by calculating the misorientation between the average of 10 measured point on each side of the grain boundaries in contrast to the tracking technique where all points within the grain area automatically are averaged when the orientation of a grain is determined. In the calculation of the orientation of a grain the $2\theta$ and $\eta$ values are used to define the reflection. These angles are determined by the linear fit through the calculated intensity weighted CM values of the corresponding diffraction spots. In case of mosaicity the CM values of the diffraction spots will be wrong resulting in not only a wrong position and shape of the reconstructed grain boundary but also in a wrong calculated orientation of the grains. In the present experiment the mosaicity was 1° and the sets of reflections from the same grains only had a variation of less than 0.1° relative to their theoretical calculated G-vectors.

## 1.6 X-ray tomography

Synchrotron X-ray tomography in combination with grain boundary wetting is another technique that is capable of mapping grain boundaries in three dimensions. When aluminium is exposed to liquid gallium (Ga), then the Ga will diffuse along the aluminium grain boundaries. Direct observation of the penetration process is difficult as the phenomenon takes place in the bulk of the sample but synchrotron radiation X-ray microtomography has proven an adequate tool

for the observation of wetted grain boundaries in the Al-Ga system (Ludwig & Bellet, 2000).
The large difference in the linear X-ray attenuation coefficient between Al and Ga allows the detection of submicron Ga layers in the bulk of millimetre sized Al samples. Tomographic reconstruction from a series of two-dimensional projections of the sample yields the three-dimensional distribution of the attenuation coefficient and clearly reveals where Ga is present within the bulk of the Al sample.
The combined effect of the high spatial resolution (~1μm) in Synchrotron X-ray tomography and the short acquisition times (~2 minutes for a complete scan) makes the technique ideal for studying the wetting process of the Al grain boundaries. The crystallographic orientations of grains can however not be determined by X-ray tomography. To investigate the importance of the grain orientations for the wetting process a combined X-ray tomography and tracking experiment was carried out.
In this section the tomography technique and the concept of tomographic reconstruction will be described. The theory of grain boundary wetting by liquid metal will be outlined, and the tomography experiment that was carried out will be discussed and compared with tracking results from the same sample. The experimental results have been published (Paper **E**).

### 1.6.1 The transmission tomography technique

Tomography is a quantitative description of a slice of matter within a bulky object, and can be achieved by several different techniques; ultrasonic, magnetic field, X-ray, γ-ray and electrical field tomography. The first tomographic images were obtained in 1957 (Bartolomew & Casagrande, 1957) but most industrial applications were first developed in the 1980's when high speed and high memory computers became generally available. In principle there are only three different ways to make the experimental set-up for transmission tomography. The incoming beam can travel along parallel paths or the beam can have a large divergence in one or two directions (a fan-beam or a cone-beam). In synchrotron X-ray tomography the beam divergence is negligible. It can therefore be assumed that all photons are travelling along parallel paths with no loss of intensity due to beam divergence.
The linear attenuation coefficient is correlated to the photon energy E and the atomic number Z of the material under investigation through the relation

$$\mu = K\frac{Z^4}{E^3}\rho \qquad (1.6.1)$$

where $K$ is a constant and $\rho$ is the density of the material. The linear attenuation coefficient decreases with increasing energy and the low-energy photons will be preferentially absorbed compared with high-energy photons for a polychromatic X-ray beam. The mean energy of the exit beam will be higher than the mean energy of the incoming beam. This is normally referred to as *beam hardening* (Kaftandjian *et al.*, 1996) and will lead to erroneous reconstructed maps of the attenuation. This is, however, easily avoided by using a monochromatic beam. In this thesis work only the case of a monochromatic X-ray beam with no divergence will be considered.
When a sample is placed in an X-ray beam the transmitted beam will be a function of the attenuation through the thickness of the object. If the transmitted beam is recorded on a detector the images will correspond to a projection of the absorption through the whole sample. By combining different projections of the absorption, transmission tomography can produce a map of the linear attenua-

tion coefficient. Transmission tomography is so to speak based on the attenuation law

$$N_1 = N_0 e^{-\int_{path} \mu(x,y)dx} \tag{1.6.2}$$

where $\mu(x,y)$ is the linear attenuation coefficient at the point $(x,y)$. In this equation only one ray is considered and the integral is performed over the straight line that corresponds to a constant $y$ value. By measuring the number $N_0$ of photons in the incident beam and the number $N_1$ of photons transmitted along a single line through the sample it is possible to calculate the line integral of $\mu$ along the line as

$$\ln \frac{N_0}{N_1} = \int_{path} \mu(x, y)dx \tag{1.6.3}$$

The set of measured parallel lines is called a *projection*. Another projection can be achieved by rotating the sample and a set of a sufficient number of projections can be used to reconstruct the linear attenuation coefficient.

### 1.6.2 Tomographic reconstruction

The purpose of the tomographic reconstruction is to build a two dimensional representation of the linear attenuation coefficient from a set of projections acquired from a number of different points of view. The linear attenuation coefficient $\mu(x,y)$ is illustrated in Fig.1.6.1 together with its projection $p(r,\omega)$ for a rotation angle $\omega$ of the sample. The $(x,y)$ co-ordinate system is attached to the sample and the rays from the source to the detector is defined by the parameters $(r,\omega)$ where $\omega$ is the sample rotation and $r$ is the distance from the rotational centre.
Each line that the X-rays travels along in Fig.1.6.1 can be described by the relation

$$r = x\cos\omega + y\sin\omega \tag{1.6.4}$$

If $\omega$ is plotted as a function of $r$ one gets a so-called *sinogram* because a point of the object describes a sinusoid in this representation.

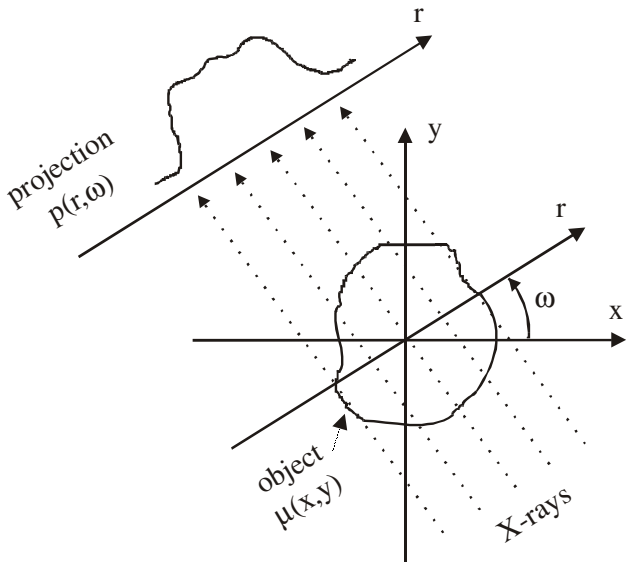


*Fig. 1.6.1. The illustration shows the object function (x,y) and its projection $p(r,\omega)$ at a rotation angle $\omega$ of the sample.*

Having acquired a set of projections from different angles of the sample the information in all the projections have to be combined and projected back to achieve the linear attenuation coefficient. An intuitive way of performing this backprojection is to assign to each point of the object the average value of all the projections at the corresponding location (see Fig.1.6.2).

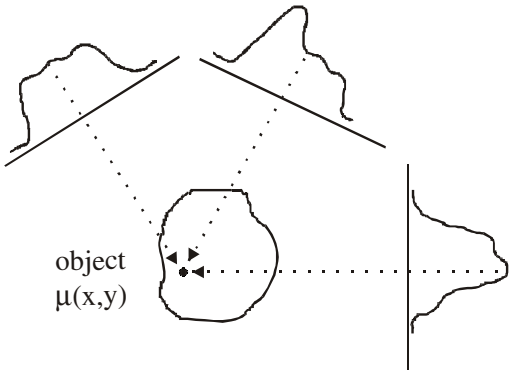


*Fig. 1.6.2. Backprojection of one point in the object by averaging the corresponding values in all the projections.*

This simple procedure will unfortunately result in a blurred reconstruction because a blurred version of the whole object will be added to each pixel. Prefiltering the projections can do an exact mathematical correction of the blurring and this is utilised in the so-called filtered backprojection algorithm. This reconstruction algorithm is based on the Fourier slice theorem. It states that the one-dimensional Fourier transform $\hat{p}(R,\omega)$ of a parallel projection $p(r,\omega)$ in the $\omega$ direction is equal to a slice in the same direction $\omega$ of the two-dimensional Fourier transform $\hat{\mu}(\nu_1,\nu_2)$ of the original function $\mu(x,y)$. The theorem is illustrated in Fig.1.6.3 and can be mathematically expressed as

$$\hat{\mu}(R\cos\omega, R\sin\omega) = \hat{p}(R,\omega) \tag{1.6.5}$$

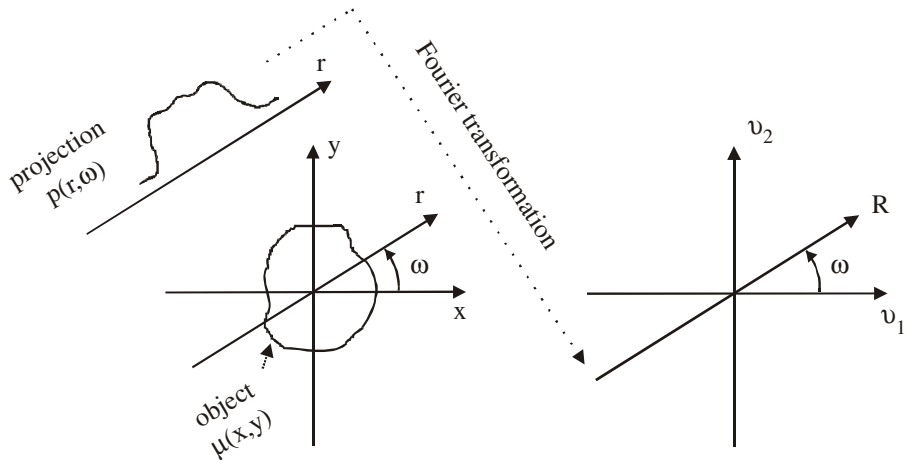


*Fig. 1.6.3. The Fourier transformation of a projection corresponds to a line through the $(\nu_1,\nu_2)$ Fourier space with the same angle $\omega$.*

The inverse two-dimensional Fourier transform of $\hat{\mu}(\nu_1, \nu_2)$ is

$$\mu(x, y) = \int_{-\infty}^{\infty}\int_{-\infty}^{\infty} \hat{\mu}(\nu_1, \nu_2) e^{2\pi i(\nu_1 x + \nu_2 y)} d\nu_1 d\nu_2 \tag{1.6.6}$$

by using the polar co-ordinates $(R, \omega)$ in the $(\nu_1, \nu_2)$ Fourier space this can be rewritten as

$$\begin{aligned} \mu(x, y) &= \int_{0}^{2\pi}\int_{-\infty}^{\infty} \hat{\mu}(R\cos\omega, R\sin\omega) e^{2\pi i R(x\cos\omega + y\sin\omega)} R dR d\omega \\ &= \int_{0}^{\pi}\int_{-\infty}^{\infty} \hat{p}(R, \omega) e^{2\pi i R(x\cos\omega + y\sin\omega)} |R| dR d\omega \end{aligned} \tag{1.6.7}$$

which is the central equation in the filtered backprojection algorithm. This equation tells us that by recording projections of the linear attenuation coefficient and Fourier transforming each of these, then the values of $\hat{p}(R, \omega)$ can be determined on radial lines as shown in Fig.1.6.3. If an infinite number of projections are recorded then $\hat{p}(R, \omega)$ would be known at all points in the $(\nu_1, \nu_2)$ plane, and the linear attenuation coefficient can then be recovered by an inverse Fourier transformation.

The evaluation of Eq. (1.6.7) can be split in two steps. The first integral to be evaluated is

$$HDp(r, \omega) = \int_{-\infty}^{\infty} p(R, \omega) e^{2\pi i R r} |R| dR \tag{1.6.8}$$

which is the filtering operation of the projection $p(r, \omega)$. The filter is noted HD because it is the Hilbert transform of the first derivative. The effect of the filter is the creation of negative values in the filtered projections that compensate for contributions from other projections.

The remaining integral in Eq. (1.6.7) is the backprojection of the filtered projections

$$\mu(x, y) = \int_{0}^{\pi} HDp(r, \omega) d\omega \tag{1.6.9}$$

which provides the two-dimensional map of the linear attenuation coefficient. To obtain a three-dimensional map we just have to apply the same algorithm on a stack of slices through the sample.

It should be noted that the analytical expressions have to be made discrete in the implementation of this algorithm. For a discussion of the discretization see Kak & Slaney (1988).

### 1.6.3 Grain boundary wetting

Many metals and ceramics experience penetration of capillary liquid films along the grain boundaries when wetted with chemically compatible liquids (Clarke & Gee, 1992). The grain boundary wetting changes the electrical and mechanical properties of the grain boundaries. If it is possible to control the wetting process, the method can be used to design and manufacture new electrical ceramics, and optimise the high-strain-rate superplasticity phenomenon, where a critical amount of liquid phase for the optimisation of grain boundary sliding during superplastic deformation has been observed (Higashi *et al.*, 1995). High-strain-rate superplasticity is utilised in the automobile and the semi-conductor industries in the near-net-shape forming techniques.

When a normally ductile metal comes in contact with a liquid metal it can sometimes lose its ductility. If the sample is stressed while in contact with the liquid metal it will cause a brittle fracture at a stress level much below the fracture strength of the material in air (Fernandes & Jones, 1997). This phenomenon is called liquid metal embrittlement. In some cases the liquid metal penetrates into the bulk of the sample even when no external stress is applied. Liquid Ga with a melting point of 29.8°C causes for example brittle fracture in polycrystalline Al and penetrates into the sample along the grain boundaries without any applied stress.
It has been attempted to regard the penetration as a wetting process of the grain boundaries and thereby to reduce the problem to a grooving problem where the equilibrium dihedral angle θ at the liquid-to-solid metal interface is

$$\theta = 2\cos^{-1}\left(\frac{\gamma_{gb}}{2\gamma_{Ga/All}}\right) \tag{1.6.10}$$

where $\gamma_{gb}$ is the grain boundary energy and $\gamma_{Ga/Al}$ is the energy of the liquid metal at the interface. When $\gamma_{gb} \geq 2\gamma_{Ga/Al}$ the dihedral angle θ becomes zero and the liquid metal will start to wet the grain boundary (Straumal *et al.*, 1994). Fig. 1.6.4(a) illustrates a Mullins groove (Mullins, 1957).

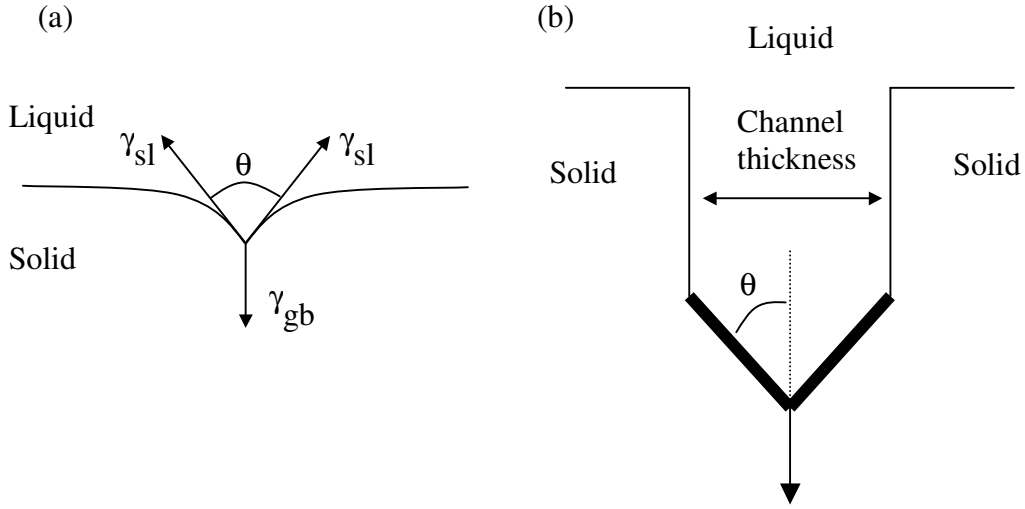


*Fig. 1.6.4. Illustrations of (a) a Mullins groove. (b) a grain boundary channel with a wedge shaped penetration front.*

A description of the penetration as a pure wetting process can not explain that a micrometer thick liquid layer is formed in the grain boundaries. To account for this several models have been proposed (Rabkin, 1998 and Desre, 1997).
One way of regarding the penetrating liquid is as a moving planar defect (Hugo & Hoagland, 1998). The Ga penetration can be compared to crack propagation by including the strain energy in the expression for the driving force. The net driving force for penetration of a thin Ga layer into an aluminium grain boundary is then the rate of change of the Gibbs free energy G of the system with respect to the grain boundary area.

$$-\frac{\partial G}{\partial A} = -\frac{\partial E}{\partial A} - 2\gamma_{Ga/Al} + \gamma_{gb} \tag{1.6.11}$$

where E is the strain energy of the solid, A is the area in the grain boundary plane, $\gamma_{Ga/Al}$ is the interfacial free energy between liquid gallium and solid aluminium, and $\gamma_{gb}$ is the grain boundary energy. The negative area rate of change

of the strain energy is the so-called crack driving force. The penetration of liquid Ga is seen in TEM observations (Hugo & Hoagland, 1998) to produce strain, and the driving force could be negative. The penetration occurs on the other hand without any external stress. For a long penetration distance the solid behind the penetration front will be left strain free, and if there is no other sources of strain energy that interact with the penetration front then the crack driving force is zero. This means that if $\gamma_{Ga/Al}$ is constant then the free energy change will only depend on the grain boundary energy $\gamma_{gb}$. The net driving force will then be positive for high energy boundaries and the penetration will happen spontaneously. Low energy boundaries, like twin boundaries and low sigma boundaries will not be penetrated without an applied stress. Hugo and Hoagland have found that this model is consistent with their in-situ TEM observations.
Rabkin (1998) goes a step further and tries to explain the formation of thick Ga layers by suggesting that the observed stress field is caused by a coherency strain in the bulk diffusion zone at the penetration front. Rabkin describes the penetration channel as a grain boundary groove that has a wedge-like shape in the penetration front and this region is regarded as coherently strained, see Fig.1.6.4(b). In the region where the channel walls are parallel the coherency is lost. For an elastically isotropic solid Rabkin finds that the thickness of the grain boundary channel is determined by the elastic properties of the solid, the diffusion coefficient in the solid and the kinetic properties of the interface between the solid and the liquid. The main drawback with these calculations is that it is necessary to assume that the diffusion across the liquid-solid interface is as slow as the volume self-diffusion in the solid if the calculated channel widths should fit the experimental values of 0.1-1μm. This assumption contradicts the available experimental data on dissolution rates in couples of liquid and solid metals (Glickman & Nathan, 1999).
At present the kinetics of the penetration process is not fully understood even though LME has been studied since 1874 where the process of liquid metal embrittlement was described for the first time by W.H. Johnson (1874). The experimental techniques used to investigate the penetration process of liquid metal have mainly been transmission electron microscopy (TEM) and scanning electron microscopy (SEM) but these techniques are limited to sample surfaces or thin foils. Synchrotron X-ray tomography on the other hand makes it possible to analyse and visualise the positions of the liquid Ga within the bulk of the sample. It is therefore expected that this technique will provide new information on the kinetics of the penetration process.

### 1.6.4 The tomography and tracking experiment

An issue presently being discussed is how grain boundaries of different types (i.e. between grains of different crystallographic orientations) are wettet by liquid metal. The dependence of the wetting kinetics upon the grain boundary properties is presently unknown as previously described. To get further information on this a polycrystalling A1 sample with Ga decorated grain boundaries was investigated both by synchrotron X-ray tomography and the X-ray tracking technique. Both techniques provide a map of the grain boundaries but only the X-ray tracking makes it possible to calculate the orientation of individual grains.
A coarse-grained 99.996% pure cylindrical aluminium sample with a diameter of 800μm was investigated. The sample was first annealed for 12 hours at 500°C and slowly cooled to minimise the mosaic spread in the grains. In order to promote surface wetting by liquid Ga, the sample was dipped in a 10% NaOH solution for about 30 seconds to remove the aluminium oxide layer cov-

ering the surface. The sample was immediately afterwards exposed to liquid Ga by depositing a Ga droplet on the sample surface.
The X-ray tomography experiment was performed at ID19 at ESRF. A monochromatic beam of 15keV was reflected in a multi-layer at a glancing angle of 1°. In this manner the beam was spread out to be 1mm$^2$ when it was incident on the sample. A two dimensional detector was positioned after the sample to record the absorption contrast. The high-resolution detector system (see Fig. 1.6.5) is based on a YAG-crystal (Ge) that transforms the X-rays into visible light which by microscope optics is projected on a CCD camera with an effective pixel size of 0.98 µm. The recorded image is the projection of 1mm$^2$ of the sample in the direction of the incoming beam. The sample was careful aligned in such a way that one row of pixels on the detector corresponds to one horizontal slice through the sample. By rotating the sample the features in the sample that cause the absorption can be studied from all directions, and the same row of pixels in all the images will correspond to the different projections of the same slice through the sample.

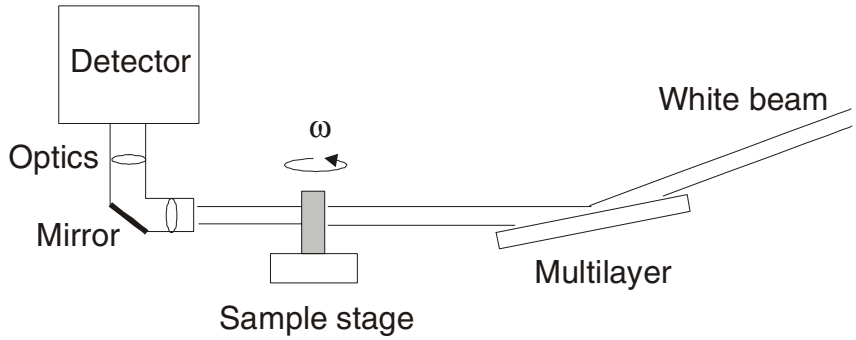


*Fig. 1.6.5. Illustration of the experimental tomography set-up. The sample is rotated from $\theta = 0°$ to 180° and 2D projections are recorded for each angular position $\theta$.*

Series of two-dimensional projections were recorded while the sample was rotated from θ = 0° to 180° with a step size of 1°. Typical full scan times were in the order of 2 minutes. The scan was repeated over several hours in an attempt to observe the kinetics of the wetting process.
The tracking experiment was later performed on the 3DXRD microscope at ID11 at ESRF. The incoming beam was focused to 5µm in height and limited in width to 800µm by slits. The cylindrical sample was 800µm in diameter and in order to cover a full layer in the sample it was translated ±300µm along the y axis and the tracking was performed twice. Images were acquired at three different detector positions (L = 6, 8 and 10mm), and 30 ω-settings with Δω=2°. The data acquisition time was typically of the order of 11 minutes for one layer in the sample. Totally 41 layers were mapped with a step size of 20µm.
The three dimensional capability of the tracking technique is illustrated by four different layers in Fig.1.6.6. The distance between the layers is 100µm. The full lines in the figure show the grain boundaries as determined by the X-ray tracking. The misfit in the position of grain boundaries from neighbouring grains is at the worst 40µm. The determined grain boundaries in Fig.1.6.6 represent the raw data with no interpolation or averaging. A better fit of the grain boundary could be obtained by averaging between the different reflections from the same grain or taking the neighbouring grains into account.

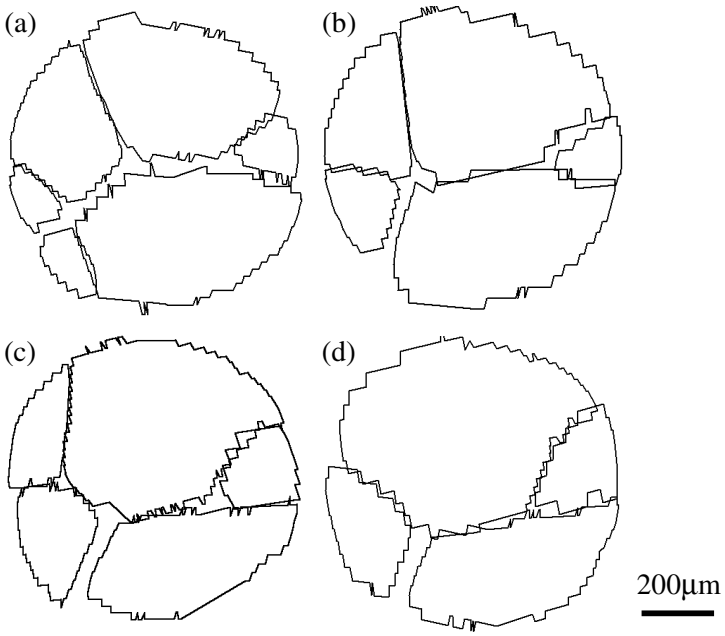


*Fig. 1.6.6. Four sections through the cylindrical Al sample reconstructed by X-ray tracking. The full lines correspond to the determined grain boundaries. The depth of the four sections from the top of the sample are: (a) 100µm (b) 200µm (c) 300µm (d) 400µm.*

The results from the two experiments are illustrated in Fig.1.6.7. Each of the four rows in the figure corresponds to one section through the sample, normal to the sample axis. The sections are 100µm apart and the first layer is 100µm below the sample surface. The images on the left are the tomographic reconstructions where the grey lines indicate the grain boundaries decorated with Ga. The images in the middle show the grain boundaries determined by both techniques superimposed. Grey and white lines correspond to the grain boundaries determined by the tomography and the X-ray tracking, respectively. The spatial resolution in the tomography experiment is 0.98µm and is therefore superior to the tracking technique in determining the position of the grain boundaries. On the other hand the tracking technique detects all the grain boundaries and not only those decorated with Ga (see Fig.1.6.7).
The X-ray tracking provides maps of the grain boundaries based on the orientations of the grains and a macroscopic orientation of each grain can be calculated (see App. **A**). The misorientations between neighbouring grains are listed in the schematic representations of the determined grain boundaries for the four sections at the left in Fig.1.6.7. Full lines correspond to boundaries determined by both techniques and dotted lines to boundaries only detected in the tracking experiment.
At present only two boundaries that are not decorated with Ga have been detected by the tracking technique, one low and one high angle boundary. The low angle boundary maintains a misorientation of 3.7° and is not decorated with Ga in either of the sections. The high angle boundary shows a change of 0.4° in misorientation and change from decorated to not decorated with Ga in the last two sections. It is interesting to note that this boundary does not become decorated at approximately the same layer where the small grain that is present in the bottom left corner in the first two sections disappears. There could be several

explanations for this, for example relating to the grain boundary energy as a function of misorientation angle or grain boundary plane normal relative to the macroscopic sample axes. Also the boundary may be wetted, but with considerably less Ga.
The accuracy of the orientation measurements is difficult to estimate but in the present experiment the tracking was performed at two different y translations of the sample to cover the whole section. Some of the grains were therefore divided in two, and only a part of the grain boundary of these grains could be recovered from each of the two different trackings. This resulted in artificial grain boundaries that were removed afterwards. The misorientation across these artificial grain boundaries was found to be 0.1° in average, with a maximum of 0.2° and this illustrates the precision of the orientation measurements.

The combination of the high spatial resolution in X-ray tomography and orientation measurement from the X-ray tracking technique makes it possible to investigate correlations between the amount of Ga present in the boundaries and the grain boundary parameters, including misorientation and boundary plane normal. The only problem is that the high precision from the tomography is lost for the interesting boundaries that stop getting decorated with Ga and we would in this case have to use the tracking data with a lower spatial resolution to determine the boundary plane normal. Due to the limited time for this project it was not possible to determine any correlation between the amount of liquid Ga in the Al grain boundaries and the grain boundary parameters.

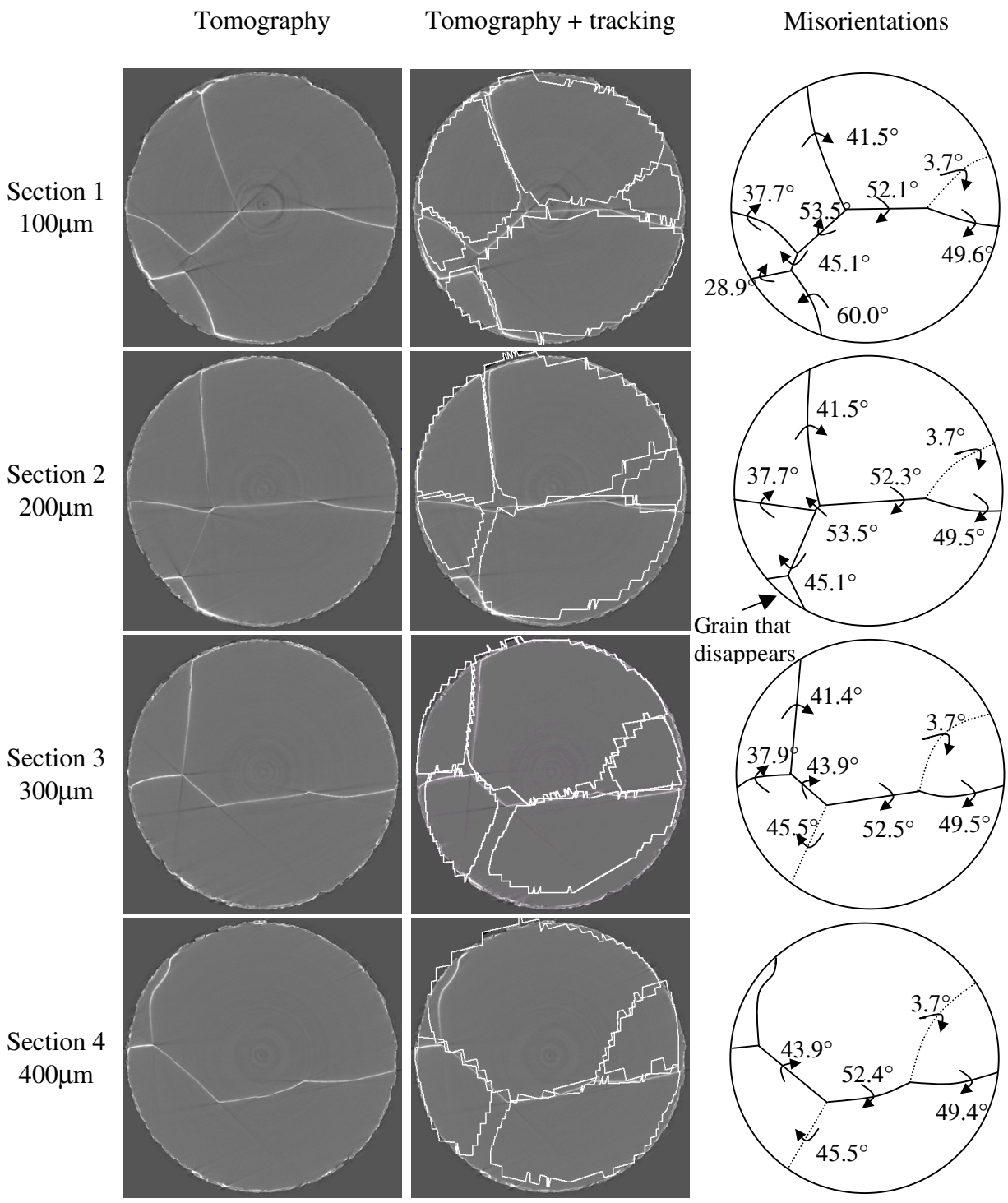


*Fig. 1.6.7. Four sections 100µm apart through the cylindrical Al sample. The sample diameter is 800µm. The images at the left represent the tomographic reconstructions. Grey lines correspond to Ga decorated grain boundaries. In the middle the boundaries determined by the tracking technique are superimposed as white lines on the tomographic reconstructions. The schematic illustrations at the right shows the grain boundaries determined by both techniques (full lines) and only by the tracking technique (dotted lines). The calculated misorientations between neighbouring grains are written on the boundaries.*

# 2 Deformation of aluminium

An electron microscopy investigation of uniaxially compressed aluminium was carried out during a four month stay at Ecole National Superieure des Mines de St. Etienne, France in the Microstructures and Processing Department. Both aluminium single crystals and polycrystals were investigated.
This chapter contains an introduction to the basic theory of plastic deformation and the standard models to predict texture evolutions, followed by a summary of the most general features in deformation microstructures observed by others in tensile deformed aluminium. The principle of the electron back scattering pattern (EBSP) technique is described and it is demonstrated how the mean orientation can be calculated from an EBSP scan. The compression experiments are described and the results from the investigation of aluminium single crystals and polycrystals are finally discussed.

## 2.1 Aim

Plastic deformation of fcc metals results in characteristic dislocation boundaries that subdivide the grains into regions that are rotated with respect to each other. The dislocation features that are developed constitute the deformation microstructure. The dislocation boundaries have many characteristics that are determined by the applied stress and strain in a more or less regular way. Many attempts have been made to find correlations that links parameters describing the microstructure with the deformation process in order to further the understanding of microstructural evolution during deformation. The goal is in time to obtain parameters that can be used in material models that relate material properties to microstructures and processing. The deformation microstructure has mostly been studied in samples deformed in tension or rolling. The aim in this part of the thesis is to use the electron back scattering pattern (EBSP) technique to describe the deformation microstructure and the texture evolution in samples that are deformed in compression to different strain levels. Both aluminium single crystals and polycrystals have been investigated. Large grains in polycrystals may in most cases be regarded as single crystals, except near the edges. Single crystals have the advantage that the orientations are known both before and after the deformation, contrary to grains in a polycrystal, where it is impossible to find the orientation of individual grains before the deformation by standard techniques. Most of the electron microscopy work was therefore carried out on deformed aluminium single crystals.
This electron microscopy investigation also provides a measurement of the deformation-induced mosaicity of the samples at different strain levels. The mosaicity is an important parameter for the X-ray tracking technique, because it sets the limit for when the tracking technique can be used. Special attention was therefore paid to calculations of the spread of the orientations in the EBSP data of aluminium single crystals deformed in compression to different strain levels.

## 2.2 Plastic deformation

Contrary to elastic deformations where the atoms will go back to their initial positions when the load is lifted, plastic deformation will create a lasting change of the shape of the sample. Plastic deformation is the result of relative motion, or slip, on specific crystallographic planes resulting from shear stress along these planes. The slip plane is normally the plane with the highest density of

atoms. A simple explanation for this is that the separation between those planes is the greatest, and therefore slip between them is the easiest, since the resistance to slip as a result of interatomic forces decreases rapidly with interatomic distance. Within each slip plane there are in turn preferred slip directions, which again are the atomic rows with the greatest density, for the same reason as for the slip planes. A slip plane and a slip direction in the plane constitute a slip system. In face-centred cubic crystals primary slip occurs in one of the four {111} planes where the slip can go in three different <110> directions in each plane, resulting in a total of twelve {111}<110> slip systems.
The slip plane and the slip direction are illustrated in Fig.2.2.1 for a cylindrical single crystal deformed by tension. The tension is performed by applying a force F along the axis of the cylindrical crystal. The tensile stress parallel to F is $\sigma=F/A$ where A is the cross-sectional area.

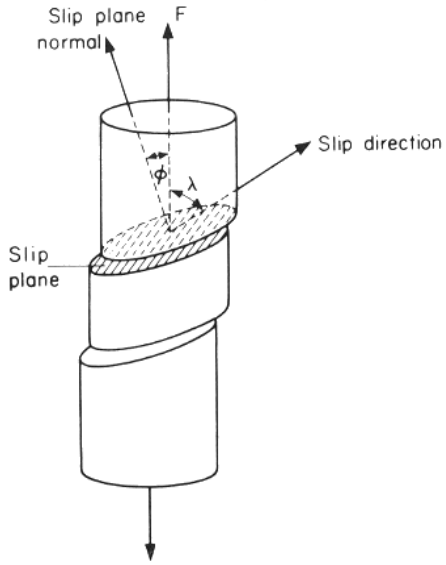


*Fig. 2.2.1. Illustration of the geometry of slip in a single crystal deformed by tension. From (Hull & Bacon, 1984).*

The component of the force in the slip direction is $F\cos\lambda$, where $\lambda$ is the angle between F and the slip direction. The slip surface that this force acts over has an area of $A/\cos\phi$, where $\phi$ is the angle between F and the normal to the slip plane. The resolved shear stress $\tau$ on the slip plane in the direction of the slip will then be

$$\tau = \frac{F}{A}\cos\phi\cos\lambda \qquad (2.2.1)$$

The relation between the tensile stress and the shear stress is called the Schmid law and is normally expressed as $m\sigma = \tau$ where $m = \cos\phi \cdot \cos\lambda$ is the Schmid factor which expresses the geometrical difference between the different slip systems through the angles $\phi$ and $\lambda$. The slip system that will be activated first in a tensile test of a single crystal is according to the Schmid law the slip system with the highest resolved shear stress. The smallest possible tensile force where slip starts to take place corresponds to the so-called critical resolved shear stress $\tau_c$ for slip.
When slip occurs, it results in a lattice rotation of the crystal lattice with respect to the external axes of the sample. This lattice rotation is illustrated in Fig.2.2.2 for slip in a tensile deformed crystal. Slip causes a change of the crystal shape. External constraints on the crystal imposed by the testing machine causes a rotation of the crystal lattice to keep the tensile direction constant. In order to pre-

dict the texture change caused by an increment of macroscopic strain this lattice rotation has to be calculated and several different calculation methods have been proposed.

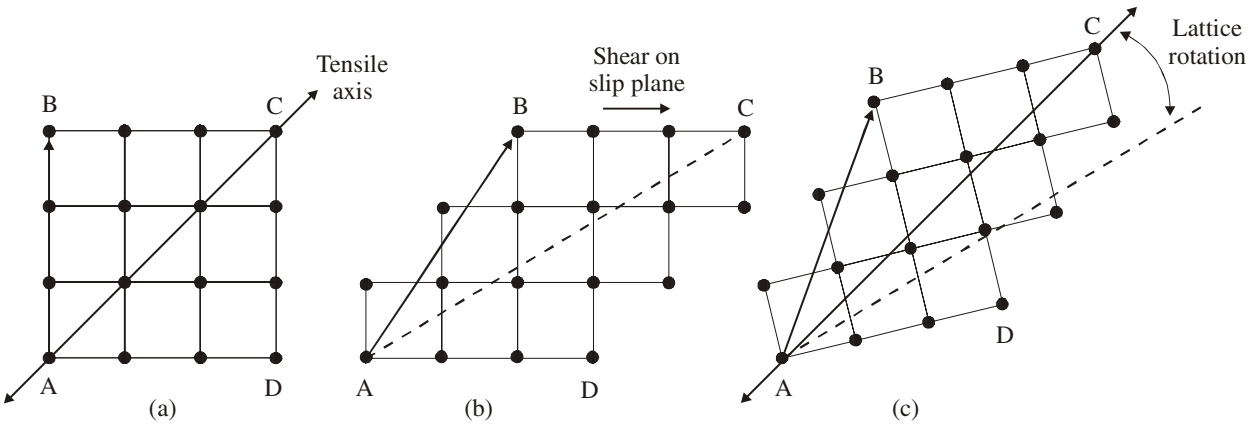


*Fig. 2.2.2. (a) a crystal lattice before a tensile test. (b) Shear on the slip plane does not cause a lattice rotation but other vectors like AB will be rotated. (c) The slip does however make the tensile axis rotate, and in order to bring it back to its original inclination the lattice has to be rotated.*

In the Sachs theory (Sachs, 1928) the Schmid law is used on a polycrystal, by assuming that only one slip system is active in each grain. In this model each grain is supposed to undergo a simple shear. Each grain is considered as a single crystal and the sample as a whole is assumed to behave as the average of all the grains. The shear plane and shear direction depend on the orientation of the slip plane and the slip direction in each grain. Since neighbouring grains usually have different crystallographic orientations these shear directions will be different in neighbouring grains. This means that the resulting macroscopic strains of neighbouring grains will not be equal and this will only be possible if holes are formed between the grains.

Experimentally we know that more than one slip system must be activated to account for plastic deformation in polycrystals but the number of simultaneously activated slip systems is difficult to determine experimentally. In the beginning of plastic deformation it is likely that single slip starts to occur in a few grains (Mecking, 1981). As the deformation goes on single slip will start in other grains and increasing misfits at the grain boundaries will be created. The misfits are first accommodated by elastic strains that will create reaction stresses, which in turn will activate additional slip systems. This process will already at low strains create a state of poly-slip in all the grains.

Von Mises showed in 1928 that five independent slip systems are needed to account for an arbitrary deformation of a single crystal under the assumption that the volume is constant. G.I. Taylor (Taylor, 1938) based his theory on von Mises arguments and solved the problem with grain interactions by assuming a homogeneous strain field. He assumed that each grain undergoes the same strain, which must then be equal to the macroscopic strain.

In the case of fcc materials with (111)<110> slip there are 12 slip systems, and the five activated slip systems in each grain are those that minimise the virtual work per unit volume of the slip systems. The work that is carried out by the five slip systems in each grain must be equal to the work carried out by the macroscopic stress $\sigma$ and strain increment $d\varepsilon$ under the assumption of a homogeneous strain field. If the critical resolved shear stress for slip is $\tau_i$ and the strain increment is $d\gamma_i$ for the $i^{th}$ slip system then we get the relation

$$\sigma d\varepsilon = \sum_{i=1}^{n} \tau_i d\gamma_i \qquad (2.2.2)$$

where n is the number of slip systems. Taylor also assumed that the critical resolved shear stress for slip is the same for all slip systems ($\tau_i = \tau_0$) and the relation then reduces to

$$\frac{\sigma}{\tau_0} = \frac{\sum_{i=1}^{n} d\gamma_i}{d\varepsilon} \qquad (2.2.3)$$

Many other texture models have been proposed for polycrystals. Among the most widely accepted models are the following: 1. The model of relaxed constraints (Kocks & Canova, 1981) that is designed for pancake shaped grains, 2. The modified Sachs model (Leffers & Bilde-Sørensen, 1990) that introduces stochastic stresses to simulate grain-to-grain interactions, 3. The self consistent models (Kröner, 1961) where the elastic constants of the grains are used to describe the grain-to-grain interactions, and 4. The finite element models (see for example Dawson *et al.*, 1994) where grain-to-grain interactions are calculated directly and not through a continuum matrix as in the other models.
A classical single slip texture model has been used to simulate the lattice rotations in a single crystalline fcc material deformed in tension and in compression (Fig.2.2.3). The model calculations do not predict exactly the opposite rotations for tension and compression because different constraints have to be used in the model due to the geometry of the two different deformation methods. In tension one direction is fixed i.e. the tensile axis (see Fig.2.2.2), but in compression a plane is fixed by the compression plates. As a result of this difference the [211] orientation turn out only to be a stable orientation for tension. For an fcc single crystal with the tensile axis in the primary stereographic triangle, the tensile axis will rotate on a great circle toward the primary slip direction [101] until it reaches the [100]-[111] boundary of the triangle (for a discussion of stereographic projections see App.B).

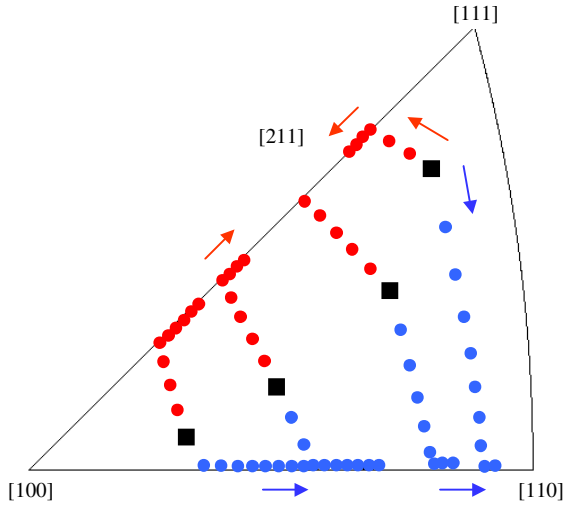


*Fig. 2.2.3. Model predictions of the texture evolution in fcc single crystals deformed in tension (red dots) and in compression (blue dots). The black squares are the starting orientations. (The model predictions were kindly provided by Grethe Winther).*

The primary and conjugate systems on this boundary are equally favoured. If the [110](1-11) conjugate system is the only activated slip system it would

cause a rotation of the tensile axis back into the primary triangle toward the [110] conjugate slip direction. The net result is simultaneous slip on both slip systems, which causes a slow rotation along the [100]-[111] edge toward the [211] pole. At the [211] pole the rotations caused by the primary and conjugated slip systems compensate each other. In compression the orientations rotate toward the [100]-[110] edge where double slip will occur and cause a slow rotation toward the stable [110] pole.

## 2.3 Deformation microstructures

During plastic deformation of metals, dislocations are created in the grains. Even at fairly low temperature the dislocation can move around and interact with each other in order to minimise the strain energy. As a consequence the dislocations will not be randomly distributed in the sample but instead a microstructure of dislocation boundaries is created. The deformation microstructures in metals depend on many parameters, like the temperature, the strain, the strain rate, the deformation type, the grain size and the orientation of the grain and of the neighbouring grains. Here I will limit the description to the most common features observed in tensile tests because it is a uniaxial deformation and therefore comparable with the compression experiments carried out in this thesis.
For relative pure metals at very low strains a microstructure of tangled dislocations is created. At slightly higher strains the dislocations accumulate in boundaries, which separate regions that have relative low density of dislocations. These regions are called cells (Swann, 1963) and the misorientations between the cells are generally less than 5°. The cell boundaries are probably formed by mutual trapping of glide dislocations and are for that reason also called incidental dislocation boundaries (IDBs) (Kuhlmann-Wilsdorf & Hansen, 1991). In the case of tensile deformation three morphologically different types of microstructure have been observed (Huang & Hansen, 1997 and Hansen & Huang, 1998) at medium to high strain.
As shown in Fig.2.3.1 the type 1 microstructure consists of very long and nearly planar dislocation boundaries and because of the high dislocation density in these boundaries they are called dense dislocation walls (DDW). The DDWs may split into two walls and are in that case called a first generation microband (MB1). The cells inside the long extended DDWs are divided in cell blocks by cell block boundaries, which also are DDWs. A widely accepted theory (Bay *et al.*, 1992) is that each cell block deforms by four or less active slip systems. However a group of cell blocks will collectively fulfil the von Mises criterion of five independent slip systems. This means that the strain in each cell block may be different from the macroscopic strain, and the strain differences between the cell blocks will then lead to the formation of cell block boundaries, which therefore have been termed geometrically necessary boundaries (GNBs) (Kuhlmann-Wilsdorf & Hansen, 1991). The long extended DDW are furthermore parallel to within 5° with a slip plane.
The type 2 microstructure is subdivided by ordinary dislocation cell boundaries that have no crystallographic or macroscopic orientation. An equiaxed cell structure is observed with no extended dislocation walls.
The type 3 is very similar to the type 1 microstructure and is subdivided into cell blocks by dense dislocation walls and microbands. The only difference is that the extended dislocation walls are less straight and further from the slip planes than in the type 1 microstructure (Winther *et al.*, 2000a). A brief initial part of the present work was spent on a transmission electron microscopy investigation of uniaxially compressed polycrystalline aluminium and the same types

of microstructures were observed but no effort were put into distinguishing between the different types of microstructures.

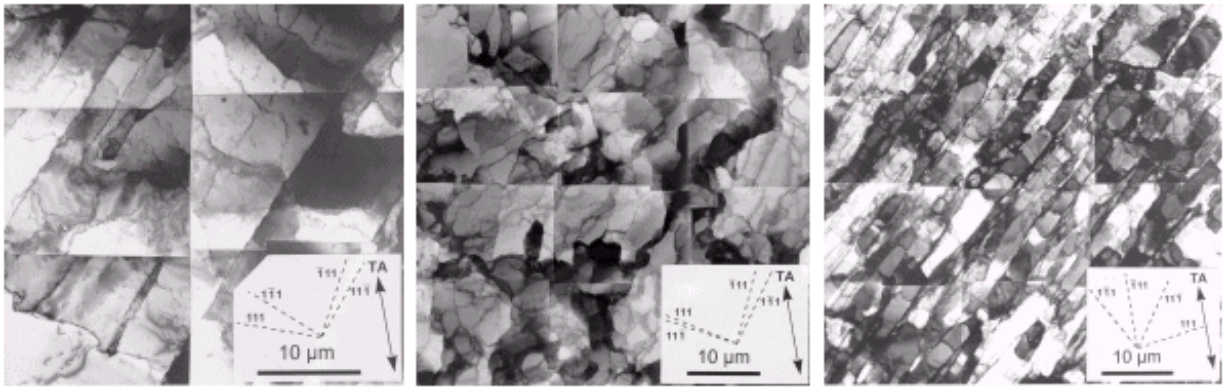


*Fig. 2.3.1. Illustration of the three different microstructures that develop in aluminium deformed in tension. (Left) Type 1 microstructure with long and nearly planar dense dislocation walls that divide the microstructure into cell blocks. (Middle) Type 2 microstructure of ordinary cell boundaries. (Right) Type 3 microstructure which is divided into cell blocks by dense dislocation walls that are less straight and further from the slip planes than in the type 1 microstructure. (from Hansen & Huang, 1998).*

A clear correlation between the type of microstructure and the grain orientation has also been observed in aluminium (Huang & Hansen, 1997) and copper (Huang, 1998) deformed in tension. The orientations of 92 grains in a copper sample deformed in tension to an elongation of 32% are plotted in an inverse pole figure in Fig.2.3.2. The types of microstructure of the individual grains are indicated in the figure by three different symbols. The stereographic triangle is more or less subdivided into three regions in which the grains have the same type of microstructure, showing a clear correlation between the orientation of a grain and its microstructure. Similar microstructures and correlations between crystal orientations have been seen for single crystals (Anongba *et al.*, 1993, Kawasaki, 1974 and Kawasaki, 1994).

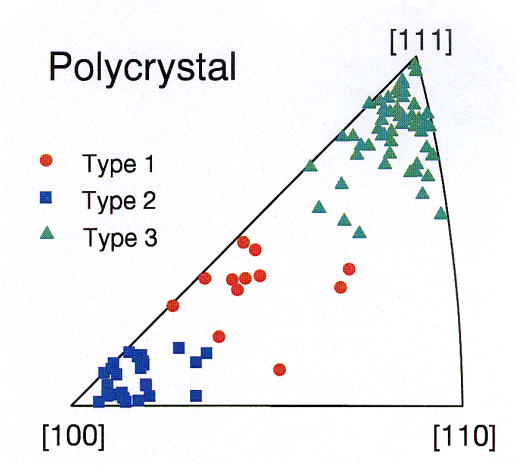


*Fig. 2.3.2. The grains with the three different types of microstructure have been found to have orientations from different regions in the inverse pole figure. (Huang, 1998)*

The samples investigated by Huang and Hansen were all polycrystals deformed by tension, and this is the reason why all the grains they investigated have orientations near the [100]-[111] edge in the inverse pole figure. The orientation of grains or single crystals for that matter will rotate toward the [100]-[111]

grains or single crystals for that matter will rotate toward the [100]-[111] edge when the sample is deformed in tension. This has been shown experimentally by neutron diffraction (Naaman *et al.*, 1987) and by various texture models.

## 2.4 EBSP

Subdivision by cell formation is a well-known phenomena in pure metals, but subdivision may also take place on a larger length scale. Subdivision on a grain scale, for example due to grain-to-grain interactions or due to formation of deformation bands. The macroscopic grain break-up and the texture evolution in aluminium deformed by compression have in this work been studied by electron backscattering diffraction (EBSP). In scanning electron microscopy (SEM) information is achieved from a volume close to the sample surface (see Fig.2.4.1). The size of the interaction volume depends upon the sample material and the energy of the primary electrons.

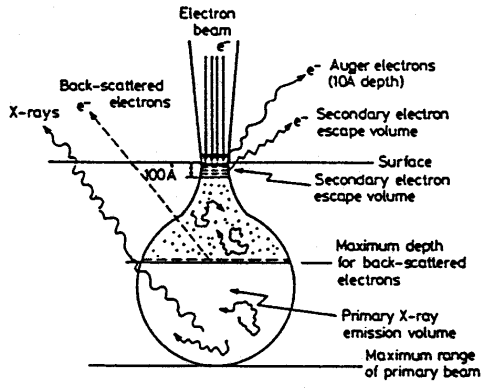


*Fig.2.4.1 Illustration of the interaction volume in a bulk sample when it is illuminated with an electron beam (Kiss, 1988).*

When primary electrons or backscattered electrons are inelasticly scattered in the sample, secondary electrons are produced. The energy of the secondary electrons is typically below 50eV (Schou, 1988). Due to the low energy of the secondary electrons they can only escape from the upper 5-50nm of the sample. Below this limit they will be absorbed. Secondary electrons can however originate from backscattered electrons, which on their way out of the sample have been inelastically scattered within the upper most 5-50nm, and if this happens they will contain information from layers deeper within the sample.
When an electron beam enters a crystalline sample then the electrons will be subject to a diffuse inelastic scattering in all directions. Some of these electrons will have an angle of incidence with the atomic planes that fulfils the Bragg law

$$\lambda = 2d_{hkl} \sin\theta \qquad (2.4.1)$$

where $\theta$ is the Bragg angle, $\lambda$ is the electron wavelength and $d_{hkl}$ is the interplanar spacing for the crystal planes with the Miller indices (hkl). The electrons that fulfil the Bragg law will be elastically scattered and will result in two cones of diffracted electrons as illustrated on Fig.2.4.2. The two diffraction cones are positioned symmetrically around the diffracting crystal planes and separated by twice the Bragg angle. The two cones will be recorded on a two-dimensional detector as hyperbolas. However, the small Bragg angle (~0.5°) and the large opening angles (90°-$\theta$) of the cones will make the hyperbolas appear as two almost straight lines on the detector. These lines are the backscattered Kikuchi lines. Each pair of the Kikuchi lines corresponds to the diffraction from a particular crystal plane in the sample. A detailed description of the formation of the

band structure in the EBSP has been given by Joy *et al.* (1982). The intersection of the diffracting plane and the detector will be at the centre between the two Kikuchi lines. This means that the crystal orientation can be determined from the positions of the Kikuchi lines. A typical electron backscattering pattern (EBSP) is shown in Fig.2.4.3. At Risø Nat. Lab. an automatic programme has been developed that can determine the crystal orientation from the backscattered Kikuchi pattern (Krieger Lassen, 1994).

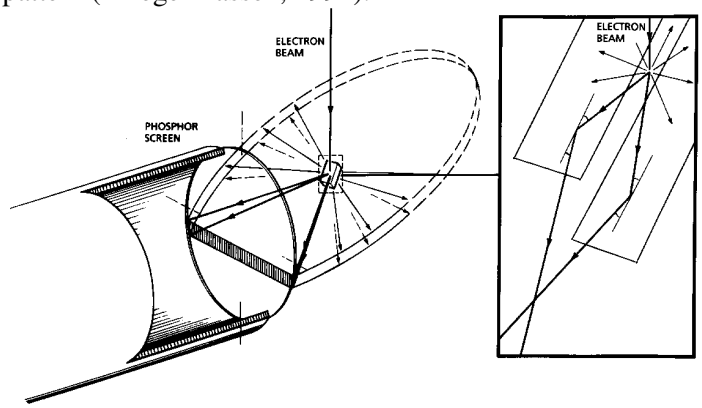


*Fig. 2.4.2. Schematic illustration showing the formation of one pair of backscattered Kikuchi lines from diffraction of the electron beam with one family of lattice planes (from http://www.oxfordinstruments.com/mag/).*

The backscattered Kikuchi lines are identified by a Hough transformation (Hough, 1962) of the recorded and digitised images. A line can be described by its distance r from the origin and the rotation $\delta$ of its normal vector as illustrated in Fig.2.4.3. The so-called normal parameterisation is $r = x\cos\delta+y\sin\delta$ and by utilising this the Kikuchi lines can be transformed into spots in the $(\delta,r)$ space. After image filtering the position of the spots can be determined by standard peak finding techniques. The positions of the spots correspond to the diffracting planes in the sample, and the crystal orientation can be identified when a sufficient number of planes have been determined (Krieger Lassen *et al.*, 1992).

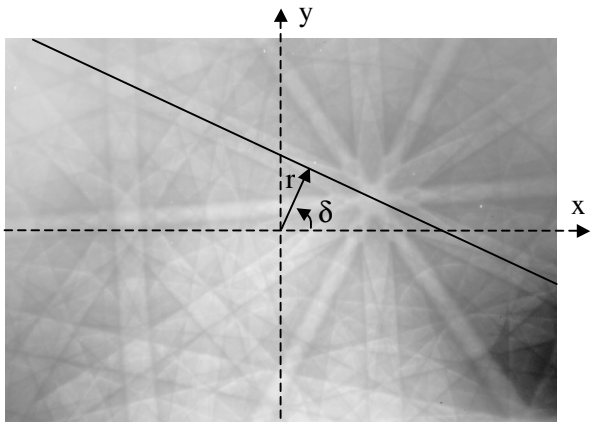


*Fig. 2.4.3. A typical electron backscattering pattern (EBSP). Each of the backscattered Kikuchi lines can be represented by the two parameters r and $\delta$ (according to the normal parameterisation $r = x\cos\delta+y\sin\delta$) where r is the shortest distance from the line to the origin of the co-ordinate system and $\delta$ is the rotation of its normal vector.*

## 2.5 Mean orientation and spread

The EBSP technique produces a set of orientation measurements in the form of Euler angles (see App. **A** for the definition of Euler angles). For a statistical treatment of this ensemble of points one has to be aware that the mean orientation can not be calculated as the simple arithmetic mean of the Euler angles. Instead the mean orientation should be determined as a maximum-likelihood estimate (Krieger Lassen & Juul Jensen, 1994). This method finds the mean orientation matrix **<g>**, which maximises

$$\sum_{i=1}^{N} tr(\mathbf{g}_i^T \cdot <\mathbf{g}>) \tag{2.5.1}$$

where $\mathbf{g}_i$ is the orientation matrix of the $i^{th}$ element in the set of orientations and N is the number of orientations in the set. The EBSP data are expressed in Euler angles but for the calculations of the mean orientation, it is convenient to use unit quaternions (Humbert *et al.*, 1996 and Morawiec & Pospiech, 1989). A quaternion **Q** is related to the Euler angles as used by Bunge (1982) through the following relation

$$\begin{pmatrix} Q_1 \\ Q_2 \\ Q_3 \\ Q_4 \end{pmatrix} = \begin{pmatrix} \cos\left(\frac{\phi}{2}\right)\cos\left(\frac{\varphi_1+\varphi_2}{2}\right) \\ \sin\left(\frac{\phi}{2}\right)\cos\left(\frac{\varphi_1-\varphi_2}{2}\right) \\ \sin\left(\frac{\phi}{2}\right)\sin\left(\frac{\varphi_1-\varphi_2}{2}\right) \\ \cos\left(\frac{\phi}{2}\right)\sin\left(\frac{\varphi_1+\varphi_2}{2}\right) \end{pmatrix} \tag{2.5.2}$$

The mean orientation can then be determined by calculating the eigenvectors of the matrix **M** given by

$$\mathbf{M} = \sum_{i=1}^{N} \mathbf{Q}_i \cdot \mathbf{Q}_i^T \tag{2.5.3}$$

The eigenvector with the largest eigenvalue corresponds to the mean orientation **<g>** (Morawiec, 1998). When the mean orientation has been determined the spread S of the data points around this mean can be calculated as the average misorientation between the mean orientation and all data points according to

$$S = \frac{1}{N}\sum_{i=1}^{N} \Delta\theta_i \tag{2.5.4}$$

where N is the number of data points and $\Delta\theta_i$ is the misorientation between the $i^{th}$ point and the mean orientation. Due to the crystal symmetry a given orientation of a cubic crystal can be represented by 24 symmetrical equivalent representation. In order to determine the mean orientation and the orientation spread it is necessary that each orientation is expressed by that particular symmetrical equivalent representation that makes all the data points have the smallest misorientation to each other. When the EBSP data are acquired at the microscope, each data point is treated individually and the Euler angles are determined from the set of recognised backscattered Kikuchi lines. No attempt is made to represent one particular orientation as one particular Euler representation. In a computer program all the symmetrical Euler representations of all the data points can be calculated and the set where all the points have the smallest misorientation to each other can be determined. The 24 symmetrical representations of the same data point do however create a problem if the sample has been deformed and a large orientation spread has been introduced in the data set. For a large orientation spread it will be impossible to determine, if a large misorien-

tation between two data points is due to the orientation spread caused by the deformation or due to a wrong choice of symmetrical equivalent Euler representations.
This problem is sketched in Fig.2.5.1. As a simple example we can look at two symmetrical equivalent sets of Euler angles: ($\varphi_1$ $\phi$ $\varphi_2$–45°) and ($\varphi_1$ $\phi$ $\varphi_2$+45°) that each have a misorientation of 45° to the mean orientation ($\varphi_1$ $\phi$ $\varphi_2$). Let us assume that we have a perfect single crystal and that the sample is deformed in such a way that the measured set of Euler angles only spreads out in the $\varphi_2$ direction. If the spread becomes larger than 45°, it will be possible to choose another symmetrical Euler representation that has a smaller misorientation to the ($\varphi_1$ $\phi$ $\varphi_2$) orientation, see Fig. 2.5.1. In this example it will not be possible to measure an orientation spread that is larger than 45° because we have to find the symmetrical equivalent representation of each data point that gives the smallest misorientation to all other data points, in order to calculate the mean orientation as described earlier.

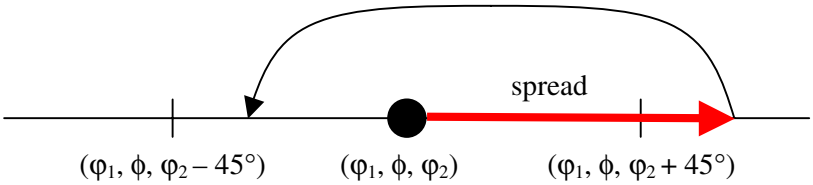


*Fig. 2.5.1. If deformation makes the orientations spread out only in $\varphi_2$ (red arrow) then if the spread is larger than 45° we can choose another symmetrical representation that has a smaller misorientation to the mean orientation ($\varphi_1$ $\phi$ $\varphi_2$).*

This means that there is a limit for how large an orientation spread that can be measured. The limit can be determined by creating a set of random orientations and calculating the misorientations between all the orientations in the set. This has been done for a set of 225 random orientations and the result is plotted in Fig.2.5.2 as a histogram with a bin size of 2°. This distribution of the misorientations is called a Mackenzie distribution (Mackenzie & Thomson, 1957). As an effect of the symmetry the largest possible misorientation between two orientations in a cubic material is seen in the Mackenzie distribution to be 62.8°. When calculating the spread as defined in Eq. (2.5.4) we see that it corresponds to the mean value of the Mackenzie distribution, which is 40.7° (Mackenzie, 1958). It will therefore not be possible to determine a spread in any set of orientations that is larger than this value of 40.7°.

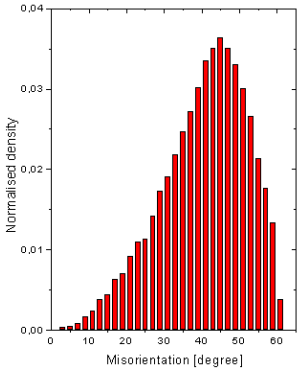


*Fig. 2.5.2. The Mackenzie distribution determined by calculating the misorientation between all orientations in a set of 225 random orientations of a fcc crystal.*

## 2.6 Experimental results

An electron microscopy investigation of both aluminium single crystals and polycrystals deformed in compression was carried out. The single crystals were grown at Ecole National Superieure des Mines de St. Etienne. In the following the compression experiments will be described and the results obtained from the two different types of materials will be discussed. Some of the results are presently being prepared for publication (Winther *et al.*, 2000b).

### 2.6.1 Single crystals in compression

Four different single crystals were selected from their position in the inverse pole figure; one in each corner and one in the middle. The crystallographic orientations of the single crystals were [100], [110], [111] and [235]. The single crystals were cut into small cubes (8×9×10mm) by spark erosion and afterwards uniaxially compressed to five and in some cases six different strain levels with a strain rate of 20μm/sec. The number of samples depended on the amount of material. For the [110] and [111] crystals, the material shortness made it necessary to reuse the strain level ① samples and deform them to strain level ⑤. In a compression experiment some friction will always be present between the ends of the sample and the pressure plates. Compression of the material causes an increase in area, and therefore a tendency to slide outward over the plates, against the shear stress on the interfaces due to the frictional resistance. In order to minimise the friction all samples were wrapped in teflon tape before the compression, to lubricate the interface between the ends of the sample and the pressure plates. The compression resulted in slightly different strains in the different single crystals. The exact strains of all the samples are listed in Table 2.6.1. Each row in the table contains single crystals with different orientations deformed to approximately the same strain. The strains of all samples with similar strains will be referred to as strain Level ① - ⑥, respectively.

| Strain level | [100] (%) | [110] (%) | [111] (%) | [235] (%) |
|---|---|---|---|---|
| Level ① | 0 | 0 | 0 | 0 |
| Level ② | 5.7 | 5.5 | 5.4 | 5.8 |
| Level ③ | 11.1 | 10.7 | 10.7 | 11.5 |
| Level ④ | 16.0 | 15.6 | 15.6 | 16.4 |
| Level ⑤ | 22.0 | 21.7 | 21.4 | 22.0 |
| Level ⑥ | 40.6 | --- | --- | 41.0 |

*Tabel 2.6.1. The uniaxial compression of the four single crystals expressed in percentage decrease of the sample height. The strains of the single crystals in each row are comparable and the rows have for that reason been given the names strain Level ① - ⑥.*

After the uniaxial compression the samples were prepared for EBSP. To avoid introducing an inclined surface by polishing, the samples were put in an acrylic mounting (Technovit 4071) to make the samples fit into a special holder made for the MecaPol-P300 (Presi) polishing machine. In this way it was possible to maintain plane parallel top and bottom of the sample through the polishing. The samples were ground and polished on the compression plane and the few remaining scratches were removed in a Vibromet-2 (Branson) by vibrating the samples in a solution from Buehler (Mastermet 2 no. 40.6380.064) on a very

smooth piece of cloth for one hour. During the polishing 2mm of material were removed from the surfaces of all the samples. As the final preparation for EBSP, the samples were electro-polished by using a Struers ElectroPol-5 with a voltage of 33V and a flow rate of 13/sec in 45sec. The solution used for the electro-polishing consisted of 30ml $HClO_4$, 170ml $H_2O$, 100ml Butilsellosolve and 700ml Ethanol.

An area of $1000\times750\mu m^2$ were measured on each of the samples by the EBSP technique with a step size of 10μm. All samples were aligned in the microscope with one of the sample edges parallel to the microscope axis. The scan on each sample was performed in the centre of the compression plan. The software programme Channel4 was used to visualise the EBSP data. Grain boundaries with misorientations of 1° and 2° are plotted as thin and thick black lines in the orientation images and misorientations of 10° and 15° are plotted as thin and thick white lines. Each pixel in an orientation image corresponds to one measurement of the crystal orientation and the pixel is coloured according to the measured orientation. The standard colour palette is not especially sensitive to small variations in the orientations. In order to visualise groups of data points that in orientation are separated from the neighbouring data points an alternative plotting programme was constructed in corporation with Jean-Christoph Glez at Ecole National Superieure des Mines de St. Etienne. This program takes a possible orientation gradient across the EBSP images into account. By setting a misorientation threshold the program can separate the groups of points that have a misorientation to the surrounding points of more than the threshold value. All groups are plotted in random colours. This alternative plotting scheme helps to visualise abrupt orientation changes from the background when the background contains an orientation gradient. If the threshold is set at 15° then this program can find the grain boundaries in a polycrystal and visualise the grain areas in random colours.

Fig.2.6.1 shows the acquired orientation images of the [100] single crystals at the different strain levels. The images labelled 1a-6a are plotted in the standard way in Channel4. Image (1a) is the undeformed crystal and very few misorientations of more than 1° are observed. The presence of even a few misorientations in the undeformed crystal indicate that the sample is not a perfect single crystal. This could be due to the manufactoring process of the single crystal, the spark erosion technique used to produce the individual samples, or the polishing of the samples for EBSP. As the strain goes up the number of small misorientations increase, and the misorientations are homogeneously distributed in the images at low strains (see 2a and 3a). At strain levels ④ and ⑤ (4a and 5a) a large-scaled structure appears and at the highest strain level, boundaries with a misorientation between 10° and 15° are formed, but no large-scaled structure is observed. Images 1b-6b in Fig.2.6.1 is plotted by the alternative plotting program with a misorientation threshold of 1°. At low strains a small orientation gradient is present in the images (see 1b, 2b and 3b). In 4b the large scaled structure becomes much more visual than in 4a. Looking at the whole series 1b-6b it is obvious that the groups of points that have a misorientation of more than 1° to the surrounding points are getting smaller when the strain is increasing. The groups of points that are visualised by this alternative plotting technique can not be interpreted as cells for several reasons. Firstly, the step size between the points are too large (10μm) to measure cells and secondly the angular resolution of the EBSP technique is ~1° whereas the misorientation between cells typically are 0.1°-0.5° (Huang & Juul Jensen, 2000). The decreasing size of the groups for increasing strain can only be interpreted as an increase in the fluctuations of the orientations when the strain is increasing.

Fig.2.6.2 are the same type of orientation images of the [110] single crystals. The numbers of low angle boundaries are increasing rapidly with increasing strain homogeneously over the full area of the images. At strain level ③ the whole sample area is covered with low angle boundaries. In order to observe large-scaled features, the images 1b-5b have been plotted with a misorientation threshold of 2° and only at strain level ④ and ⑤ some smaller groups of points start to appear. In the Channel4 images at the same strain levels (4a and 5a) small groups of dark green and blue points are seen to be mixed in between each other. This indicates that the crystal breaks up in small regions that, more or less, have one of two different orientations.

For the [111] single crystals in Fig.2.6.3 the number of low angle boundaries is increasing even faster with increasing strain. Already at strain level ② the sample area is completely covered with low angle boundaries. At strain level ③ misorientations with angles between 10° and 15° start to appear and at level ④ some misorientations are larger than 15°. At strain level ⑤ a horizontal band is clearly visual. High angle boundaries exist more frequently outside the band than inside. In (5b) a sub-division in medium sized groups is seen outside the band. The band it-self is almost one single group with a few very small sized groups evenly distributed in the band.

The main feature in the orientation images of the [235] single crystals in Fig.2.6.4 is a developing band structure for increasing strain. At strain level ③ the low angle misorientations are already clustered in long lines and a band structure is developed at strain level ④. At level ⑤ high angle boundaries are formed at the edges of the bands and at strain level ⑥ high angle boundaries are observed inside the band. In the images 3a, 4a and 5a the angle of the band structure is approximately 60° relative to the x-axes of the images but at strain level ⑥ the band is horizontal. This could be due to a misalignment of the sample with the highest strain. The high deformation caused the surface of the sample to change shape to a parallelogram with bulky edges and this made it difficult to align the sample in the microscope.

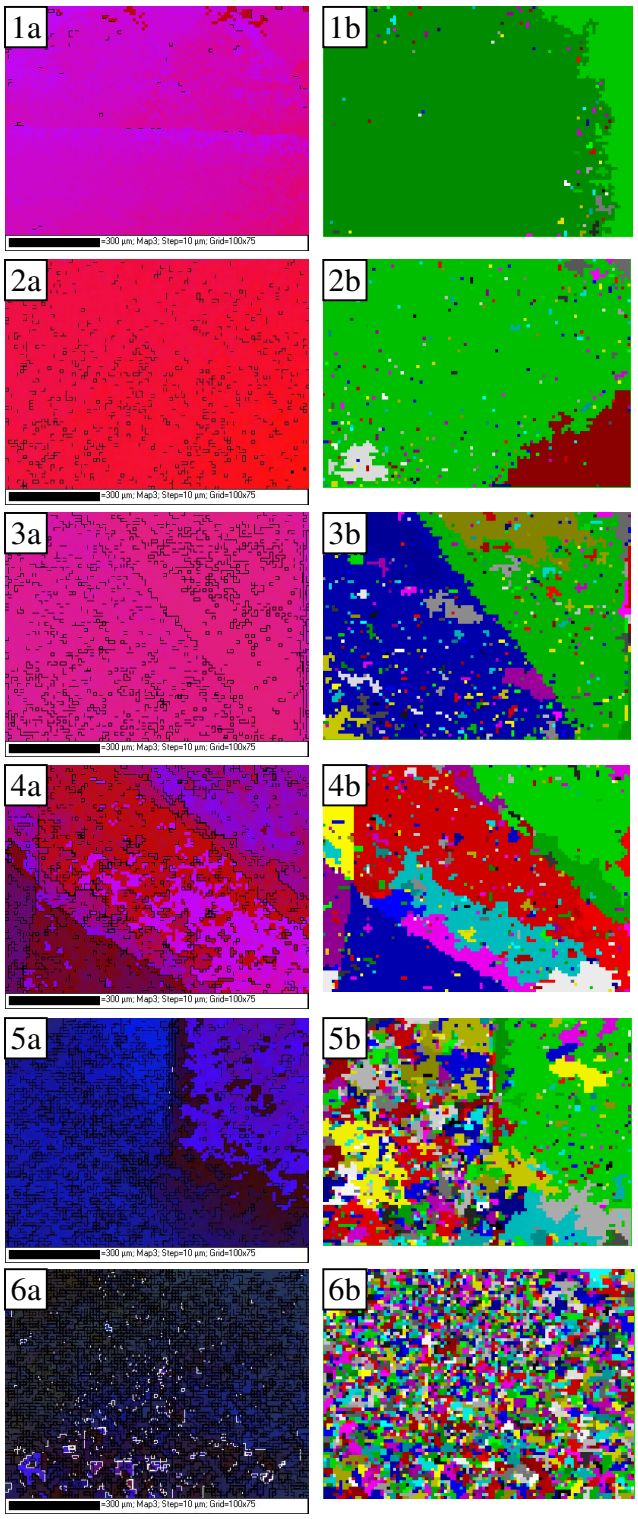


*Fig. 2.6.1. Orientation images from the compression plane of [100] single crystals deformed to six different strains: (1) Level ①, (2) Level ②, (3) Level ③, (4) Level ④, (5) Level ⑤ and (6) Level ⑥. Each image represents an area of 1000×750μm$^2$ recorded with a step size 10 μm. The images in the left column (1a-6a) are the raw orientation images where thin and thick black lines correspond to 1° and 2° misorientations and thin and thick white lines correspond to 10° and 15° misorientations, respectively. The right column (1b-6b) is the same EBSP data plotted by the alternative technique with a threshold value of 1°.*

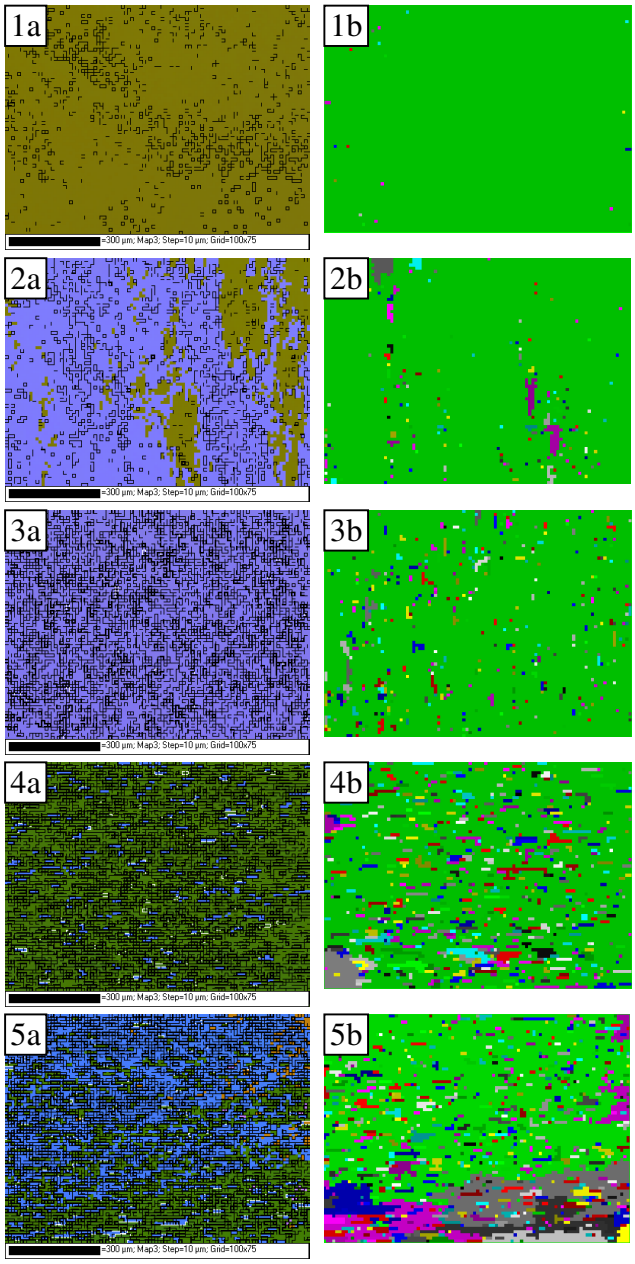


*Fig. 2.6.2. Orientation images from the compression plane of [110] single crystals deformed to five different strains: (1) Level ①, (2) Level ②, (3) Level ③, (4) Level ④ and (5) Level ⑤. Each image represents an area of 1000×750μm$^2$ recorded with a step size 10 μm. The images in the left column (1a-5a) are the raw orientation images where thin and thick black lines correspond to 1° and 2° misorientations and thin and thick white lines correspond to 10° and 15° misorientations, respectively. The right column (1b-5b) is the same EBSP data plotted by the alternative technique with a threshold value of 2°.*

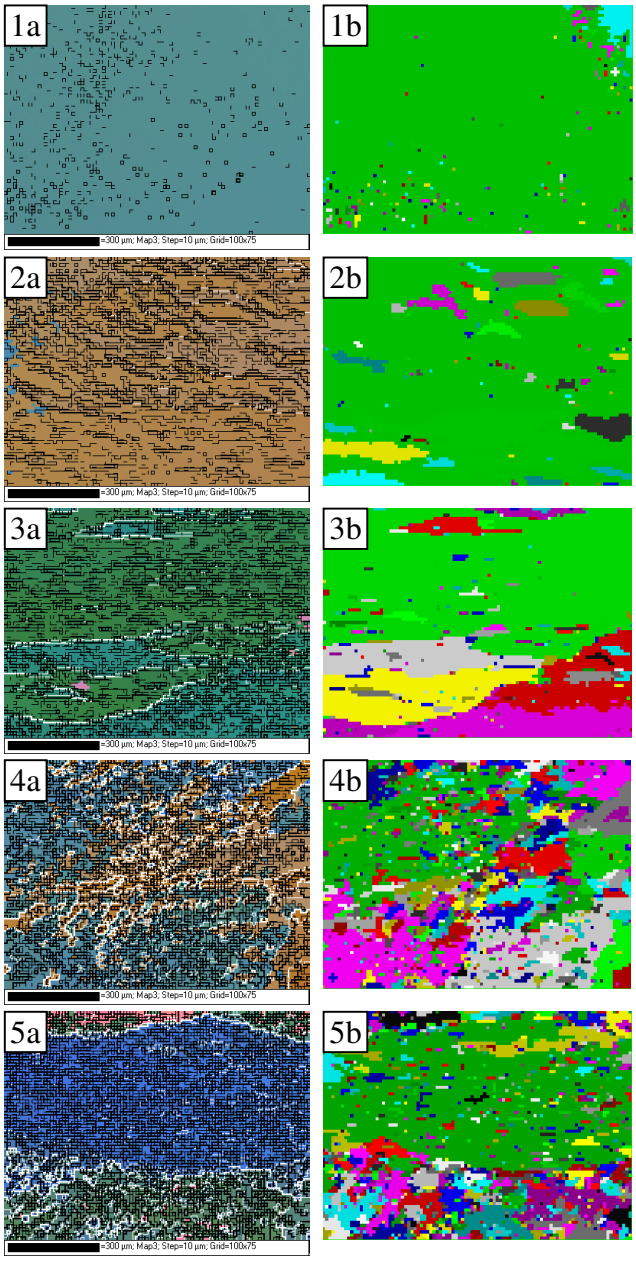


*Fig. 2.6.3. Orientation images from the compression plane of [111] single crystals deformed to five different strains: (1) Level ①, (2) Level ②, (3) Level ③, (4) Level ④ and (5) Level ⑤. Each image represents an area of 1000×750μm$^2$ recorded with a step size 10 μm. The images in the left column (1a-5a) are the raw orientation images where thin and thick black lines correspond to 1° and 2° misorientations and thin and thick white lines correspond to 10° and 15° misorientations, respectively. The right column (1b-5b) is the same EBSP data plotted by the alternative technique with a threshold value of 2°.*

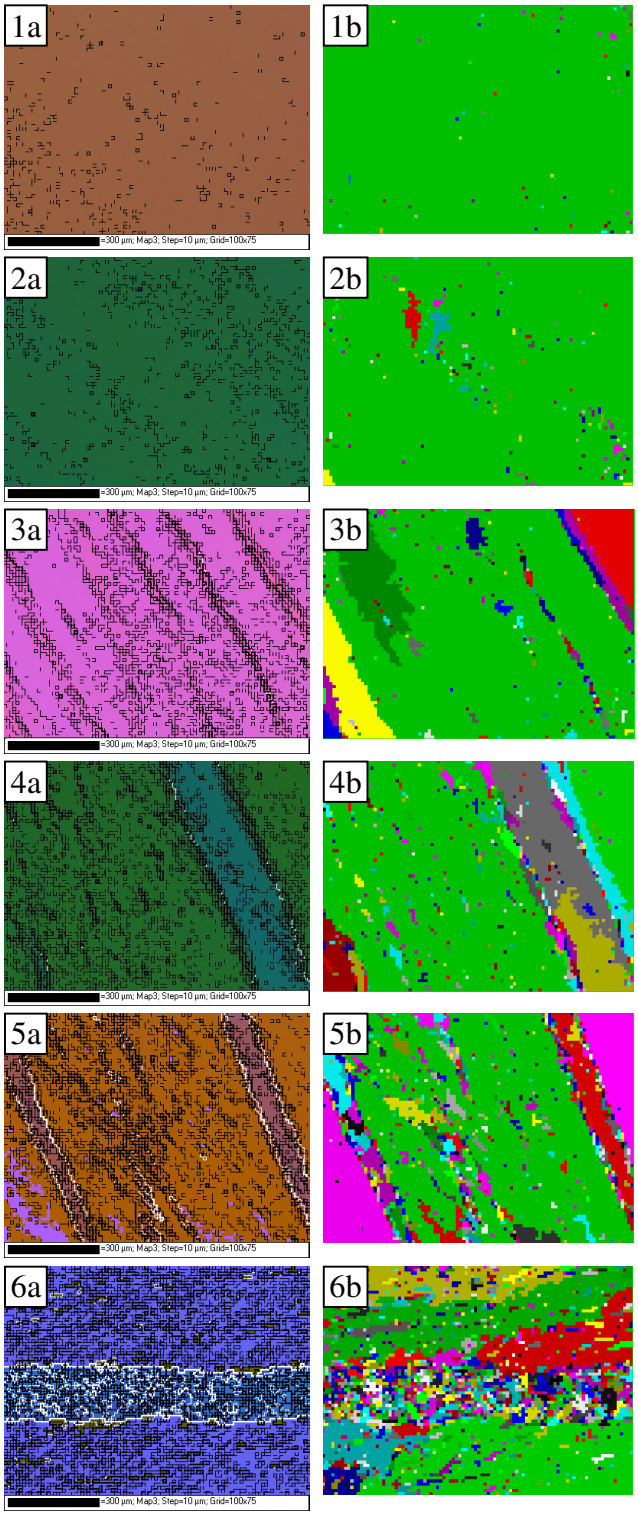


*Fig. 2.6.4. Orientation images from the compression plane of [235] single crystals deformed to six different strains: (1) Level ①, (2) Level ②, (3) Level ③, (4) Level ④, (5) Level ⑤ and (6) Level ⑥. Each image represents an area of 1000×750μm$^2$ recorded with a step size 10 μm. The images in the left column (1a-6a) are the raw orientation images where thin and thick black lines correspond to 1° and 2° misorientations and thin and thick white lines correspond to 10° and 15° misorientations, respectively. The right column (1b-6b) is the same EBSP data plotted by the alternative technique with a threshold value of 2°.*

The measured orientations, represented by colours in the orientation images, have also been plotted as pole figures and inverse pole figures of the compression plane in Fig.2.6.5 and Fig.2.6.6, respectively.
The mean orientations of the [100] and [110] single crystals are seen from the pole figures (Fig.2.6.5) to be stable with increasing strain. The size of the spots in the pole figures is increasing with increasing strain, indicating that the orientations of the measured points more or less spread out in all directions (a spherical spread). The [111] and [235] have on the other hand a pronounced spread in only one direction. The band structure in the [235] single crystal at strain level ⑥ is seen in the pole figure as two clearly separated spots.
The inverse pole figures in Fig.2.6.6 consist of two stereographic triangles (see App. **B**). All the orientations at the different strain levels measured on the [110] single crystal seem to jump between the primary and the conjugated triangles. Indicating that two different sets of slip systems are equally favoured. At strain level ④ and ⑤ the orientations spread out in both triangles. The data points are coloured dark green and blue in the two stereographic triangles, respectively. The same colour scheme is used in the orientation images and the observed macroscopic sub-division, see Fig.2.6.2 (4a-5a), are clearly related to the predominant activation of the two different sets of slip systems. The orientation spread in both stereographic triangles is caused by a continuous variation in the activity of these slip system sets.
The orientations measured on the [100] single crystal (see Fig.2.6.6) are also observed to spread out in both the primary and the conjugated triangles. The data points in the two systems are coloured dark blue and blue and correspond to the areas in the orientation images that constitute the macroscopic sub-division, see Fig.2.6.1 (5a-6a).
The [111] single crystal starts out at strain level ① slightly off the [111] pole in the inverse pole figure (Fig.2.6.6). The main feature is a large one-dimensional spread toward the [110] pole. Again the orientations jump between the primary and the conjugated triangles when the strain is increased from level ① to level ② indicating two different sets of slip systems are equally favoured. At strain levels ③ and ④ the orientations spread out on both triangles and at strain level ⑤ the orientations divide into two separated spots in the inverse pole figure where the blue spot close to the [110] pole corresponds to the blue band in the middle of Fig.2.6.3(5a).
The [235] single crystal starts out by moving toward the [100]-[110] edge at strain level ② in Fig.2.6.6. At strain level ③ the orientations spreads out further towards the [001]-[110] edge but the spread completely stops in this direction at level ④ where the orientations instead starts to spreads out in the opposite direction toward the [100]-[$11\bar{1}$] edge. The spread toward the [100]-[110] edge continues at strain level ⑤ and at level ⑥ the orientations divide into two separated spots in the inverse pole figure. The spot closest to the [110] pole at strain level ⑥ is the material outside the band in Fig. 2.6.4.(6a) and the other spot that has a larger spread correspond to the data points inside the band.

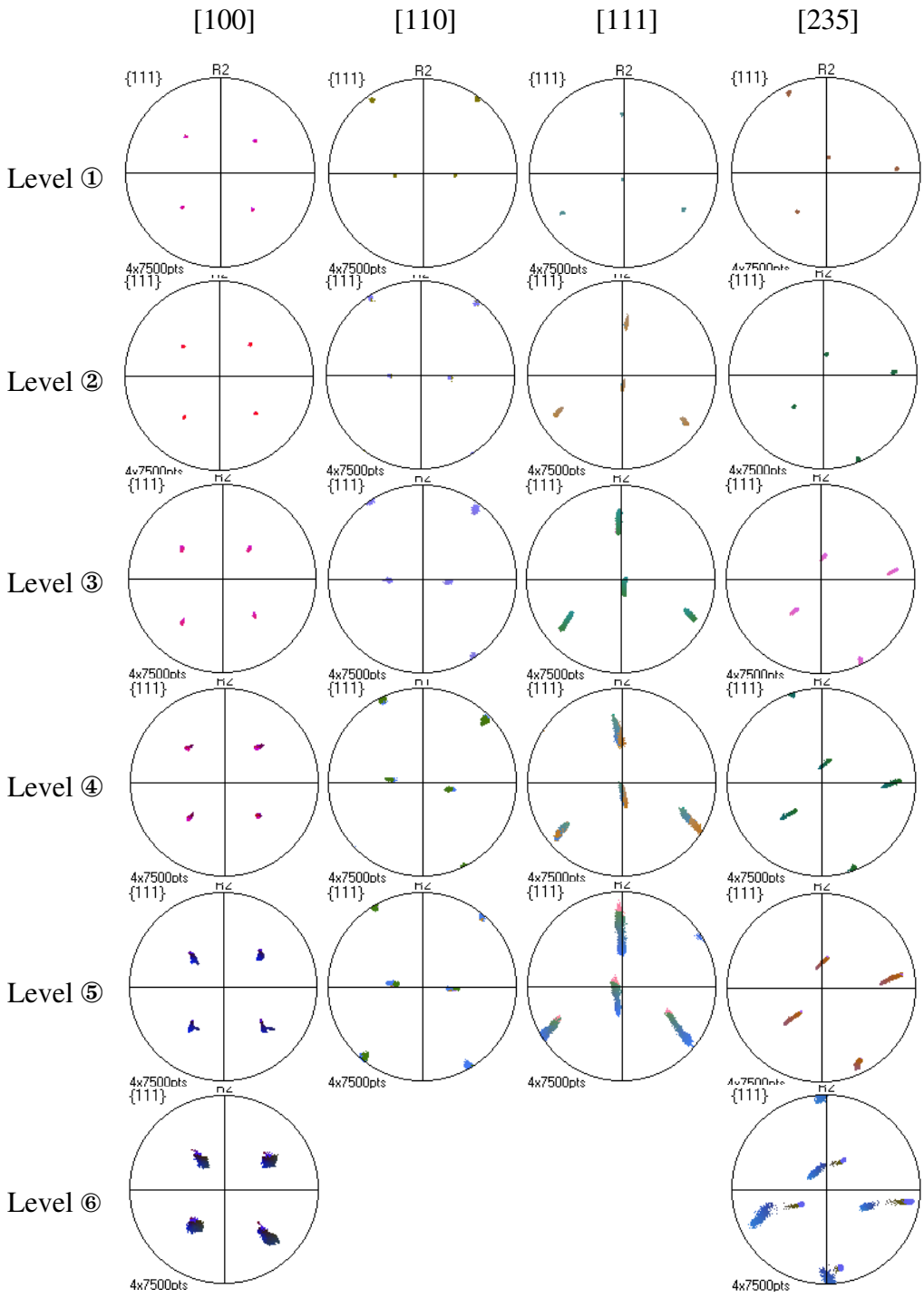


*Fig. 2.6.5. Pole figures of the compression plane of the four different single crystals deformed to different strain levels. Each column is one type of single crystal deformed to five or six different strain levels and each row is the four single crystals deformed to the same strain level.*

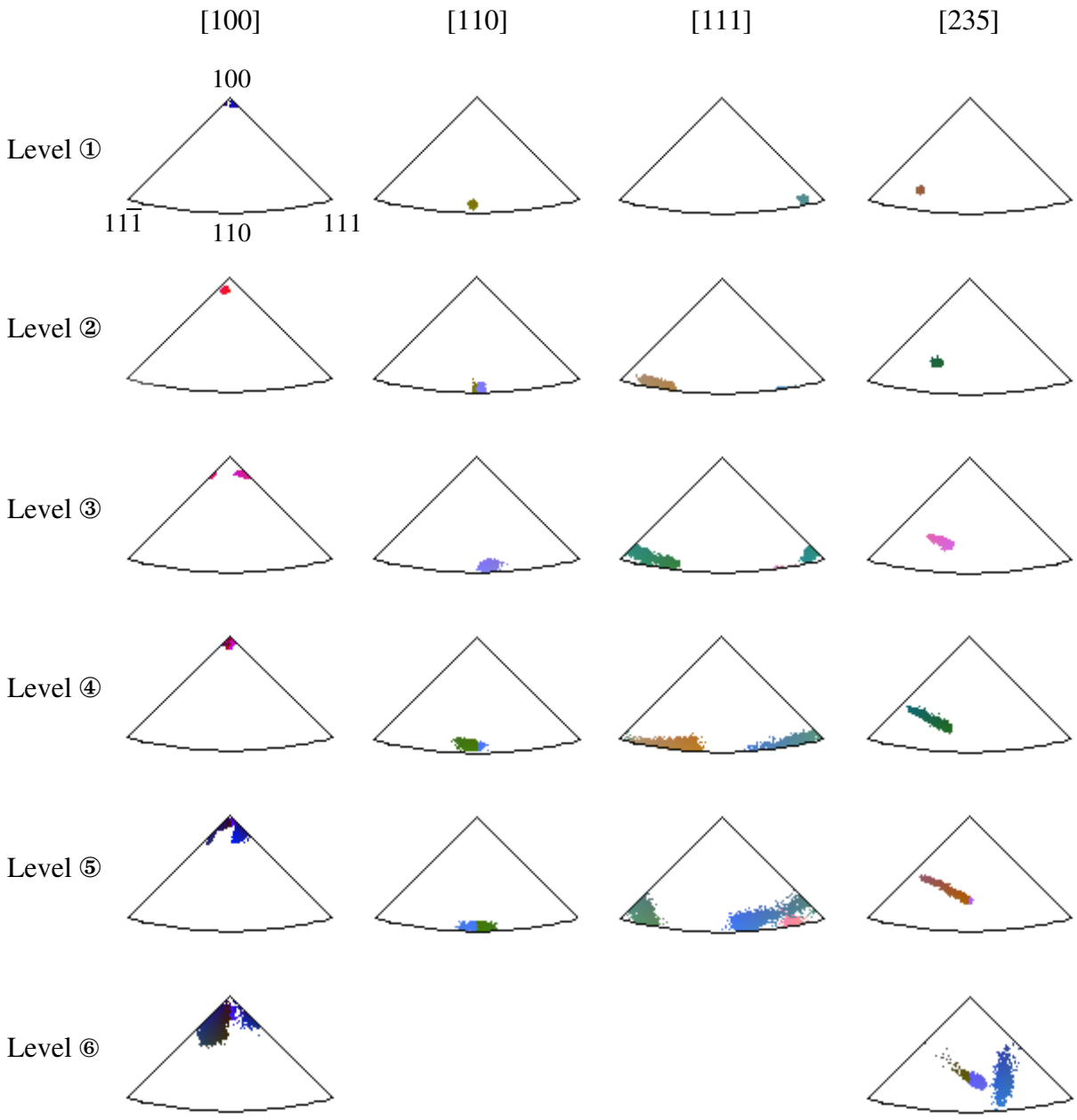


*Fig. 2.6.6. Inverse pole figures of the compression plane of the four different single crystals deformed to different strain levels. Each column is one type of single crystal deformed to five or six different strain levels and each row is the four single crystals deformed to the same strain level.*

The pole figures and the inverse pole figures (Fig. 2.6.5 and Fig. 2.6.6) show that the orientation spread is increasing for increasing strain in all the single crystals. In order to quantify the spread the mean orientations were found and the spreads of the orientations around these mean orientations were calculated as described in section 2.5. The values are listed in Table 2.6.2. and Table 2.6.3. As seen in Fig.2.6.5 the spread of the orientations in the [100] and [110] single crystals are more or less spherical in contrast to the [111] and [235] single crystals where the orientations mainly spread out in only one direction. When calculating the spread as the averaged misorientation of all points to the mean orientation, the large spread in one direction will be averaged with the smaller spread in the two other directions. The result is a smaller spread than expected when looking at Fig.2.6.5 for the [111] and [235] single crystals. The large one-dimensional spreads of the measured orientation in these two single crystals at different strain levels have therefore been estimated from Fig.2.6.5. The estimated values (see Table 2.6.3) give a truer picture of the actual spread.
The EBSP data were acquired from the middle of the surface areas of the samples, and some fluctuations in the calculated orientation spreads would be expected due to the observed large-scale structure. The spreading of the orientations is caused by the sub-division of the single crystals into small volume element where the crystal lattices are rotated differently with respect to each other. The orientation spreads therefore represent the large-scale microstructure.

| **[100]** Strain level | φ1 [degree] | ϕ [degree] | φ2 [degree] | Spread [degree] |
|---|---|---|---|---|
| ① | 70.922 | 2.171 | 68.196 | 0.654 |
| ② | 17.862 | 5.016 | 20.366 | 0.786 |
| ③ | 48.120 | 9.531 | 50.242 | 1.185 |
| ④ | 15.948 | 1.973 | 17.219 | 1.766 |
| ⑤ | 34.897 | 6.985 | 34.181 | 3.856 |
| ⑥ | 56.549 | 14.084 | 60.609 | 4.388 |
| | | | | |
| **[110]** Strain level | φ1 [degree] | ϕ [degree] | φ2 [degree] | Spread [degree] |
| ① | 178.082 | 41.951 | 177.744 | 0.84 |
| ② | 177.952 | 43.533 | 179.536 | 0.84 |
| ③ | 177.214 | 42.604 | 174.300 | 1.25 |
| ④ | 187.435 | 42.042 | 177.204 | 1.48 |
| ⑤ | 185.211 | 43.778 | 180.416 | 1.93 |

*Table 2.6.2. The calculated mean orientations in Euler angles and the spread of the orientations around the mean values for the [100] and [110] single crystals. Both single crystals have a more or less spherical orientation spread.*

| **[111]** Strain level | φ1 [degree] | ϕ [degree] | φ2 [degree] | Spread [degree] | 1D Spread [degree] |
|---|---|---|---|---|---|
| ① | 116.489 | 49.751 | 128.303 | 1.02 | 1 |
| ② | 114.567 | 47.526 | 120.323 | 2.63 | 5 |
| ③ | 120.313 | 51.973 | 119.514 | 5.61 | 18 |
| ④ | 116.117 | 49.218 | 120.964 | 4.39 | 30 |
| ⑤ | 105.652 | 42.554 | 116.286 | 11.48 | 20 |
| | | | | | |
| **[235]** Strain level | φ1 [degree] | ϕ [degree] | φ2 [degree] | Spread [degree] | 1D Spread [degree] |
| ① | 146.031 | 33.709 | 24.300 | 1.03 | 1 |
| ② | 131.820 | 35.799 | 69.141 | 0.87 | 1 |
| ③ | 140.730 | 35.370 | 75.376 | 1.45 | 5 |
| ④ | 128.304 | 36.463 | 67.988 | 4.97 | 10 |
| ⑤ | 122.160 | 32.386 | 96.931 | 3.54 | 15 |
| ⑥ | 132.721 | 31.323 | 93.737 | 12.54 | -- |

*Table 2.6.3. The calculated mean orientations in Euler angles and the spread of the orientations around the mean values for the [111] and [235] single crystals. The large one-dimensional spreads have been estimated from Fig.2.6.6.*

At present no texture models are capable of predicting a microstructure and no model predictions of crystal orientations after a given straining will therefore have any orientation spread. By using a single slip model the final orientation of the four different single crystals has been calculated at the different strain levels. The predicted orientations are superimposed as yellow dots on a standard inverse pole figure of the measured orientations in Fig.2.6.7.
The model predicts that there are eight equally favoured slip systems for the [100] single crystals corresponding to four different lattice rotations. Depending on the slip system the orientation of the [100] single crystal will rotate along the [100]-[111] edge as shown in Fig.2.6.7 or along the [100]-[11$\bar{1}$] edge in the conjugate slip system. If both slip systems are activated then the [100] orientation will evolve along the [100]-[110] edge for increasing strain.

For the [110] single crystal the model predicts four equally favoured slip systems that correspond to two different lattice rotations. The orientation can rotate towards the [111] pole as shown in Fig.2.6.7 or rotated towards the [11$\bar{1}$] pole in the conjugated slip system. If both slip systems are activated then the [110] orientation will be stable for increasing strain. The measured orientations of the [110] single crystal at strain level ⑤ are observed to be stable at the [110] pole and spreading out toward both the [111] and [11$\bar{1}$] poles, see Fig.2.6.6. Thus a good agreement between model predictions and measured texture evolution of the [110] single crystal is observed.

It should be emphesied that the model predictions plotted in Fig.2.6.7 only show one of the possible lattice rotations. The [100] and the [110] orientations are stable if all the slipsystems are included but the model predictions in Fig.2.6.7 illustrate how far the lattice would rotate if only one slipsystem were used.

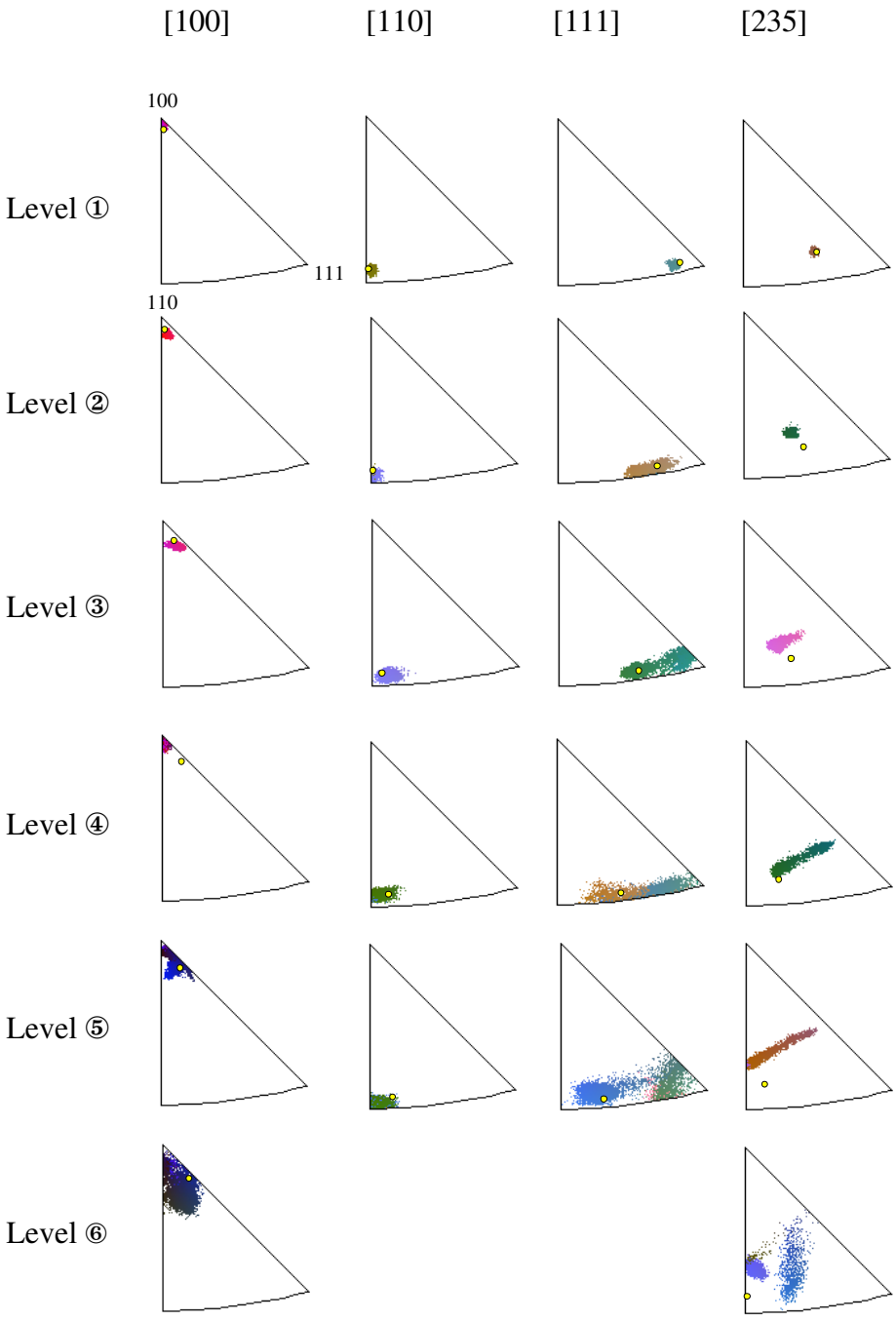


*Fig. 2.6.7. The folded inverse pole figures of the compression plane of the four different single crystals deformed to different strain levels. Each column is one type of single crystal deformed to five or six different strain levels and each row is the four single crystals deformed to the same strain level. A single slip texture model has been used to simulate the texture evolution in the single crystals. The yellow spots correspond to the calculated orientations at the respective strains.(with courtesy to Grethe Winther)*

The measured texture evolution of the [111] single crystal includes a large one-dimensional spread of the orientations. The texture model cannot predict the orientation spread but the rotation towards the [110] pole seems to agree reasonably well with the measured orientations.
The [235] single crystal is the only one that does not agree with the model predictions. The model predicts a continuous rotation toward the [100]-[110] edge. The measured orientations jump toward the [100] pole at strain level ② and continue to stay at this position for higher strains. At strain level ④ the measured orientations even spreads out toward the [100]-[111] edge, which is completely opposite to the predicted rotation. At strain level ⑥ the [235] single crystal breaks-up and a large spread is observed almost parallel to the [100]-[110] edge. This break-up is due to the formation of a band structure in the scanned area (see Fig.2.6.4). The formation of such a microstructure can at present, not be predicted by any texture model.

### 2.6.2 Polycrystals in compression

An electron microscopy investigation of aluminium polycrystals was also carried out at Ecole National Superieure des Mines in St. Etienne. The sample material was commercially pure aluminium (99.4%), the main impurities being Fe (0.33wt%) and Si (0.09wt%). All the samples were machined to cylinders with a diameter of 5mm and a height of 8mm. The samples were afterwards annealed for 24 hours at 500°C and slowly cooled to room temperature over a period of 6 hours, in order to minimise the mosaic spread of the grains. The deformation microstructures in the aluminium polycrystals were characterised at different strain levels by the EBSP technique and the texture evolution was investigated.
The samples were deformed by uniaxial compression with a strain rate of 20μm/sec to five different deformations (0%, 5%, 11%, 16%, 23%). The samples were mechanically polished from one end to a finial height of 2/3 of the height after the deformation and afterwards electro-polished for EBSP. An area of (2.5x1.875mm$^2$) of the compression plan on all the samples was measured by the EBSP technique with a step size of 25μm. The orientations of each point in the EBSP scans are plotted on pole figures and inverse pole figures of the compression plane in Fig.2.6.8. Thin and thick black lines in the orientation images correspond to misorientations of 1° and 2°, and white lines correspond to misorientations larger than 15°.
The EBSP scans were performed in the centre of the compression plane and it would intuitively have been expected that the grain size would increase with increasing strain. Instead the mean grain size is seen directly from Fig.2.6.8 to decrease with increasing strain, as a result of the macroscopic grain break-up and the formation of high angle boundaries. This has also been measured by linear intercept. The linear intercept length was measured for every 80μm both horizontally and vertically and the mean values of these intercept lengths are listed in Table 2.6.4. The scanned area on the starting material (0% deformed) is seen in Fig.2.6.8(a) to contain one large grain that makes the linear intercept length larger than for the 5% deformed sample. With this exception the linear intercept length is seen to decrease from 350μm to 190μm when the deformation is increased from 0% to 23%.
The pole figures and inverse pole figures in Fig.2.6.8 show that the orientations of all the grains spread out in a more or less spherical way for increasing strain. In general the orientations of the grains rotate towards the [100]-[110] edge in the inverse pole figure as expected in a compression experiment. It is however not possible to determine how much the individual grains have rotated because only the final state after the deformation is observed.

It was intended to calculate the orientation spread as a function of strain for individual grains in the polycrystals. However the macroscopic grain break-up and formation of high angle boundaries make this impossible. What looks like two different grains after the deformation could before the deformation have been one and the same grain. Calculation of the orientation spread of what looks like one grain after the deformation would only result in an underestimation of the true orientation spread.
The spots in the pole figures do however look rather diffuse, indicating a large orientation spread, but this is the case already at 0% deformation, see Fig.2.6.8(a). When the material at 0% deformation has a large orientation spread it means that the strain level of the deformed samples is much higher than expected.
Due to the massive formation of high angle boundaries during the deformation and the fact that the material appears to be pre-strained before the actual deformation it was not attempted to calculate the orientation spread in any of the grains in the aluminium polycrystals.

| Strain [%] | Linear intercept length [μm] |
|---|---|
| 0 | 302.1 |
| 5 | 342.7 |
| 11 | 276.2 |
| 16 | 200.7 |
| 23 | 191.8 |

*Tabel 2.6.4. Linear intercept length measured on aluminium polycrystals deformed in compression to five different strains. The linear intercept lengths are measured on the orientation images in Fig.2.7.1.*

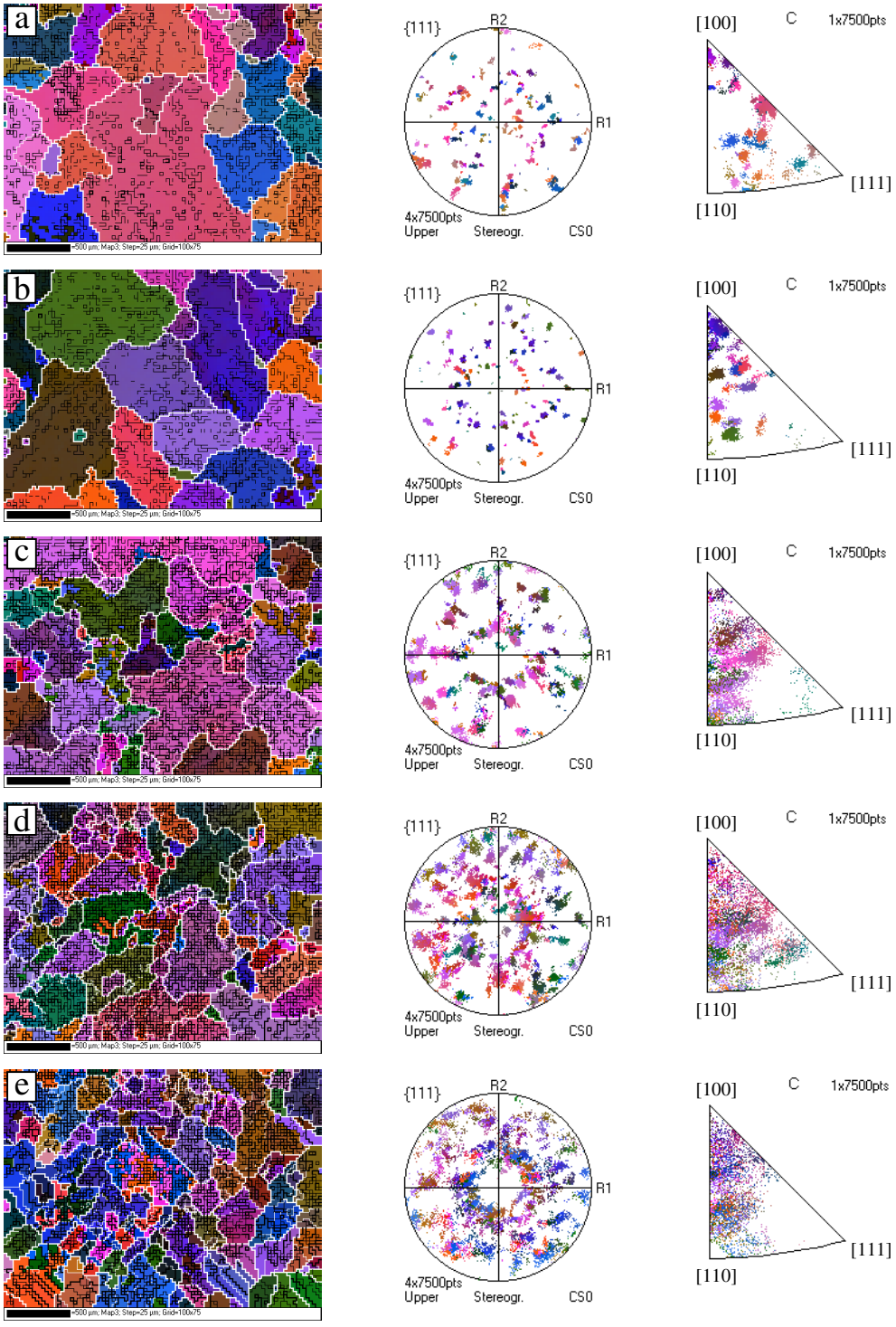


*Fig. 2.6.8. Orientation images of the compression plane of aluminium polycrystals deformed by uniaxial compression. a) The starting material with no deformation, b-e) are deformed to 5%, 11%, 16% and 23% reduction, respectively. The orientations of each point in the EBSP scans (of the compression plans) are plotted in the pole figures and the inverse pole figures that are next to the orientation images.*

# 3 The deformation and tracking experiment

As previously described in section 2.6.2 it is not possible to use electron microscopy to determine the texture evolution of individual grains in polycrystals during straining. Only the final state of the material after the deformation is observed. The X-ray tracking technique is a new non-destructive method that allows investigations of planar sections in the bulk of samples. All essential features like the position, volume, orientation, stress-state of the grains and the morphology of the grain boundaries can be determined. The tracking technique makes it possible to map the initial orientations of individual grains before the deformation as well as the final orientation after the deformation.
The X-ray tracking is therefore a perfect technique for investigating whether the deformation microstructure within a grain with a given crystallographic orientation depends on the previous lattice rotation and/or the crystallographic orientation of the neighbouring grains. By performing *in-situ* deformation of the sample while tracking the individual grains the evolution of the grain morphology and the grains orientations can be directly observed. Alternatively the undeformed sample can be mapped by the tracking technique and afterward deformed and sectioned at one of the mapped layers.
This alternative method was used in the preliminary experiment to follow the texture evolution in individual grains during deformation. The sample material in this experiment was the same commercially pure aluminium (99.4%) as used in the electron microscopy investigation in section 2.6.2. The investigated sample was machined to a cylinder with a diameter of 5mm and a height of 8mm and afterwards annealed for 24 hours at 500°C and slowly cooled to room temperature, in order to minimise the mosaic spread of the grains. The sample was polished at one surface and an EBSP scan was acquired. The tracking was performed 10µm below this sample surface and 20 other layers in the bulk of the sample were subsequently mapped. The sample was afterwards deformed by uniaxially compression outside the 3DXRD microscope to a final reduction of 10%.
Carnegie Mellon University (CMU) in Pittsburgh, USA, has specialised in serial sectioning and has reported that sectioning can be performed with a precision of 0.1µm (Adams *et al.*, 1999). The sample was therefore brought to CMU for sectioning at one of the layers mapped in the synchrotron experiment. After the sectioning this layer was investigated by electron microscopy (EBSP). The intention was to compare the microscopic observations after the deformation with the tracking results from the same layer before the deformation. Thus the texture evolution of individual grains could be determined.
Unfortunately, the sample was sectioned 30µm below the mapped layer. Furthermore the results from the tracking just below the surface do not agree with the EBSP observations. The tracking result shown in Fig.1.5.11 was acquired just before the present experiment. Only the sample was changed between the two experiments, but during the mounting of the new sample something in the experimental set-up must have been altered. The detector could have been moved or the rotational centre of the sample could have been lost in the aligning of the sample. The obtained tracking results from the bulk of the sample can therefore not be trusted and due to the sectioning at the wrong layer it is not possible to compare the EBSP and X-ray tracking results.
The described problems in the present experiment are due to regular misfortune which must be classified as initial difficulties that could be overcome by repeating the experiment. This has, however, not been possible due to the limited time for this project.

# 4 Conclusion

Two different synchrotron techniques have been developed, tested and applied in order to measure the rotation histories of the crystal lattice in individual grains during deformation. Both techniques are non-destructive and capable of mapping grain boundaries and the crystallographic orientation of grains in the bulk of polycrystalline samples.

The conical slit proved to be a useful tool for depth profiling, but difficult to align in the diffracted beam. An alignment method was developed, and the longitudinal resolution was found to be optimal for the {222} slit opening, where the gauge volume was determined to be 92μm in the longitudinal direction. The two other dimensions of the gauge volume are determined by the size of the incoming beam, which was limited by a square aperture to $22\times24\mu m^2$. The needle shaped gauge volume can be used to map the crystallographic orientation and the position of the grain boundaries as demonstrated. The position of the grain boundaries will be determined with different precision, depending on the orientation of the needle shaped gauge volume with respect to the grain boundary under investigation.

The conical slit consist of seven conical parts, which all suffer from some degree of eccentricity, even though the most modern wire electrodischarge machining was used in the manufacturing process. The design of the conical slit could be improved by manufacturing the device from one piece of tungsten. This would eliminate assemblage errors and cross-eyed slits could be avoided. The machining and assemblage errors limit the achievable resolution. The main drawback by using a conical slit is that it only works for samples that belong to one specific symmetry group and only at one specific energy. When using the conical slit in combination with a two-dimensional detector six full Debye-Sherrer rings can be recorded. Thus complete information on the texture from one particular gauge volume is provided in only one image. One Debye-Sherrer ring consist of several diffraction spots and a conical slit therefore provides a considerable faster way to obtain longitudinal resolution than traditional slits where each reflection has to be scanned individually.

The X-ray tracking technique proved to be even faster and therefore more suitable for three-dimensional mapping. The acquisition time for a complete map of $2.5\times2.5$ $mm^2$ in one layer was less than two minute. The positions of the grain boundaries in an undeformed aluminium sample were reconstructed from the tracking data with an average uncertainty of 26μm. The grain orientations were calculated with a precision of about 0.1°. The limit on the mapping accuracy is given by the width of the focal line, the detector resolution, and the accuracy of the sample movements. With present technology these factors can all be reduced to 1μm. In the present thesis only the raw X-ray data have been presented, but the spatial resolution of the grain boundary maps could be improved by averaging between different reflections from the same grain or between neighbouring grains. This averaging, however, can only be carried out by an automatic computer programme due to the large amount of X-ray data. Such a programme is presently being developed.

For deformed specimens, the mapping accuracy will be determined by the mosaic spread of the grains. The mosaicity leads to a one-dimensional spread of the intensity along the Debye-Scherrer rings in the images. Adding the intensity distributions in several images recorded at different sample rotations can solve this problem to some extent. However, for a large mosaic spread the diffraction

spots will overlap and it will not be possible to reconstruct the grain boundaries and calculate the mean crystallographic orientations.
The conical slit method is on the other hand not affected by mosaicity in the sample and it is therefore ideal for stress and strain measurements. For low strained samples the tracking technique can be extended to include strain and stress characterisation. By adding an area detector at a large distance from the sample and observing the small shifts in the angles $2\theta$ and $\eta$. The evolution of the average strain of each grain can in this way be followed *in-situ* during deformation.
The tracking technique was used in combination with X-ray tomography to study the wetting kinetics of liquid gallium in aluminium grain boundaries. The wetting results in a large variation in the amount of gallium present in different boundaries. Some boundaries are not penetrated while other boundaries become decorated with several microns of liquid gallium. The tracking technique has a lower spatial resolution than the X-ray tomography technique. However, the crystallographic orientations of the grains can be calculated from the tracking data. This makes it possible to investigate correlations between the amount of liquid Ga present in the boundaries and the grain boundary parameters, including misorientation and boundary plane normal. Furthermore, the tracking technique does not, as the tomography technique, depend on the presence of liquid gallium in the boundaries in order to detect the boundaries.
The electron microscopy investigation of the four single crystals with the macroscopic orientations [100], [110], [111] and [235] deformed in compression showed a significant macroscopic sub-division. The texture evolutions in the single crystals were found to agree reasonably well with model predictions, except for the [235] single crystal. The macroscopic sub-division results in a spread of the orientations. The orientation spreads were in all directions for the [100] and [110] single crystals but one-dimensional for the [111] and [235] single crystals. When using single crystals the orientations are known before the deformation. By measuring the final orientation after the deformation the texture evolution can be studied. The grains in the polycrystals deformed by uniaxially compression experienced a macroscopic sub-division and a formation of high angle boundaries. What looks like two different grains after the deformation could before the deformation have been one and the same grain. The electron microscopy investigation of the deformed polycrystals illustrates the need for a non-destructive technique to map the grain boundaries and grain orientations before the deformation.
The tracking technique has in several experiments proven to be useful for non-destructive depth profiling. The problems experienced with the preliminary tracking experiment to investigate the lattice rotation in individual grains (chapter 3) were due to regular misfortune. This experiment should be repeated in the future, and new information on the rotation history of the crystal lattice in individual grains would be gained.

# REFERENCER


Adams, B.L., Ta'asan, S., Kinderlehrer, D., Livshits, I., Mason, D.E., Wu, C.-T., Mullins, W.W., Rohrer, G.S., Rollett, A.D. and Saylor, D.M. (1999). Extracting grain boundary and surface energy from measurement of triple junction geometry. Interface Sci. **7** p. 321-338.

Altarelli, M., Schlachter, F. and Cross, J. (1998). Ultrabright X-ray machines. Sci. Am. **279**(6) p. 66-73.

Anongba, P.N.B., Bonneville, J. and Martin J.L. (1993). Hardening stages of [112] Cupper single-crystals at intermediate and high – temperatures. 2. Slip systems and microstructures. Acta Metall. Mater. **41**(10) p. 2907-2922.

Bartholomew, R.N. and Casagrande, R.M. (1957). Measuring solids concentrations in fluidized systems by gamma-ray absorption. Ind. Eng. Chem. **49**(3) p. 428-431.

Bay, B, Hansen, N., Hughes, D.A. and Kuhlmann-Wilsdorf, D. (1992). Evolution of fcc deformation structures in polyslip. Acta Metall. Mater. **40** p. 205-219.

Bragg, W.L. (1913). The diffraction of short electromagnetic waves by a crystal. Proc. Camb. Phil. Soc. **17** p. 43-57.

Bunge, H.J. (1982). Texture analysis in materials science. London, Butterworth.

Busing, W.R. and Levy, H.A. (1967). Angle calculations for 3- and 4- circle X-ray and neutron diffractometers, Acta Cryst. **22** p. 457-464.

Clarke, D.R. and Gee, M.L. (1992). Material interfaces. Edited by D. Wolf and S. Yip, Chapman & Hall, London.

Dawson, P.R., Beaudoin, A.J. and Mathur, K.K. (1994). Finite element modelling of polycrystalline solids. In: Numerical predictions of deformation processes and the behaviour of real materials. Edited by S.I. Andersen *et al*. (Risø National Laboratory, Roskilde), p. 33-44.

Desre, P.J. (1997). A mechanism for the stress independent grain boundary penetration of a metal by a liquid metal. Application to the metallic couple Al-Ga, Scripta Mater. **37**(6) p. 875-881.

Fernandes, P.J.L. and Jones, D.R.H. (1997). Mechanisms of liquid metal induced embrittlement, Inter. Mater. Rev. **42**(6) p. 251-261.

Friedrich, W., Knipping, P. and Laue, M. (1912). Interferenz-Erscheinungen bei Röntgenstrahlen. Sitz. Math. Phys. Klasse Bayer. Akad. Wiss., p. 303-322.

Giacovazzo, C., Monaco, H.L., Viterbo, D., Scordari, F., Gilli, G., Zanotti, G. and Catti, M. (1991). Fundamentals of crystallography. Oxford university press, Oxford.

Glickman, E., and Nathan, M. (1999). On the kinetic mechanism of grain boundary wetting in metals, J. Appl. Phys. **85** p. 3185-3191.

Hammersley, A.P., Svensson, S.O., Hanfland, M., Fitch, A.N. and Häusermann, D. (1996). Two-dimensional detector software: From real detector to idealised image or two-theta scan. High Press. Res. 14 p. 235-248.

Hansen, J., Pospiech, J. and Lücke (1978). Tables of texture analysis of cubic crystals, Springer-verlag, Berlin.

Hansen, N. (1990). Cold deformation microstructures. Mater. Sci. Techn. **6**(11) p. 1039-1047.

Hansen, N. and Huang, X. (1998). Microstructure and flow stress of polycrystals and single crystals. Acta Mater. **46**(5) p. 1827-1836.

Henry, N.F.M and Lonsdale, K. (1965). International tables for X-ray crystallography. International Union of Crystallography, Birmingham.

Higashi, K., Nieh, T.G., Mabuchi, M. and Wadsworth, J. (1995). Effect of liquid phases on the tensile elongation of superplastic aluminium alloys and composites. Scripta Metal. Mater. **32**(7) p. 1079-1084.

Hough, P.V.C. (1962). A method and means for recognizing complex patterns, U.S. Patent 3,069,654.

Huang, X. (1998). Grain orientation effect on microstructure in tensile strained copper. Scripta Mater. **38**(11) p. 1697-1703.

Huang, X. and Hansen, N. (1997). Grain orientation dependence on microstructure in alluminium deformed by tension. Scripta Mater. **37**(1) p. 1-7.

Huang, X. and Juul Jensen, D. (2000). EBSP contra TEM characterization of a deformed aluminium single crystal. In: Electron backscatter diffraction in materials science. Edited by A.J. Schwartz *et al*., Kluwer Academic/Plenum Publisher, New York, p. 265-276.

Hugo, R.C. and Hoagland, R.G. (1998). In-situ TEM observation of aluminum embrittlement by liquid gallium. Scripta Mater. **38**(3) p. 523-529.

Hull, D. and Bacon, D.J. (1984). Introduction to dislocations. Pergamon Press, Oxford.

Humbert, M.,Gey, N., Muller, J. and Esling, C. (1996). Determination of a mean orientation from a cloud of orientations. Application to electron backscattering pattern measurements. J. Appl. Cryst. **29** p. 662-666.

Häuserman, D. and Itié, J.P. (1992). Conical geometry energy dispersive diffraction – 1st results. Rev. Sci. Instrum. **63**(1) p. 1080-1082.

Ice, G. (2000). Letting the grains show their strains. Mater. World, **8**(5) p. 20-21.

Johnson, W.H. (1874). On some remarkable changes produced in iron and steel by the action of hydrogen and acids. Proc. R. Soc. Lond. **23** p. 168-179.

Joy, D.C., Newbury, D.E. and Davidson, D.L (1982). Electron channeling patterns in the scanning electron microscope. J. Appl. Phys. **53** p. 81-122.

Juul Jensen, D. and Poulsen, H.F. (2000). Recrystallization in 3D. In: Proceedings of the 21$^{th}$ international symposium on materials science: Recrystallization – fundamental aspects and relations to deformation microstructure. Edited by N. Hansen *et al*. (Risø National Laboratory, Roskilde), p.103-124.

Kaftandjian, V., Peix, G., Babot, D., Peyrin, F. (1996). High resolution X-ray computed tomography using a solid-state linear detector. J. of X-ray Science and technology. **6** p. 94-106.

Kak, A.C. and Slaney, M. (1988). Principles of computerized tomographic imaging. IEEE Press. New York. (An electronic version of this book is available on http://www.slaney.org/pct/).

Kawasaki, Y. (1974). Cell structures in deformed copper single crystals. J. Phys. Soc. Jap. **36** p. 142-148.

Kawasaki, Y. (1994). Relationship between deviations from slip planes and slip systems of layered dislocation structures in deformed copper single crystals. In: Strength of materials. Edited by Oikawa *et al.* Japan Inst. Met., p. 187-190.

Kiss, K. (1988). Problem solving with microbeam analysis. Elsevier.

Kocks, U.F. and Canova, G.R. (1981). How many slip systems and which? In: Deformation of polycrystals: Mechanisms and microstructures. Proceedings of the 2$^{th}$ International symposium on metallurgy and materials science. Edited by N. Hansen *et al.* (Risø National Laboratory, Roskilde), p. 35-44.

Kocks, U.F., Tomé, C.N. and Wenk, H.-R. (1998). Texture and anisotropy. Cambridge University Press, Cambridge.

Krieger Lassen, N.C. (1994). Automated determination of crystal orientations from electron backscattering patterns. Ph.D. thesis, Institude of Mathematical Modelling (IMM), Technical University of Denmark, Lyngby.

Krieger Lassen, N.C. and Juul Jensen, D. (1994). On the statistical analysis of orientation data. Acta Cryst. **A50** p. 741-748.

Krieger Lassen, N.C., Juul Jensen, D. and Conradsen K. (1992). Image processing procedures for analysis of electron back scattering patterns. Scanning Microscopy **6**(1) p. 115-121.

Kröner, E. (1961). Zur plastichen verformung des veilkristalls. Acta Metall. **9** p. 155-161.

Kuhlmann-Wilsdorf, D. and Hansen, N. (1991). Geometrically necessary, incidental and subgrain boundaries. Scr. Metall. Mater. **25** p.1557-1562.

Lauridsen, E.M., Juul Jensen, D., Poulsen, H.F. and Lienert, U. (2000a). Kinetics of individual grains during recrystallization. Scripta Mater. **43**(6) p. 561-566.

Lauridsen, E.M., Schmidt, S., Poulsen, H.F. and Suter, R.M. (2000b). Structural characterization of grains in powders or polycrystals. In preparation.

Leffers, T. and Bilde-Sørensen, J.B. (1990). Intra- and intergranular heterogenities in the plastic deformation of brass during rolling. Acta Metall. Mater. **38** p. 1917-1926.

Lienert, U., Martins, R., Grigull, S., Pinkerton, M., Poulsen, H.F. and Kvick, Å. (2000b). High spatial resolution strain measurements within bulk materials by slit-imaging. Mat. Res. Soc. Symp. Proc. **590** p. 241-246.

Lienert, U., Poulsen, H.F., Honkimaki, V., Schulze, C. and Hignette, O. (1999a). A focusing multilayer analyser for local diffraction studies. J. Synchrotron Rad. **6** p. 979-984.

Lienert, U., Poulsen, H.F., Kvick, Å. (1999b). Proceedings of the 40$^{th}$ conference of the american institute of aeronautics and astronautics on structures, structural dynamics and materials (St. Luis, USA), p. 2067-2075.

Lienert, U., Poulsen, H.F., Martins, R.V. and Kvick, Å. (2000a). High energy microscope for local strain measurements within bulk materials. Mater. Sci. Forum **347** p. 95-100.

Ludwig, W., and Bellet, D. (2000). Penetration of liquid gallium into the grain boundaries of aluminium: a synchrotron radiation microtomographic investigation, Mater. Sci. and Eng. **A281** p. 198-203.

Mackenzie, J.K. (1958). Second paper on statistics associated with the random disorientation of cubes. Biometrika **45** p. 229-240.

Mackenzie, J.K. and Thomson, M.J. (1957). Some statistics associations with the random disorientation of cubes. Biometrika **44** p. 205-210.

Mecking, H. (1981). Low temperature deformation of polycrystals. In: Deformation of polycrystals: Mechanisms and microstructures. Proceedings of the 2$^{th}$ International symposium on metallurgy and materials science. Edited by N. Hansen *et al*. (Risø National Laboratory, Roskilde), p. 73-86.

Morawiec, A. (1998). A note on mean orientation. J. Appl. Cryst. **31** p. 818-819.

Morawiec, A. and Pospiech, J. (1989). Some information on quaternions useful in texture calculations. Textures Microstruct. **10** p. 211-216.

Mullins, W.W. (1957). Mass transport at interfaces in single component systems. Metall. Mater. Trans. **A26**, p. 1917-1929.

Naaman, H., Talreja, R., Juul Jensen, D. and Hansen, N. (1987). Development of deformation textures in polycrystalline copper experiments and model predictions. Textures Microstruct. **7** p. 149-170.

Poulsen, H.F., Garbe, S., Lorentzen, T., Juul Jensen D., Poulsen, F.W., Andersen, N.H., Frello, T., Feidenhansl, R. and Graafsma, H. (1997). Applications of high-energy synchrotron radiation for structural studies of polycrystalline materials. J. Synchrotron Rad. **4** p. 147-154.

Proceedings. 20th Risø international symposium on materials science, Risø (DK), Deformation-induced microstructures: Analysis and relation to properties. Risø National Laboratory, Roskilde, 1999.

Rabkin, E. (1998). Coherency strain energy as a driving force for liquid grooving at grain boundaries, Scripta Mater. **39**(6) p. 685-690.

Sachs, G. (1928). Zur ableitung einer fliessbedingug. Z. Verein Deut. Ing. **72** p. 734-736.

Schou, J. (1988). Secundary electron emission from solids by electron and proton bombardment. Scanning Microsc. **2** p. 607-632.

Straumal, B., Gust, W. and Molodov, D. (1994). Tie lines of the grain boundary wetting phase transition in the Al-Sn system. J. Phase Equilibria. **15**(4) p. 386-391.

Suortti, P. (1977). Accuracy of structure factors from X-ray powder intensity measurements. Acta Cryst. **A33** p. 1012-1027.

Swann, P.R. (1963). Dislocation arrangements in face-centred cubic metals and alloys. In: Electron microscopy and strength of crystals. Edited by G. Thomas and J. Washburn, Interscience, New York, p.131-181.

Taylor, G.I. (1938). Plastic strain in metals. J. Inst. Met. **62** p. 307-324.

Warren, B.E. (1969). X-ray diffraction. Dover publications, New York.

Williams, D.B. and Carter, C.B. (1996). Transmission electron microscopy. Diffraction. Plenum Press, New York.

Winther, G., Huang, X. and Hansen, N. (2000a). Crystallographic and macroscopic orientations of planar dislocation boundaries – correlations with grain orientation. Acta Mater. **48** p. 2187-2198.

Winther, G., Huang, X., Nielsen, S.F. and Wert, J. (2000b). Dislocation boundaries and slip systems in uniaxially deformed [110] Al single crystals. In preparation.

Woolfson, M.M. (1996). An introduction to X-ray crystallography. Cambridge University Press, Cambridge.

Wroblewski, T., Clauss, O., Crostack, H.A., Ertel, A., Fandrich, F., Genzel, C., Hradil, K., Ternes, W. and Woldt, E. (1999). A new diffractometer for materials science and imaging at HASYLAB beamline G3. Nucl. Inst. Meth. **A428** p. 570-582.

# APPENDIX A

**The crystallographic orientation**

The calculation of the crystallographic orientation in an X-ray experiment is a complex procedure where one has to keep track of all possible translations and rotations of the sample relative to the incoming beam in several different co-ordinate systems. The following demonstrates how the orientation can be calculated from the experimental tracking set-up. The orientation could of cause be calculated from another experimental set-up like for example the conical slit set-up. The calculations have been carried out for X-ray or neutron single crystal diffractometers (Busing & Levy, 1967) and their calculations can be used directly to establish the orientation of a grain from the observed angles of at least two different reflections from the grain under investigation. The different co-ordinate systems that have to be considered and the procedure for the orientation calculation will be outlined in the following. A more detailed discussion can be found in Busing & Levy (1967), Lauridsen *et al.* (2000b) and Giacovazzo *et al.* (1991).

**The basic diffractometer equation**

A basic equation for the diffraction in a reference co-ordinate system can be established by considering five different Cartesian co-ordinate systems: the laboratory system, the tilted system, the ω-system, the sample system and the Cartesian grain system. The characteristics of these systems will be described in the following.

*The laboratory co-ordinate system* ($x_{lab}$,$y_{lab}$,$z_{lab}$) is a right-hand system with the $x_{lab}$ axis along the incoming white beam. $y_{lab}$ is transverse to $x_{lab}$ and the vertical $z_{lab}$ which is positive upwards. A Si (111) crystal is used in the optics box to make the beam monochromatic. This causes the monochromatic beam to exit the optics box with an angle $2\theta_m$ with respect to the direct beam (at 50keV we get $2\theta_m$=4.53°) and this defines the *tilted co-ordinate system* ($x_t$,$y_t$,$z_t$) with the $x_t$-axis along the monochromatic beam (see Fig.A1).

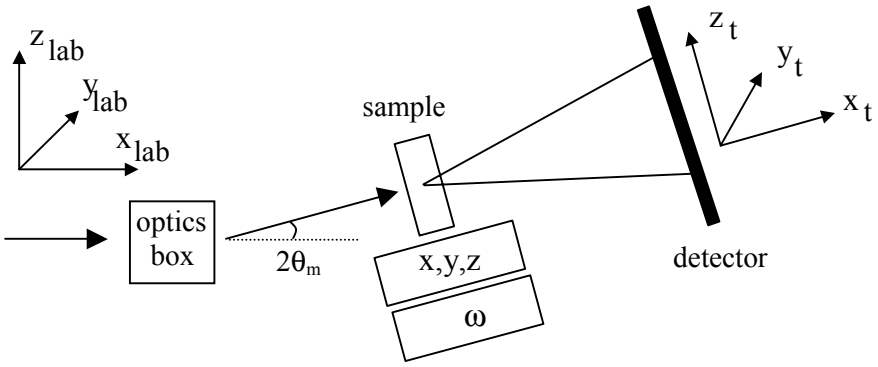


*Fig. A1. Illustration of the laboratory and the tilted co-ordinate system. The laboratory system has the x axis along the white beam and the tilted system has the x axis along the monochromatic beam. The sample stage with the x,y and z translations and the ω rotation are all tilted with the angle $2\theta_m$ of the monochromatic beam.*

*The tilted system* is the natural reference system for the measurements because the sample stage with both the ω-rotation and the sample translations are tilted with $2\theta_m$ with respect to the beam. The relation between the laboratory system and the tilted system can be described with the matrix operation

$$\begin{pmatrix} x_t \\ y_t \\ z_t \end{pmatrix} = \begin{pmatrix} \cos(2\theta_m) & 0 & \sin(2\theta_m) \\ 0 & 1 & 0 \\ -\sin(2\theta_m) & 0 & \cos(2\theta_m) \end{pmatrix} \begin{pmatrix} x_{lab} \\ y_{lab} \\ z_{lab} \end{pmatrix} \tag{A1}$$

The detector is also tilted in such a way that the detector plane is perpendicular to the beam at a distance of L from the sample. A recorded two dimensional image from the detector is equivalent to looking at the detector from the sample position in the beam direction. The detector co-ordinates are $y_{det}$ (horizontal) and $z_{det}$ (vertical). The direct beam define the zero point ($y_{0,det}$, $z_{0,det}$) on the detector. A diffraction spot on the detector is then defined by the scattering angle 2θ and the azimuthal angle η on the detector. The azimuthal angle on the detector is positive clockwise and zero at the top as illustrated in Fig.A2.

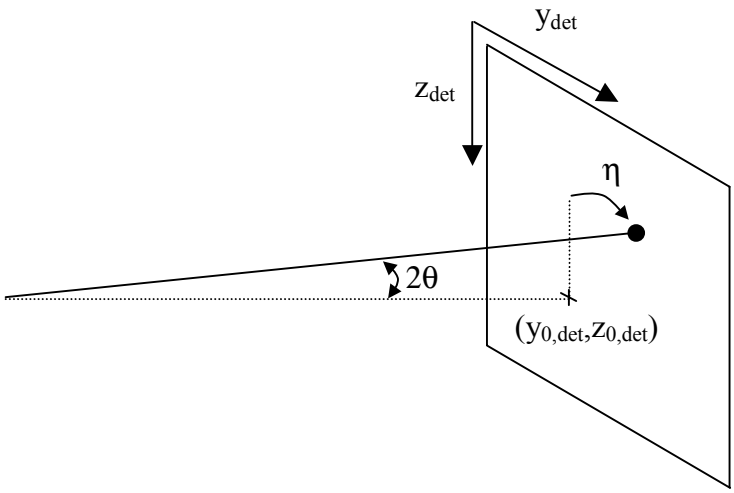


*Fig. A2. Illustration of the detector co-ordinate system. The axes on the detector start at the upper left corner. The direct beam defines the zero-point on the detector, and each diffraction spot is defined by the scattering angle 2θ and the azimuthal angle η.*

The scattering vector $G_t$ in the tilted system can be found directly by inspection of Fig.A2 to

$$\mathbf{G}_t = \frac{2\pi}{\lambda} \begin{pmatrix} \cos(2\theta) - 1 \\ \sin(2\theta)\sin(\eta) \\ \sin(2\theta)\cos(\eta) \end{pmatrix} \tag{A2}$$

where $2\pi/\lambda$ is required to get the right length of the vector. The length of the scattering vector in the reciprocal space is related to the lattice spacing in the direct space by $|\mathbf{G}_t| = 2\pi/d$ and by using the Bragg law ($\lambda=2d\sin\theta$) we find that the length of the scattering vector is $|\mathbf{G}_t| = (4\pi/\lambda)\sin\theta$ which is consistent with equation (A2).

*The omega co-ordinate system* ($x_\omega$,$y_\omega$,$z_\omega$) is defined by the omega rotation in such a way that ω=0 when $x_\omega$ is parallel to $x_t$, $y_\omega$ is parallel to $y_t$ and $z_\omega$ is parallel to $z_t$. The ω rotation is positive clockwise when observed from the above. The omega system is related to the tilted system by the rotation matrix Ω

$$\mathbf{G}_t = \mathbf{\Omega G}_\omega \tag{A3}$$

$$\textit{where} \qquad \mathbf{\Omega} = \begin{pmatrix} \cos(\omega) & \sin(\omega) & 0 \\ -\sin(\omega) & \cos(\omega) & 0 \\ 0 & 0 & 1 \end{pmatrix} \tag{A4}$$

*The sample co-ordinate system* ($x_s$,$y_s$,$z_s$) defines how the sample is mounted on the rotation stage with respect to the deformation axes of the sample, if any. This gives the relation

$$\mathbf{G}_\omega = \mathbf{S G}_s \tag{A5}$$

The sample will typically be aligned so the axes in the sample system will be $x_s$=RD,$y_s$=TD and $z_s$=ND. This gives a very simple *S* matrix:

$$\mathbf{S} = \begin{pmatrix} 1 & 0 & 0 \\ 0 & 1 & 0 \\ 0 & 0 & 1 \end{pmatrix} \tag{A6}$$

The Cartesian grain system ($x_c$,$y_c$,$z_c$) is defined with respect to the Cartesian axes in the grain under investigation

$$\mathbf{G}_s = \mathbf{U G}_c \tag{A7}$$

where *U* is the orthogonal matrix which relates the sample system with the Cartesian grain system.
The Miller indices (h,k,l) describe a dimensionless vector:

$$\mathbf{G}_{hkl} = \begin{pmatrix} h \\ k \\ l \end{pmatrix} \tag{A8}$$

in the reciprocal space. This vector has to be transformed into the Cartesian grain system before other operations like for example the ω-rotation can be performed. The direct space lattice and the reciprocal space lattice can be described by the parameters a,b,c,α,β,γ and a*,b*,c*,α*,β*,γ* respectively as illustrated for the direct lattice in Fig.A3.

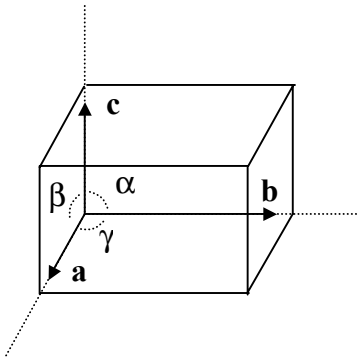


*Fig. A3. Illustration of the lattice vectors a, b and c and the angles between the vectors α, β and γ.*

The correspondence between the Cartesian grain system and the reciprocal space can be written as

$$\mathbf{G}_c = \mathbf{B}\mathbf{G}_{hkl} \tag{A9}$$

$$\text{where} \quad \mathbf{B} = \begin{pmatrix} a^* & b^*\cos(\gamma^*) & c^*\cos(\beta^*) \\ 0 & b^*\sin(\gamma^*) & -c^*\sin(\beta^*)\cos(\alpha) \\ 0 & 0 & 2\pi/c \end{pmatrix} \tag{A10}$$

The B matrix rotates the $G_{hkl}$ vector to a Cartesian co-ordinate system and ensures the right dimension ($G_{hkl}$ is dimensionless). In the case of a cubic crystal we have a*=b*=c*, a*=2π/a and α*=β*=γ*=π/2. The B matrix will in this case reduce to a matrix with 2π/a in the diagonal. In the cubic system the B matrix do nothing else than ensuring the right length of the $G_{hkl}$ vector in the Cartesian grain system.

If all the operations in the five co-ordinate systems are put together we get the basic diffractometer equation:

$$\mathbf{G}_t = \mathbf{\Omega}\mathbf{S}\mathbf{U}\mathbf{B}\mathbf{G}_{hkl} \tag{A11}$$

This equation describes the scattering vector as observed in the tilted co-ordinate system, which as already mentioned is the natural reference system.

**The crystallographic orientation in Euler angles**

A poly-crystal is a collection of grains, each with its own crystal lattice. The macroscopic orientations of the different grains are given by the orientations of the crystal lattices with respect to the external axes of the sample. A co-ordinate system $(x_c, y_c, z_c)$ can be fixed to crystal lattice by placing the vectors on three characteristic directions of the crystal lattice that are normal to each other. The sample co-ordinate system that defines the external axes of the sample can be denoted $(x_s, y_s, z_s)$. The orientation of the grain can now be described as the orientation of $(x_c, y_c, z_c)$ with respect to $(x_s, y_s, z_s)$ and this is often done by using the three Euler angles $\varphi_1$, $\Phi$, $\varphi_2$ (Bunge, 1982). Three successive rotations have to be carried out to bring the sample system into the same angular position as the crystal lattice. Fig.A4 illustrates the three rotations e.g. the Euler angles. The sample co-ordinate system $(x_s, y_s, z_s)$ is first rotated $\varphi_1$ around $z_s$. The rotated sample system $(x'_s, y'_s, z'_s)$ is now rotated $\Phi$ around $x'_s$, which brings $z'_s$ to coincide with $z_c$. In order to bring the two other axes into position a final rotation of $\varphi_2$ around $z'_s$ is carried out. With this definition of the Euler angle where the range of the angles is 0-360° for $\varphi_1$ and $\varphi_2$ and 0-180° for $\Phi$ there will exist 24 equivalent Euler representations of each crystal orientation in an fcc material (Hansen *et al.*, 1978).

To determine the orientation of the grain under investigation in the X-ray experiment we need to solve the diffractometer equation (A11) with respect to the U matrix. This matrix can be thought of as a rotation matrix that brings the $G_c$ vector from one Cartesian co-ordinate system to another. The co-ordinate system after the rotation will only be unambiguous defined if at least two vectors are rotated into the co-ordinate system. It is therefore necessary to sort out all reflections from one grain, and use those to find the U matrix that rotates all of them in the correct way.

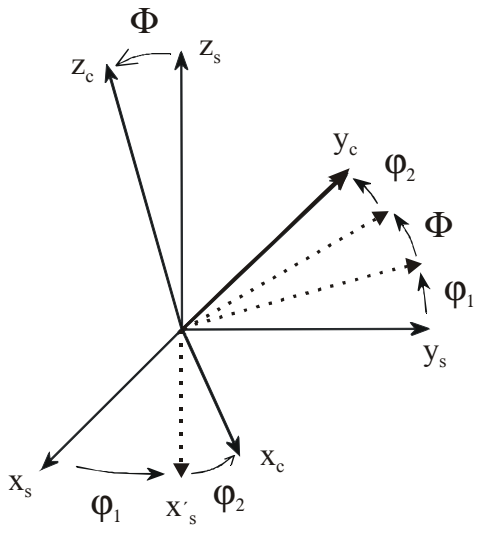


*Fig. A4. The Euler angles $\varphi_1$, $\Phi$, $\varphi_2$ describes the orientation of the crystal co-ordinate system ($x_c, y_c, z_c$) with respect to the sample co-ordinate system ($x_s, y_s, z_s$).*

For each reflection the scattering angle 2θ and the azimuth angle η is known and the length of the scattering vector in the tilted co-ordinate system can be calculated. This allows us to assign a $G_{hkl}$ to each reflection where the vector has to end after the operation with the U matrix. There are 24 symmetrical equivalent $G_{hkl}$ vectors that could be assigned to each measured reflection. In practice one $G_{hkl}$ vector is chosen for each reflection, and one U matrix is computed out of several symmetrical equivalent possible matrices. E.M. Lauridsen has written a programme that finds the U matrix from a set of reflections from the same grain. The program is directly based on Busing & Levy (1967). When the U matrix has been established it is easy to convert it into the g matrix in the Bunge notation

$$\mathbf{g} = \mathbf{U}^{-1} = \mathbf{U}^{\mathrm{T}} \tag{A12}$$

where the formulas are well established. According to Hansen *et al.* (1978) the Euler angles $\varphi_1$,$\phi$ and $\varphi_2$ can be calculated from the U matrix by the following relations:

$$\mathbf{g} = \begin{pmatrix} U_{11} & U_{21} & U_{31} \\ U_{12} & U_{22} & U_{32} \\ U_{13} & U_{23} & U_{33} \end{pmatrix}$$

$$= \begin{pmatrix} \cos(\varphi_1)\cos(\varphi_2) - \sin(\varphi_1)\sin(\varphi_2)\cos(\phi) & \sin(\varphi_1)\cos(\varphi_2) + \cos(\varphi_1)\sin(\varphi_2)\cos(\phi) & \sin(\varphi_2)\sin(\phi) \\ -\cos(\varphi_1)\sin(\varphi_2) - \sin(\varphi_1)\cos(\varphi_2)\cos(\phi) & -\sin(\varphi_1)\sin(\varphi_2) + \cos(\varphi_1)\cos(\varphi_2)\cos(\phi) & \cos(\varphi_2)\sin(\phi) \\ \sin(\varphi_1)\sin(\phi) & -\cos(\varphi_1)\sin(\phi) & \cos(\phi) \end{pmatrix} \tag{A13}$$

When the Euler angles have been calculated from the U matrix by using equation (A13) we have a representation of the crystallographic orientation of the grain under investigation. It is not an unambiguous representation because 24 symmetrical equivalent sets of Euler angles exist which all represent the same crystallographic orientation. This is however not a problem if we are looking at misorientations, because a misorientation between to sets of Euler angles is traditionally defined as the smallest possible misorientation between all the symmetrical equivalent representations of the two sets.

APPENDIX B

**Pole figures**

A pole figure is a stereographic projection that shows the distribution of crystallographic orientations in the sample. The axes of the reference system are usually chosen so they correspond to easily defined directions in the sample. In a rolled sheet it would be natural to choose the rolling direction (RD), the transverse direction (TD) and the normal direction (ND) of the rolling plane.

A (hkl) plane in crystalline sample that is positioned in the centre of an orthogonal (x,y,z) co-ordinate system has a normal that intersects a unit reference sphere at a particular point. This point on the reference sphere is the (hkl)-pole. Fig.B1 illustrates two different (hkl)-poles, marked a and b. To represent all the poles in a two-dimensional plot, the poles can be projected stereographically on a pole figure plane. If the equatorial plane in the reference sphere is chosen as the pole figure plane, then the stereographic projection of a pole is obtained by projection from either the south pole or the north pole onto the equatorial plane. In Fig.B1 the stereographic projection is performed by drawing lines from the poles a and b to the south pole S. The points A and B at which the lines cuts the equatorial plane are the stereographic projection of the poles a and b. In the pole figure plane each point represents the orientation of the normal to a crystal plane with respect to a set of sample axes.

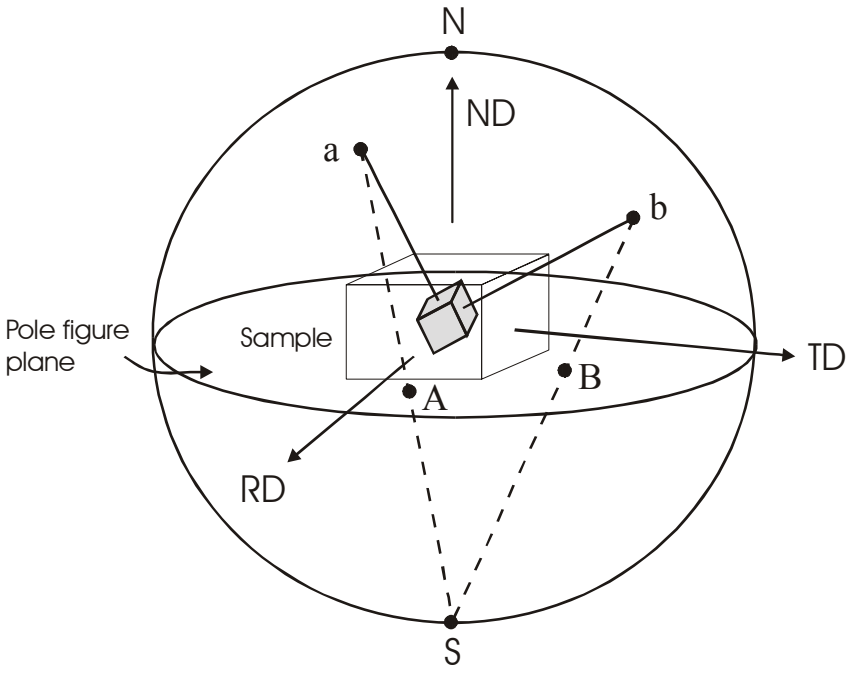


*Fig. B1. The sample is centred in a reference sphere and the poles a and b are projected stereographically to A and B on the equatorial plane which is the pole figure plane.*

**Inverse pole figures**

In the pole figure each point represents the orientation of the normal to a crystal plane with respect to a set of sample axes. In an inverse pole figure it is the other way around. Here a single reference direction (e.g. the tensile or compression axis) is plotted with respect to the crystal axes [001], [010] and [100]. The inverse pole figure will therefore show the crystal symmetry while the pole figure will be subject to the sample symmetry. Fig.B2 shows a cubic [100] crystal, modified with faces to illustrate the {101} and {111} lattice planes.

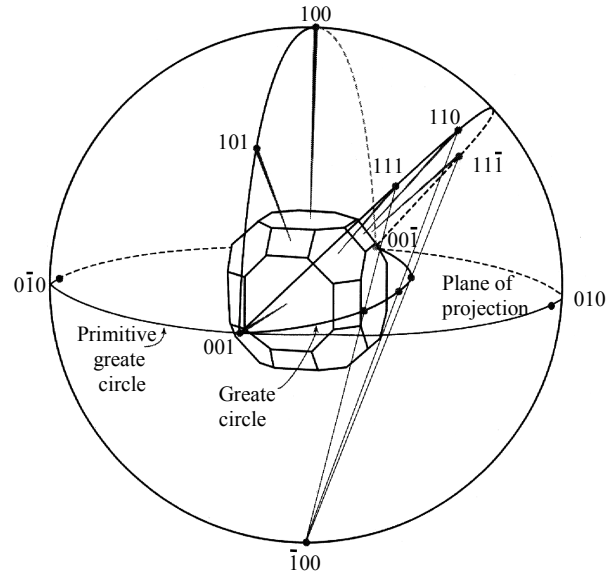


*Fig. B2. The sample is centred in a reference sphere and the poles a and b are projected stereographically to A and B on the equatorial plane which is the pole figure plane. (Williams & Carter, 1996)*

The normals to the (100),(111),(011) and ($\bar{1}$11) planes intersect the reference sphere in poles that all project onto a great circle on the stereographic projection. All poles from planes, which have parallel edges (i.e. parallel intersections between the planes) will project onto a great circle on the stereographic projection. Such a set of planes constitutes a zone and the common direction of the edges is known as the zone axis. The low index crystal planes can be can be grouped into nine zones:

| Zone | (hkl) indices of crystal planes |
|---|---|
| *a* | (00$\bar{1}$), (01$\bar{1}$), (010), (011), (001), (0$\bar{1}$1), (0$\bar{1}$0), (0$\bar{1}\bar{1}$) |
| *b* | (001), (101), (100), (10$\bar{1}$), (00$\bar{1}$) |
| *c* | (010), (110), (100), (1$\bar{1}$0), (0$\bar{1}$0) |
| *d* | (0$\bar{1}$1), (1$\bar{1}$1), (100), (11$\bar{1}$), (01$\bar{1}$) |
| *e* | (011), (111), (100), (1$\bar{1}\bar{1}$), (0$\bar{1}\bar{1}$) |
| *f* | (001), (1$\bar{1}$1), (0$\bar{1}$1), (1$\bar{1}\bar{1}$), (00$\bar{1}$) |
| *g* | (001), (111), (110), (11$\bar{1}$), (00$\bar{1}$) |
| *h* | (010), (11$\bar{1}$), (10$\bar{1}$), (1$\bar{1}\bar{1}$), (0$\bar{1}$0) |
| *i* | (010), (111), (101), (1$\bar{1}$1), (0$\bar{1}$0) |

Zone a corresponds to the primitive great circle in the plane of projection (see Fig.B2). The zones *b,c,d* and *e* appear as straight lines connecting the poles that

lie in the same zone and the zones *f-i* appear as different great circles. The nine zones are plotted in Fig.B3 in different colours. The subdivision of the inverse pole figure in 48 stereographic triangles expresses the crystal symmetry. Only 24 triangles are visible in Fig.B3 corresponding to the upper hemisphere of the pole figure.

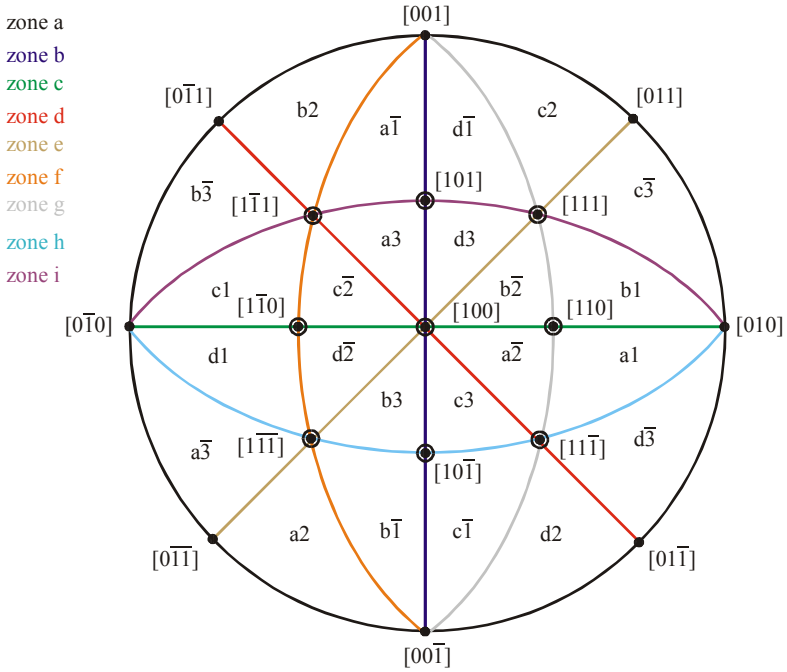


*Fig. B3. An inverse [100] stereographic projection with the nine zones in different colours. Each triangle corresponds to a particular slip system in a cubic crystal.*

Usually no distinction is made between families of directions. An inverse pole figure can therefore be plotted in a fundamental area of the full stereographic projection. The sample symmetry determines the size of the fundamental area. Consider two single crystal with orientations A and B indicated in Fig.B4(a) by their Z-axis. The directions to the X-axis of the sample are shown as long flags. These two orientations are not necessarily symmetrically equivalent representations of the same orientation.

Due to the mirror plane perpendicular to $[1\,\bar{1}\,0]$ a sample with the orientation A will have an equivalent pole at B', see Fig.B4(b). The long and short flags show the direction toward the X- and Y-axis, respectively. The right-handed pole triplet at A is mirrored into the left-handed pole triplet at B'. If A is rotated around $[1\,\bar{1}\,0]$ then the pole will be on the lower hemisphere at C. The pole triplet at C will still be right-handed after the rotation. If the C pole is projected on the upper hemisphere, then all the axes would change signs and the pole triplet would be left-handed and identical with B'. Due to the two-fold axis at $[1\,\bar{1}\,0]$ we see that A and B' are equivalent and C and B' are identical, see Fig.B4(b).

In Fig.B4(a) we do not have the directions toward the Y-axis for the two crystal orientations. The implicit assumption would be that both were described in right-handed co-ordinate systems as illustrated in Fig.B4(c). If that is the case then the two orientations are not equivalent by any crystal symmetry and both of the stereographic triangles are needed to represent the two crystal orientations.

The orientations A and B will only be equivalent in the case of sample symmetry. If for example the Z-X plane in the sample is a mirror plane then the flags

towards the Y-axis would go in both directions, see Fig.B4(d). By sample symmetry in this context is meant the symmetry of one grain in a polycrystal that has an equivalent partner somewhere, given by the symmetry of the microstructure or the symmetry of the testing (Kocks *et al.*, 1998).

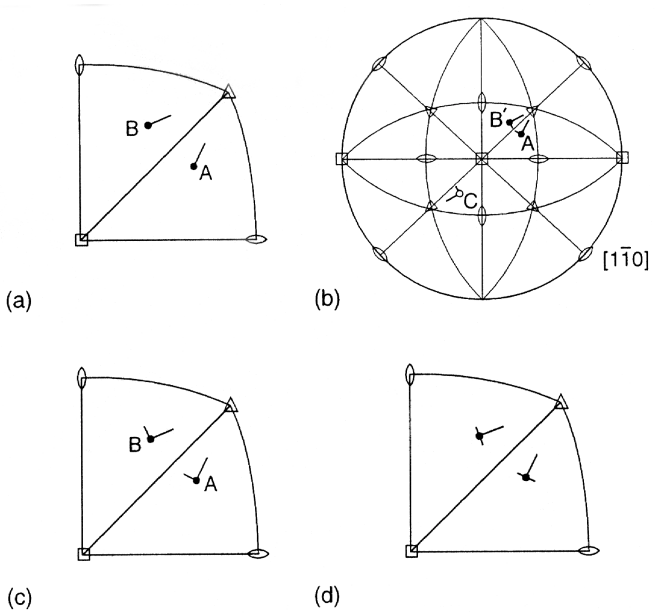


*Fig. B4. (a) Two orientations A and B of cubic crystals in an inverse pole figure. The plotted axis is the sample axis Z and the long flag is the direction toward the X axis. (b) Due to the mirror plane perpendicular to* [1 $\bar{1}$ 0] *the orientation A will have an equivalent pole at B' but they are only equivalent if B' is a left-handed co-ordinate system. The short flag indicates the direction of Y. (c) A and B' are not equivalent if they are both right-handed sample co-ordinate systems (d) However, A and B do become equivalent if there is a sample mirror plane perpendicular to the Y-direction.*

The triangle with the [1 0 0], [1 1 0] and [1 1 1] corners is traditionally called the primary stereographic triangle. For all orientations of fcc crystals within this triangle the Schmid factor for the [1 0 1](1 1 $\bar{1}$) slip system is higher than for all other systems. Single slip on this slip system would therefore be expected. If the compression axis lies on one of the boundaries of a triangle then two slip systems are equally favoured. The second slip system is the one with the highest Schmid factor in the adjoining triangle. The slip systems are labelled in Fig.B3 and the slip directions and planes are defined in Table B1.

| Plane | a = (1 1 1) | b = ($\bar{1}$ $\bar{1}$ 0) | c = ($\bar{1}$ 1 1) | d = (1 $\bar{1}$ 1) |
|---|---|---|---|---|
| Direction | [0 1 $\bar{1}$][$\bar{1}$ 0 1][1 $\bar{1}$ 0] | [0 $\bar{1}$ $\bar{1}$][1 0 1][$\bar{1}$ 1 0] | [0 1 $\bar{1}$][1 0 1][$\bar{1}$ $\bar{1}$ 0] | [0 $\bar{1}$ $\bar{1}$][$\bar{1}$ 0 1][1 1 0] |
| System | a1 a2 a3 | b1 b2 b3 | c1 c2 c3 | d1 d2 d3 |

*Table B1. The slip plane and slip direction defines a slip system. The different slip systems are labelled in the table and the same labelling are used in Fig.B3.*

# APPENDIX C: PUBLISHED PAPERS

**Paper A:** Nielsen, S.F., Wolf, A., Poulsen, H.F., Ohler, M., Lienert U. and Owen, R.A. (2000). A conical slit for three-dimensional XRD mapping. J. Synchrotron Rad. **7** p. 103-109.

**Paper B:** Poulsen, H.F., Nielsen, S.F., Lauridsen, E.M., Lienert, U., Suter, R.M. and Juul Jensen, D. (2000). Three dimensional maps of polycrystalline materials. Submitted to Nature.

**Paper C:** Juul Jensen, D., Kvick, Å., Lauridsen, E.M., Margulies, L., Nielsen, S.F., Poulsen, H.F. (2000). Plastic deformation and recrystallization studied by the 3D X-ray microscope. Mat. Res. Soc. Symp. Proc. **590** p. 227-240.

**Paper D:** Nielsen, S.F., Lauridsen, E. M., Juul Jensen, D. and Poulsen, H.F. (2000). A three-dimensional X-ray diffraction microscope for deformation studies of polycrystals. Proceedings of ICSMA12, Asilomar, California. In press.

**Paper E:** Nielsen, S.F., Ludwig, W., Bellet, D., Lauridsen, E.M., Poulsen, H.F. and Juul Jensen, D. (2000). Three dimensional mapping of grain boundaries. In: Proceedings of the 21$^{th}$ International symposium on materials science: Recrystallization – fundamental aspects and relations to deformation microstructure. Risø National Laboratory. Edited by N. Hansen *et al.* (Risø, Roskilde, Denmark, 2000), p. 473-478.

# Paper A

# Paper B

# Three dimensional maps of polycrystalline materials

**H. F. Poulsen[*], S. F. Nielsen[*], E. M. Lauridsen[*], U. Lienert[†], L. Margulies[*†], R.M. Suter[‡], T. Lorentzen[*] & D. Juul Jensen[*]**

[*] Materials Research Department, Risø National Laboratory, 4000 Roskilde, Denmark
[†] European Synchrotron Radiation Facility, BP 220, 38043 Grenoble, France
‡ Department of Physics, Carnegie Mellon University, Pittsburgh, PA 15213 USA

Polycrystalline materials, including most metals, ceramics and minerals, are composed of crystalline grains. Their properties are to a large extent governed by the size and arrangement of the grains and the character of the boundaries between them. At present information on the structure of the grains is only available from near-surface probes such as optical and electron microscopy[1-2]. This is unfortunate since surface and bulk characteristics in general differ substantially due to, for example, stress relaxation, migration of dislocations and atypical grain growth. Here we present a fast and non-destructive scheme for mapping the embedded grains within thick samples in three dimensions. All essential features: the position, volume, orientation, and stress-state of the grains as well as the morphology of the grain boundaries can be determined. Based on diffraction of hard X-rays from a synchrotron source[3-4], the structural changes of the individual grains can be studied during processing. As such the technique will facilitate the establishment of dynamical models based on first-principles in materials science.

Polycrystalline materials play a role in virtually every modern industry. The sizes and orientations of grains determine phenomena as diverse as the weight of beer cans and the prospect of high Tc superconducting cables[5]. The character of grain boundaries is the focus of an emerging technology termed "grain boundary engineering"[6]. In view of these observations it is remarkable that most structural techniques, including novel synchrotron μ-probes with 10-30 keV beams[7], only probe the surface and as such are unable to provide information on the dynamics of the grains and the grain-boundary network during thermal or mechanical processing. The one exception is neutron diffraction, which does probe bulk properties. However, this technique cannot resolve the individual grains that typically are in the 1-1000 micron size range. Due to this lack of *in-situ* microscopic probes, models of processing and grain evolution are generally formulated in terms of statistical properties.

To observe the grain dynamics, a probe is required which combines high penetration power, high spatial resolution and high speed of measurement. Furthermore the probe has to span a six-dimensional space. Three spatial dimensions specify the location and extent of the grains. An additional three dimensions specify the orientation of the crystal lattice of the grains. Conventional diffraction set-ups for depth resolved studies using slits formed as pinholes, grids[8] or cones[9] before and/or after the sample lead at most to multiplexing over two of these degrees of freedom. Such methods are prohibitively slow.

We describe a technique based on tracing of diffracted high energy X-rays that fulfils the above requirements. High energy X-rays (≥ 50 keV) can penetrate

millimetre thick specimens of all materials and as much as four centimetres of aluminium. Using focused synchrotron radiation,[4,10] sufficient flux is obtained to observe diffraction from individual grains with radii as small as 1 μm. Using a line focused beam and a high resolution area detector, an experimental technique and analysis algorithm is demonstrated which involves multiplexing over four dimensions, leaving one rotation and one translation to be carried out serially. Complete three-dimensional maps over cubic-millimetres of material can then be obtained within ~1 h.

Our technique is implemented at the 3-Dimensional X-Ray Diffraction (3DXRD) microscope[10] recently built at beamline ID11 at the ESRF synchrotron. Point or line focusing broadband monochromators have been developed including bent Laue-crystals and multilayer mirrors. Focal spot sizes are achieved down to $5 \times 5$ μm$^2$ and 1 μm x 1 mm, respectively.

The measuring procedure uses a tracing algorithm, inspired by the use of three-dimensional detectors in high energy physics. The principle is sketched in Fig 1. The line-focused beam illuminates a layer in the sample. The basic idea is to identify diffraction spots from individual grains within this layer and image the circumference of the grains by a combination of the geometry of the diffracted beam and rotations of the sample around an axis, ω, perpendicular to the illuminated plane. As the sample is rotated around ω, additional diffraction spots occur from the same grain. Combining the information, one can calculate the grain orientations. By translating the sample in *z* and repeating the procedure for several layers a three-dimensional map is obtained.

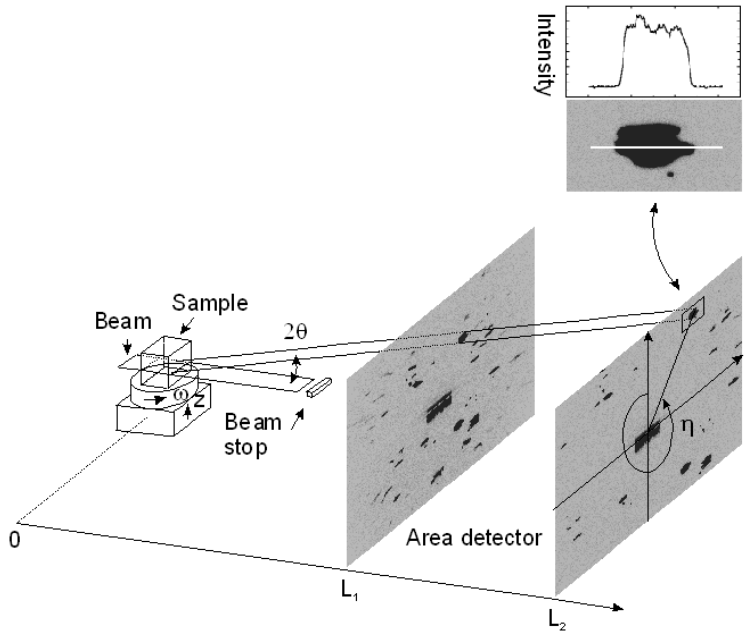


*Fig 1. Sketch of the X-ray tracing principle. The diffraction spots appearing in exposures of the area detector at different sample-detector distances are projected back to the illuminated plane in the sample. A typical intensity profile along a line in one of the diffraction spot are included, and angles $2\theta$, $\omega$ and $\eta$ defined.*

The ray tracing algorithm works as follows: the detector is set at a nominal distance, $L_1$, from the ω–axis and an exposure is acquired. During the exposure, the sample is oscillated over a range Δω (depending on the mosaic spread of the grains) to obtain a complete integration of the Bragg intensity. The intensity weighted centre-of-mass (CM) of each diffraction spot is computed. This procedure is repeated at detector distances $L_2$ and $L_3$. Linear fits through corresponding CM points extrapolate to the CM of the diffracting grains and yield the angles 2θ and η To obtain the cross-sectional grain shape, the periphery of the diffraction spot in the image acquired at the closest distance ($L_1$) is projected into the illuminated sample plane along the direction determined by the fit. This procedure is repeated for a number of ω settings, producing a complete map of all grain boundaries and grain orientations in the plane.

To illustrate the range of applicability of our technique, we show three examples of distinct applications. First, the basic six-dimensional mapping of a polycrystal is demonstrated, using a coarse-grained 99.996% pure aluminium sample. Initially the grains at a sample surface were mapped by electron microscopy (EBSP), and found to have an average mosaic spread of 1 degree. Next, the sample was aligned with the same surface parallel to the beam at the 3DXRD microscope and the tracing procedure was performed with a 5 μm wide beam incident just below the surface. The X-ray energy was E = 50 keV and the bandwidth ΔE/E = 0.5%. With a 1 second exposure time, 22 ω-settings with Δω = 2 degrees and detector distances *L = 7.5, 10.3* and *13* mm, the total data acquisition time was less than 4 minutes.

An example of the intensity distribution across a diffraction spot is included in Fig 1. It is nearly flat at the centre, with some tails reflecting the instrumental resolution and the mosaic spread of the grain. As a first approximation, the peripheries of the spots are set by a fixed intensity threshold.

The grain orientations determined by EBSP and X-rays reproduced within 1 degree. The grain boundaries are superposed in Fig 2. The 3DXRD boundaries are raw data with no interpolation or averaging between reflections from the same or neighbouring grains. The dominant error in the 3DXRD data is the point-spread function of the detector, which had a width of 16 μm. This is consistent with an average deviation of ≈ 20 μm between the boundaries determined by the two techniques.

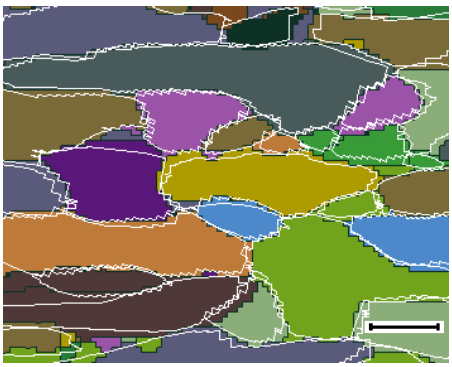

*Fig 2. Validation of the X-ray tracing algorithm. Colours and black outlines mark the grains and grain boundaries on the surface of an aluminium polycrystal as determined by electron microscopy (EBSP). Superposed as white lines are the grain boundaries resulting from the synchrotron experiment. The scale bar at the bottom is 400 μm.*

The quality of the 3DXRD map in Fig 2 is already sufficient for many basic studies, where the use of pure materials leads to large grains. Examples include *in-situ* studies of the grain rotations induced by deformation and grain boundary mobility studies by means of difference maps. Moreover, simplified descriptions of the grain morphology in terms of centroids (centre-of-mass position, volume and aspect ratio) can be very useful, especially for classifying grains.

We next present data on the nucleation and growth of new grains during annealing of a deformed 1 mm thick Aluminium specimen. Here, the line-focus was broadened to allow a uniform illumination of grains within a 150 μm wide layer. Grain volume kinetics for ≈ 100 emerging grains were inferred simultaneously from the integrated intensity of individual reflections[11]. X-ray tracing was used to determine orientations, describe clustering, and to identify valid grains: those fully illuminated by the beam and positioned truly in the bulk.

Results for four grains are shown in Fig 3 where grain volumes have been converted to radii assuming spherical grains. The material of choice had been examined intensively by conventional techniques and modelled by an Avrami approach common to metallurgy[12]. As a result, all grains were predicted to nucleate at the on-set of the annealing, and to grow with approximately the same growth velocity according to a universal curve. The synchrotron results clearly demonstrate the limitations of such an approach based on average properties, and should motivate the incorporation of fluctuations in future modelling. Our result constitutes the first direct observation of nucleation in metals, a process normally considered elusive as well as fundamental to metallurgy.

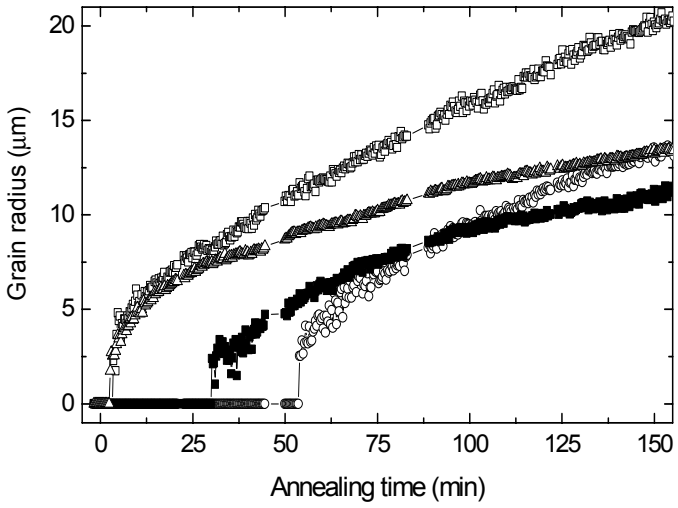


*Fig 3. Derived grain radii for 4 embedded nuclei, emerging during annealing of a deformed Al specimen at 270 $^{o}$C.*

In our third example the ray tracing algorithm is extended to include strain characterisation by adding an area detector at a large distance from the sample (the area detector in Fig 1 is semitransparent). From small shifts in angles 2θ and η the evolution of the average strain of each grain can be followed *in-situ* during deformation. As an example, results for tensile deformation of a 3 mm thick Cu specimen is shown in Fig 4. One 250 μm grain in the middle of the sample is singled out. In this case, the strain determination is based on 17 reflections. Generally the accuracy Δε on the strain measurements is given by the stability of

stability of the set-up and the resolution of the detector. For the present set-up $\Delta\varepsilon \approx 10^{-4}$, consistent with the scatter in Fig 4.

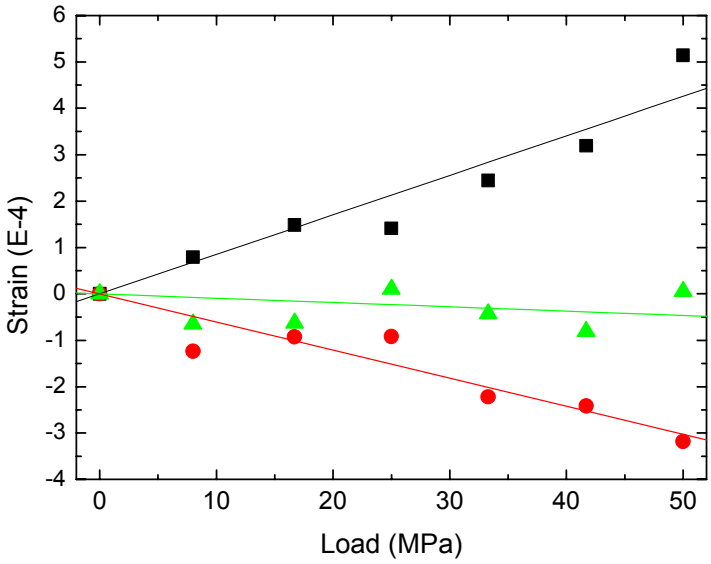


Fig 4. Evolution of selected strain components for an embedded Cu grain during tensile deformation. $\varepsilon_{22}$ (■) and $\varepsilon_{33}$ (•) represent directions along the tensile axis and transverse to it, respectively. $\varepsilon_{23}$ (▲) is the associated shear component. Lines represent linear fits to the data.

To increase the spatial resolution of maps such as the one presented in Fig. 2, software is presently being developed that makes use of the inherent crystallographic features. This includes automatic procedures for interpolation between reflections from the same and neighbouring grains. Ultimately, for non-deformed specimens the mapping accuracy is given by the width of the focal line, the detector resolution, and the accuracy of the sample movements. With present technology these factors can all be reduced to 1 μm. Indeed for synchrotron based X-ray tomography, which also involves the projection of hard X-rays on two-dimensional detectors, a spatial accuracy below 1 μm is now standard[13].

For deformed specimens, the mapping accuracy will be determined by the mosaic spread of the grains. The mosaicity leads to a one-dimensional spread of intensity along η in the images. The necessary integration over this distribution can be accomplished in two ways. First by combining data from constant 2θ line segments in several reflections in a reconstruction algorithm similar to the procedures for attenuation contrast tomography[14]. Or - at the expense of speed - by using a point-focus beam instead of the line-focus, and scanning the sample in y as well as z. The correction for mosaicity is then simply a question of integrating the spots in the η direction. The ultimate resolution is in this case similar to the non-deformed case.

1. Adams B.L., Wright S.I., Kunze K., *Metall. Trans. A*, **24A**, 819 (1993).

2. Forwood C.T., Clarebrough L.M. *Electron Microscopy of Interfaces in Metals and Alloys* (Inst. of Physics Publishing, Bristol 1991).

3. Bouchard R. *et al. J. Synchrotron Rad*. **5**, 90-101 (1998).

4. Poulsen H.F. *et al. J. Synchrotron Rad*. **4**, 147-154 (1997).

5. Dou S.X., Liu H.K. *Supercond. Sci. Technol.* **6**, 297-314 (1993).

6. Proc. 6th Conf. on Frontiers of Electron Microscopy in Materials Science, *Ultramicroscopy* **67** (1997).

7. O. Castelnau O. *et al*. *Materials Science Forum* **347-349,** 297-302 (2000).

8. Wroblewski T. *et al. Nucl. Inst. Meth. A* **428** 570-582 (1999).

9. Nielsen, S.F., Wolf A., Poulsen H.F., Ohler M., Lienert U., Owen R.A. *J. Synchrotron Rad*. **7**, 103-109 (2000).

10. U. Lienert, H.F. Poulsen, A. Kvick, *AIAA Journal*, in print.

11. Lauridsen, E.M., Juul Jensen D., Lienert U., Poulsen H.F. *Scripta Materialia,* in print.

12. Vandermeer R.A., Juul Jensen D. *Acta Metall. Mater*. **42**, 2427 (1994).

13. Baruchel J. *et. al. J. Synchrotron Rad.* **7**, 196-201 (2000).

14. Kak A.C., Slaney M. *Principles of Computerized Tomographic Imaging* (IEEE Press, New York, 1988).

ACKNOWLEDGEMENTS. This work was supported by the Danish Natural Science Research Council via Dansync and the Danish Technical Research Council, partly via the Engineering Science Centre at Risø. RMS also received support from the MRSEC program of the National Science Foundation. Correspondence should be addressed to H.F.P. (e-mail: henning.friis.poulsen@risoe.dk).

# Paper C

# Paper D

# A three-dimensional X-ray diffraction microscope for deformation studies of polycrystals.

*S. F. Nielsen, E. M. Lauridsen, D. Juul Jensen and H.F. Poulsen.*
Materials Research Department, Risø National Laboratory,DK-4000 Roskilde, Denmark.

Keywords: High-energy synchrotron radiation, X-ray diffraction, deformation, *in-situ* measurement, three-dimensional mapping.

## Abstract
*The microstructure in polycrystalline materials has mostly been studied in planar sections by microscopy techniques. Now the high penetration power of hard X-ray synchrotron radiation makes three-dimensional observations possible in bulk material by back tracing the diffracted beam. The 3DXRD microscope installed at the European Synchrotron Radiation Facility in Grenoble provides a fast and non-destructive technique for mapping the embedded grains within thick samples in three dimensions. All essential features like the position, volume, orientation, stress-state of the grains can be determined, including the morphology of the grain boundaries. The accuracy of this novel tracking technique is compared with electron microscopy (EBSP), and its three-dimensional capacity is demonstrated.*

## Introduction
Recently significant progress has been achieved in quantitative characterisation of plastic deformation [1,2]. It has been shown that the original grains subdivide into small volume elements of different crystallographic orientation by the development of medium to high angle dislocation boundaries. The subdivision and the morphology of the dislocation microstructure have been shown to be very important for the work hardening behaviour of the individual grains and the sample as a whole [3].
Previous investigations on tensile deformation of copper and aluminium show that the dislocation morphology can be classified into three types and the actual type of morphology does not seem to depend on the imposed strain [4]. However, it has so far not been possible to investigate the importance of the rotation history of individual grains for the final microstructure and grain orientation after straining. It is not known whether the dislocation structure within a grain with a given crystallographic orientation depends on the previous lattice rotation and/or the crystallographic orientations of the neighbouring grains. These questions can only be answered by applying a non-destructive technique with high penetration power, high spatial resolution and high speed of measurement to a three dimensional assembly of grains. This is now possible with the so-called Three-Dimensional X-ray Diffraction (3DXRD) microscope at the ESRF synchrotron, by application of a special beam tracking technique, which can be used to follow the crystallographic rotation and subdivision of grains during straining.

## The tracking technique

The tracking technique is based on a monochromatic high energy X-ray (50-80 keV) beam focused into a line and a 2 dimensional detector. The principle is sketched in figure 1. When the incoming beam is focused into a line it defines a layer within the sample. All grains that happen to fulfil Bragg's conditions in this layer give rise to diffraction spots on the detector. The diffraction spots are the projected image of the corresponding diffracting grains in the observed layer. The position of each diffraction spot is measured. While the exposure is made, the sample is oscillated over a range $\Delta\omega$ to obtain a complete integration of the Bragg intensity. The necessary $\Delta\omega$ value depends on the mosaic spread of the grains. The intensity-weighted centre-of-mass (CM) of each diffraction spot is computed. This procedure is repeated at several detector distances corresponding to different L values in figure 1. Linear fits through corresponding CM points extrapolate to the CM of the diffracting grains and provides the angles $2\theta$ and $\eta$ (see figure 1). To obtain the cross-sectional grain shape, the periphery of the diffraction spot in the image acquired at the closest distance is projected into the illuminated sample plane along the direction determined by the fit. The periphery of the diffraction spots is determined by setting a fixed intensity threshold.

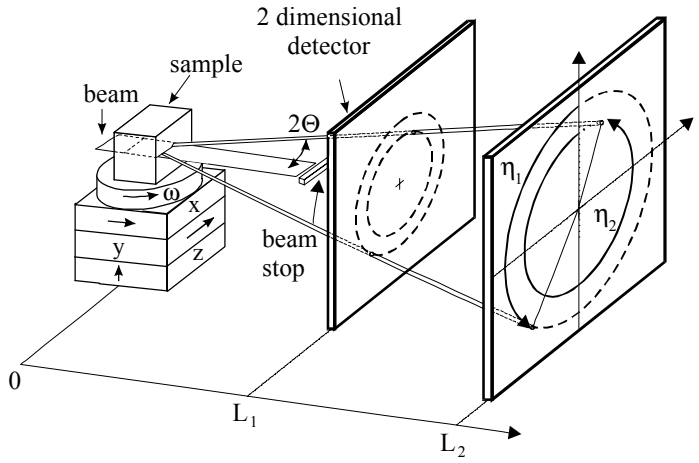


*Figure 1: Illustration of the tracking technique. When the detector is translated away from the sample the diffraction spots will move outwards on the detector. The positions of the diffracting grains in the sample are determined by linear fits. The fits also provide the $2\theta$ and $\eta$ values.*

By rotating the sample around an axis $\omega$, perpendicular to the illuminated plane, all grains will come to fulfil the Bragg condition and a complete map of all grain boundaries and grain orientations in the plane is thus produced. A three-dimensional map is then obtained simply by translating the sample in z and repeating the procedure for several layers.

## Result and discussion

As a validation test for the tracking technique a coarse-grained 99.996% pure aluminium sample was investigated. The sample was first annealed for 12 hours

at 500°C and slowly cooled to minimise the mosaic spread of the grains. One sample surface was polished and the grains at this surface were mapped by electron microscopy (EBSP). The range of orientation variation within the grains was found to be less then 1 degree. Afterwards the sample was aligned in the 3DXRD microscope and analysed with the tracking technique. The incoming beam was focused to 5 μm in height and limited in width to 0.8 mm by slits. Images were acquired at three different detector positions (L = 7.5, 10.3 and 13 mm), and 22 ω-settings with $\Delta\omega = 2$ degrees. With these settings the total data acquisition time was only 1 minute for one layer in the sample. The resulting grain boundaries for two grains found by the two different techniques are superimposed in figure 2. The black lines in the figure indicate the grain boundaries as determined by electron microscopy (EBSP), and the white lines indicate the grain boundaries resulting from the synchrotron experiment. The variation in the position of the grain boundaries determined by the two techniques is at the worst 50 μm. Maps of the grain boundary structure determined by the tracking technique will thus be of sufficient quality for many applications.

*Figure 2: Superimposed image of the grain boundaries of two grains as found by EBSP (black lines) and by the synchrotron tracking technique (white lines). The length of the scale bar is 200 μm.*

The grey shades in figure 2 indicate different grain orientations (EBSP) and the grain orientations determined by the two techniques have been found to reproduce within the combined alignment errors of the set-ups.
The 3DXRD boundary in figure 2 is the raw data with no interpolation or averaging. When the sample is rotated in ω several reflections will be observed from the same grain. A better fit of the grain boundary could be obtained by averaging between the different reflections from the same grain or taking the neighbouring grains into account.
Simply by translating the sample in z and repeating the procedure for several layers a complete three-dimensional map of one cubic millimetre of material can then be obtained within ~1h. The speed of this technique should be compared with conventional diffraction set-ups for depth resolved studies using slits formed as pinholes, grids [5] or cones [6] before and/or after the sample, which lead to very slow data acquisition. In the present experiment the tracking was performed on 20 different layers in the bulk of a cylindrical aluminium sample with a diameter of 5 mm. Well over 1000 images were recorded, each with at least 20 diffraction spots. This overwhelming data set has not yet been fully analysed but an automatic computer program is in the process of been developed in collaboration with Carnegie Mellon University in Pittsburgh, USA.

Figure 3 is an example of one grain followed in 3 dimensions through 6 different layers within the bulk of the aluminium sample.

## Outlook

By performing in-situ deformation of the sample while tracking the individual grains the evolution of the grain morphology and the grains orientations can be directly observed. The 3DXRD microscope was not equipped with a stress rig to do in-situ deformation, at the time of the present experiment. Alternatively we plan to deform the sample by compression outside the 3DXRD microscope and perform a sectioning at one of the layers mapped in the synchrotron experiment. By studying this layer, now the surface, in the electron microscope (EBSP) the crystallographic rotation of the grains in the layer can be determined and the grain morphology can be characterised.
Other applications for the tracking technique are for example in-situ recrystallization studies of the evolution of separate nuclei during annealing [7], and studies of grain-to-grain interactions.

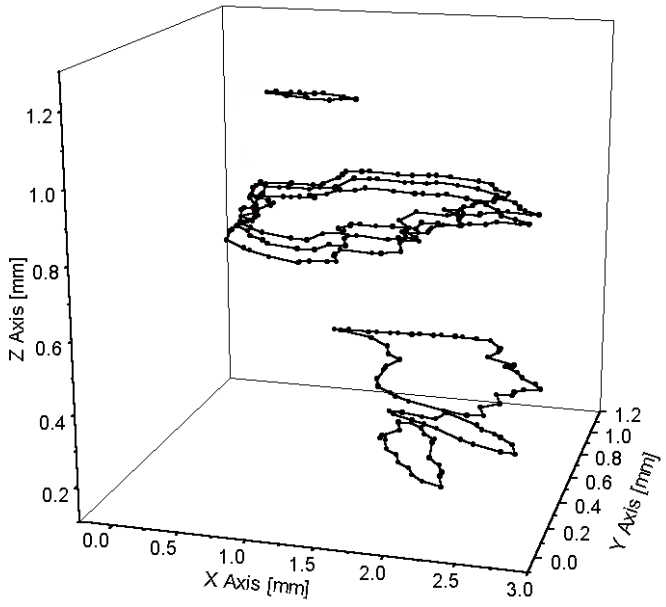


*Figure 3: A three-dimensional image of one embedded aluminium grain. The tracking was performed at 6 different layers in the grain. The sample is intended for later sectioning, and in order to minimise the difficulties of finding a particular layer, the tracking was done on three layers very closely spaced.*


## Acknowledgements

This work was supported by the Danish Natural Science Research Council via Dansync and the Danish Technical Research Council and by the Engineering Science Centre at Risø.

[1] D. Hughes these proceedings.

[2] N. Hansen, D.Juul Jensen, Phil. Trans. R. Soc. Lond. A 357 (1999) 1447.

[3] N. Hansen, X. Huang, Acta Mater. 46 (1998) 1827.

[4] X. Huang, N. Hansen, Scripta Materialia 37 (1997) 1.

[5] T. Wroblewski, O. Clauss, H.A. Crostack, A. Ertel, F. Fandrich, C. Genzel, K. Hradil, W. Ternes, E. Woldt, Nucl. Inst. Meth. A 428 (1999) p. 570.

[6] S.F. Nielsen, A. Wolf, H.F. Poulsen, M. Ohler, U. Lienert, R.A. Owen, J. Synchrotron Rad. in print.

[7] E.M. Lauridsen, D.Juul Jensen, U. Lienert, H.F. Poulsen, submitted for publication.

# Paper E

**Bibliographic Data Sheet** **Risø-R-1289(EN)**

Title and authors

Synchrotron radiation and deformation studies

Søren Fæster Nielsen

| ISBN | | | ISSN |
|---|---|---|---|
| 87-550-2931-0<br>87-550-2932-9 (Internet) | | | 0106-2840 |
| Department or group | | | Date |
| Materials Research Department | | | November 2000 |
| Pages | Tables | Illustrations | References |
| 145 | 6 | 57 | 75 |

Abstract (max. 2000 characters)

In the present thesis two different synchrotron X-ray diffraction techniques capable of producing non-destructive information from the bulk of samples, have been investigated. Traditionally depth resolution in diffraction experiments is obtained by inserting pinholes in both the incoming and diffracted beam. For materials science investigations of local strain and texture properties this leads to very slow data acquisition rates, especially when characterisation is performed on the level of the individual grains.

To circumvent this problem a conical slit was manufactured. The conical slit has six 25μm thick conically shaped openings matching six of the Debye-Scherrer cones from a fcc powder. By combining the conical slit with a microfocused incoming beam of hard X-rays an embedded gauge volume is defined. Using a 2D detector, fast and complete information can be obtained regarding the texture and strain properties of the material within this particular gauge volume. The capacity of the conical slit for depth profiling is demonstrated by scanning the gauge volume within the bulk of a polycrystalline copper sample, obtaining a two-dimensional map of the grain boundary morphology.

Another X-ray diffraction technique was applied on the three-dimensional X-ray diffraction (3DXRD) microscope at the ESRF synchrotron. The microscope uses a new technique based on ray tracing of diffracted high energy X-rays, providing a fast and non-destructive scheme for mapping the embedded grains within thick samples in three dimensions. All essential features like the position, volume, orientation, stress-state of individual grains can be determined, including the morphology of the grain boundaries. The first results obtained by using the novel tracking technique are presented in this thesis.

The tracking technique was applied in a preliminary experiment with the intention of following the rotation history of the crystal lattices in individual grains during deformation. The tracking technique was furthermore applied in combination with synchrotron X-ray tomography in order to gain new information on the wetting kinetics of liquid gallium in aluminium grain boundaries.

Finally, an electron microscopy investigation was carried out in order to describe the lattice rotations and texture evolution in uniaxially compressed aluminium single crystals and polycrystals.

Descriptors

Synchtron radiation, X-ray diffraction, conical slit, X-ray tracking, X-ray tomography, deformation, texture.

Available on request from Information Service Department, Risø National Laboratory,
(Afdelingen for Informationsservice, Forskningscenter Risø), P.O.Box 49, DK-4000 Roskilde, Denmark.
Telephone +45 4677 4004, Telefax +45 4677 4013